Spring 2015

Fusion welding of diboride-carbide ceramic composites

Derek Scott King

Department: Materials Science and Engineering

Recommended Citation

King, Derek Scott, "Fusion welding of diboride-carbide ceramic composites" (2015). *Doctoral Dissertations*. 2387.
https://scholarsmine.mst.edu/doctoral_dissertations/2387

FUSION WELDING OF DIBORIDE-CARBIDE CERAMIC COMPOSITES

by

DEREK SCOTT KING

A DISSERTATION

Presented to the Faculty of the Graduate School of the

MISSOURI UNIVERSITY OF SCIENCE AND TECHNOLOGY

In Partial Fulfillment of the Requirements for the Degree

DOCTORATE OF PHILOSOPHY

in

CERAMIC ENGINEERING

2015

Approved by

Gregory E. Hilmas, Advisor
William G. Fahrenholtz
Jeffrey D. Smith
Mohsen Asle Zaeem
Jay Switzer

PUBLICATION DISSERTATION OPTION

Sections in this dissertation were prepared for publication in peer reviewed journals. Pages 1-38 contain an Introduction and a Literature Review for background purposes. Pages 39-71 were published in the Journal of the European Ceramic Society in December of 2014. Pages 72-105 were submitted as a paper to the International Journal of Applied Ceramic Technology in January of 2015, and have been accepted for publication. Pages 106-136 will be submitted to Journal of the European Ceramic Society after revisions from committee members. Pages 137-151 were published in the Journal of the American Ceramic Society in January of 2014. Conclusions and Future Work sections are also included in pages 152-159. An Appendix is included for the purpose of presenting work that was performed, but not presented in a journal paper.

ABSTRACT

Plasma and pulsed plasma arc welding (PAW and PPAW) processes were used to fusion weld ZrB_2 containing 20 vol% ZrC. Varying welding parameters resulted in changes in weld pool shape and size, and the size of ZrB_2 grains within the fusion zone. For PAW processes that resulted in a keyhole fusion zone (full penetration), the arc to workpiece power transfer efficiency was estimated to be <20%. Power transfer efficiency was estimated to drop to <15% for non-keyhole welds. The power transfer efficiency was not estimated for PPAW processes, but keyhole formation was observed for PPAW FZs. ZrB_2 grain lengths were observed to decrease between binary PAW FZs (~1 mm in length), and binary PPAW FZs (~0.8 mm in length), and an increasing aspect ratio for ZrB_2 grains in PPAW welds (up to 40:1) compared to PAW ZrB_2 grain aspect ratios (up to 25:1) revealed that growth of ZrB_2 was hindered in PPAW FZs. Grain growth was also observed to decrease with decreasing arc power. A high arc power resulted in high growth rates of ZrB_2 and a textured FZ, lower arc power FZs did not exhibit texture. A high current plasma arc (222 A) was used to increase the temperature of the weld pool, such that ZrB_2 growth would follow the arc thermal gradient. ZrB_2 growth occurred in the basal plane, giving grains a plate-like structure, where grain thickness increased by ledge growth. ZrB_2 grain sizes within the FZ were observed to affect the strength of weldments. PM flexure strengths were measured to be ~660 MPa and strengths were observed to drop to ~140 MPa for PAW weldments and ~170 MPa for PPAW weldments. Diffusion of C into the melt pool was observed to hinder ZrB_2 grain growth significantly (~150 μm maximum ZrB_2 grain size), and the average flexure strength of a ZrB_2-ZrC-C weldments was ~250 MPa.

ACKNOWLEDGEMENTS

I would first like to thank my advisors Drs. Gregory Hilmas and William Fahrenholtz for guiding and supporting me throughout my time as a graduate student. Both have allowed me freedom in my research, and throughout my time they have allowed me to present my work through conferences and publications. I would also like to thank Dr. Watts for his guidance and support throughout my time as a graduate student. Whether they know it or not, each of these people have had a significant role in my life. More profound words escape me, but I would like to say that I am truly and sincerely grateful.

I would also like to thank my committee members, Drs. Jeffrey Smith, Mohsen Asle Zaeem, and Jay Switzer for their time, comments, and assistance throughout my research. You have helped put me on the path to success.

I would like to acknowledge that this research was funded by the Air Force Office of Scientific Research, grant number FA9550-12-C-0060. I would also like to acknowledge MO-SCI Corporation and CW Kim for their part in this program.

I have made many friends throughout my time at Missouri S&T, and I would like to thank you all for your support, even if you had no idea what I was talking about. I would name names, but I fear I would forget someone, and I'm off the hook for that… But seriously, having all of you in my life has been a pleasure. Thank you to the undergraduates who have worked for me, Andrew Schlup and Cari Swanson, you've been a tremendous help.

Lastly, I would not be here without the love and support of my family. To my mother and grandmother, I cannot begin to understand the sacrifices the two of you have made as I have grown and I truly appreciate everything. To my wife, Liz, you have supported me every step of the way and I am forever grateful. Our life together and our family has just begun, with the birth of our son, Alexander. Finally, to my son, I will watch you grow, I will teach you and you will teach me, and from the first moment that I saw you, I couldn't imagine my life without you. Know that I no longer make decisions for myself, but I strive to be the best for you, your mother, and hopefully someday your siblings, the best for our family.

TABLE OF CONTENTS

PAPER

SECTION

LIST OF ILLUSTRATIONS

Figure Page

PAPER I

PAPER II

PAPER III

PAPER IV

LIST OF TABLES

PAPER I

PAPER II

PAPER III

1. INTRODUCTION

Zirconium diboride (ZrB_2) is ceramic material belonging to the group of materials known as ultra-high temperature ceramics (UHTCs), where UHTCs are typically classified as ceramics with melting temperatures >3000°C.[1] Some of the properties that make ZrB_2 of interest include its high melting temperature (3245°C), high thermal conductivity (108 W/m·K), and chemical stability.[1-3] These properties make ZrB_2 attractive for applications such as molten metal crucibles, refractory linings, and hypersonic flight applications, such as atmospheric re-entry vehicles or rocket propulsion.[1,4-6] Due to the interest in using ZrB_2 for these applications, the ability to join ZrB_2 has also become of interest, where joining would be useful for repairs and complex shape fabrication.[7,8]

Brazing and solid-state techniques have received the most attention as potential joining techniques for UHTCs, but each have their issues.[7-9] For instance, palladium alloys have been studied for the joining of ZrB_2, but the melting temperature of these braze alloys are lower than the expected use temperature for several UHTC applications (>2000°C).[8,9] Solid-state joining, however, requires high temperatures and pressures to achieve dense joint microstructures. This can limit complex shape fabrication due to the processes typically utilized to densify UHTCs such as ZrB_2. Examining metal joining techniques reveals that fusion welding, joining by melting, is highly utilized for the joining of metals, but has received little attention for ceramic joining. Arc welding, fusion welding with an electric arc, is one of the most popular of these metals fusion welding techniques. With a low electrical resistivity (6 μΩ·cm), ZrB_2, may be an arc weldable ceramic, and fusion welding may be possible.[3,10,11]

The research reported in this dissertation focuses on the use of plasma arc welding for joining of ultra-high temperature ceramics, and its purpose is to better understand arc welding as a joining technique for ceramics. Specifically, it is of interest to understand the microstructural changes that occur due to the welding process and how those changes affect the microstructure and mechanical properties of the welded material. To understand the response of the parent material to arc welding, this research answers several questions:

1. Can plasma arc welding be used for the fusion welding of ZrB_2 based ceramics?
2. What are the differences between plasma arc welded microstructures and the microstructure of the non-welded material?
3. How do ZrB_2 grains grow within the melt pool, and can grain growth be controlled?
4. How do the strengths of welded ceramics compare to the parent material?
5. Is arc welding a joining technique limited to ZrB_2 based ceramics?

Arc welding has previously been reported as a method of joining ZrB_2 based ceramics, but this research presents processing-microstructure-property relationships that have not been previously investigated.[10,11] A more fundamental study of the mechanical behavior of the joint aids in determining the usability of the joined material, while understanding the related microstructures can lead to process improvements. Knowledge of the arc welding process for joining ceramics can lead to the production of complex shape parts that may not have been previously possible.

2. LITERATURE REVIEW

2.1 JOINING OF CERAMICS

Joining of materials has been of interest to mankind for a long time, such that lashed spears and arrows may even be considered early Stone Age applications of materials joining. But, the ability to extract and join metals would not be discovered until mankind entered the Bronze Age. Then blacksmithing or forging, a solid-state joining technique, was developed for joining metals, igniting a materials revolution due to the many uses of metals. It wasn't until the late 1800's, when French engineer Auguste de Méritens was awarded a patent for arc welding lead (Pb) using a carbon (C) electrode, that more advanced metal joining techniques were developed.[12] Since then the arc welding of metals has become widely studied and is a commonly practiced metal joining technique. Along with several arc welding techniques, many other joining techniques for metals remain popular, and include: forging, resistance welding, friction welding, friction stir welding, and even mechanical fastening.[13-15] As metals joining continues to advance, with the evolution of new techniques and increased understanding, ceramic joining remains relatively limited to brazing and solid-state joining techniques.[7-10,16-18]

2.1.1 Braze Joining. Brazing is a highly versatile joining technique that can join a variety of materials. Brazed joints are made using a low melting temperature alloy, or with a glass/glass ceramic.[9,18-24] For example, SiC fiber reinforced ceramics are of interest for use in applications such as nuclear reactors and turbine engines. Processing typically allows for the production of the necessary shapes, but attaching the ceramic part to another ceramic or metal component becomes a challenge. The many patents covering ceramic joining techniques for the production of ceramic turbines highlight this issue.[25-29]

Therefore, to advance use in applications, research on brazes typically focuses on wetting behavior, interfacial reactions, and bond strength.[9,22,23] Yano et al. investigated the brazing of SiC/SiC ceramics using a Ag-Cu-Ti alloy.[23] High resolution electron microscopy (HREM) was used to observe the presence of TiC at the interface between the braze and SiC. Increasing braze time and temperature led to an increase in bending strength where brazed components manufactured at 850°C had strengths of ~100 MPa and components manufactured at 950°C had strengths of ~300 MPa. The increase in strength was contributed to epitaxially grown TiC that exhibited good lattice matching between SiC, reducing residual stress. More recently, Singh et al. examined a Ag-Cu-Ti foil braze for the joining of SiC/SiC.[18] Diffusion of Si from SiC led to the formation of a 1 μm TiC interfacial layer at the surface of the SiC, and a 1-2 μm Ti-Si phase that separated the TiC interfacial layer and the braze. Elevated temperature shear strength testing revealed that cracking initiated along the Ti-Si/TiC interface.[18] Numerical modeling of the stresses within the joint was carried out, revealing the highest stresses to be in the interfacial region of the joint (**Figure 2.1**). The increased stresses at the Ti-Si/TiC interface revealed why failure occurred at that interface.

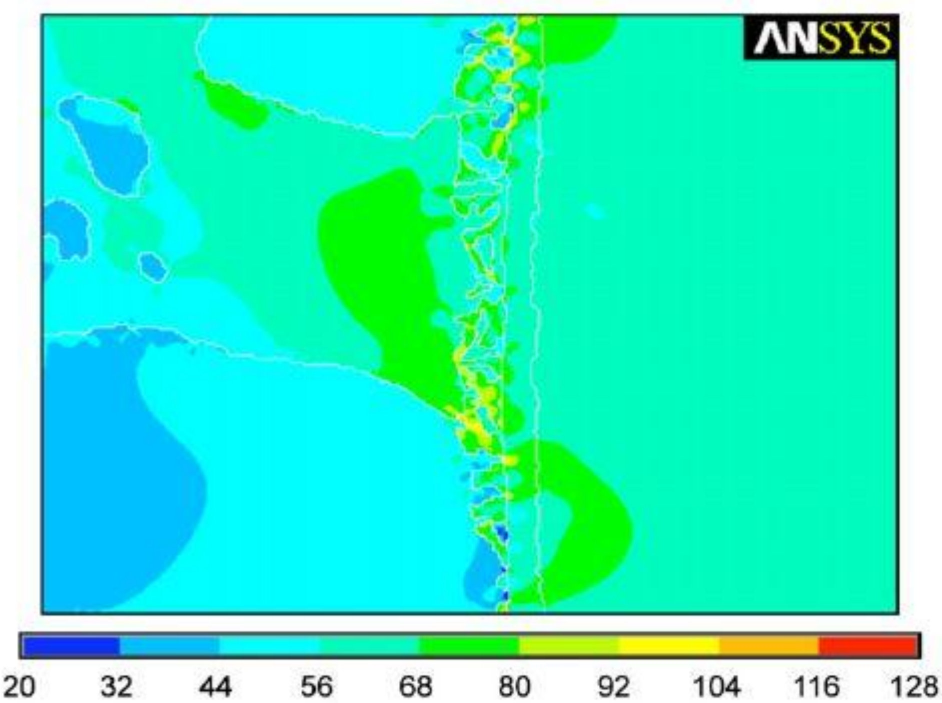

Figure 2.1: Stress distribution in the interfacial layers of brazed SiC, modeled by Singh et al., where stresses are highest in the Ti-Si and TiC interfacial layers. Scale is in MPa.[18]

With good strength (~100 to ~400 MPa) and low processing temperatures (<1000°C) brazing is an attractive joining technique for manufacturing of complex shape parts, or metal to ceramic joints.[18,21-23,30] However, one drawback of brazes can be use temperature. When utilized in UHTC applications, many braze alloy melting temperatures are lower than the expected use temperature of UHTCs (>2000°C).[1,8] For example, palladium alloy brazes have been developed as a lead candidate for brazing ZrB_2-SiC to themselves or metals and are favored in comparison to Ag or Ni based brazes due to a higher melting temperature and oxidation resistance.[7,30,31] Commercially, Palco® (65Pd-35Co) and Palni® (60Pd-40Ni) brazes have been of interest. Both brazes have high thermal expansion coefficients (CTE), making residual stresses between the braze and the ceramic a concern. Palini, for example has a CTE of 15×10^{-6}/°C, much higher than that of ZrB_2 (a=6.7x10^{-6}/°C c=6.9x10^{-6}/°C) or SiC (a=3.7x10^{-6}/°C c=4.5$10^{-6}$/°C).[7,32,33] The large difference in CTE results in the development of tensile residual stresses in the braze and compressive residual stresses in ZrB_2-SiC after cooling from the brazing temperature. **Figure 2.2** demonstrates how CTE differential leads to the development of thermal residual stresses between layers that are bonded. The dashed lines represent an unconstrained system after cooling from processing, while the solid boxes represent layers that remain bonded during cooling. Elements in each layer represent the tensile and compressive stresses developed from CTE mismatch. When the stresses become large enough, cracking or delamination of the layers can occur.[34-37] In ZrB_2-SiC brazed joints, the high ductility of Palco (43% elongation) and Palni (23% elongation) can be expected to reduce the stresses developed in the joint. Still, good wetting behavior between Palco or Palni and ZrB_2-SiC, and chemical interaction, lead to residual stresses (>1.5 GPa) that can crack the ceramic, affecting the mechanical integrity of the joined part.[7,30,31]

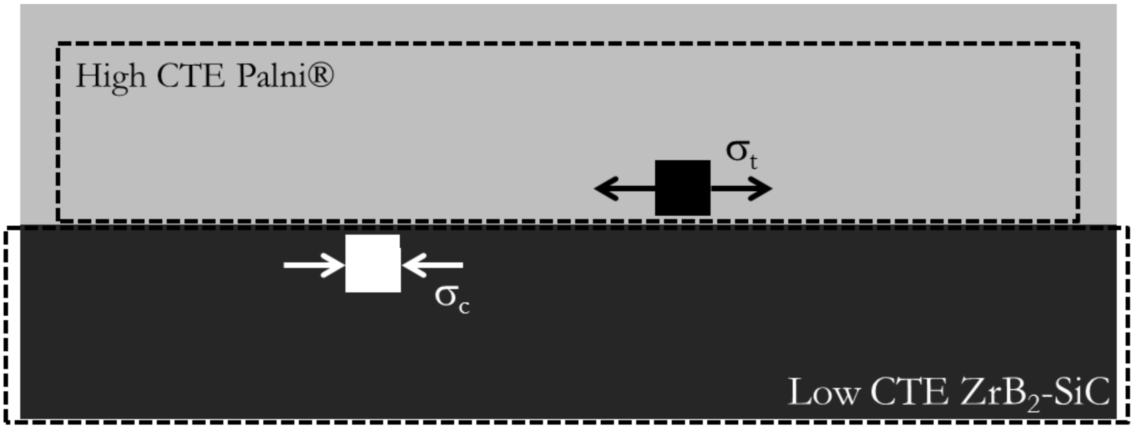

Figure 2.2: Development of thermal residual stresses between layers with a CTE differential.

In lieu of metal brazes, glass brazes have also been investigated for the joining of ZrB_2 based ceramics. Esposito and Bellosi investigated the joining of ZrB_2-SiC ceramics using glass interlayers.[38] Esposito and Bellosi measured a CTE of 7.5×10^{-6}/°C for their ZrB_2-SiC ceramic (20 wt% SiC) up to 1300°C. Comparatively, their glass brazes had CTEs ranging from 5.3 to 6.6×10^{-6}/°C, and compressive stresses within the glass braze were of concern.[38] The highest CTE glass, containing SiO_2 (34.0 wt%), Al_2O_3 (39.8 wt%), and CaO (26.2 wt%) resulted in the best bonding characteristics. The glass wet the surface of the ZrB_2-SiC and the low CTE mismatch resulted in a crack free bond. Oxidation of the SiC within the microstructure also led to good penetration of the braze, creating a stronger bond. Three-point bend strengths of the joints were measured to be ~280 MPa, compared to 730 MPa for the parent material (PM). Testing at 1000°C resulted in strengths of ~90 MPa, and it was concluded that the glass braze would not be suitable for use at temperatures ≥1000°C, thus use temperature remain an issue for glass brazes.[38]

2.1.2 Solid State Joining. Joints manufactured without the use of a braze, or the creation of a melt pool, are considered solid-state joints. Solid-state joining techniques such as friction stir welding and forging are utilized for metals joining. Typically, solid-state ceramic joints are manufactured by the densification of an interlayer.[24] As an example, Pinc et al. utilized spark plasma sintering (SPS) to join ZrB_2-SiC with a Zr-B reactive interlayer.[8] Joints were formed by layering a Zr-B-ZrB_2-SiC powder mixture between two dense ZrB_2-SiC billets (30 vol% SiC). The sandwich was then placed in a graphite die and heated to a temperature of 1800°C in a SPS furnace. Specimens were also compressed at 2.5 MPa pressure during joining. Densification and diffusion from the powder interlayer resulted in the production of a seamless joint, where the microstructure of the joint was analogous to that of the parent material (PM).[8] The shear strengths of joints were measured to be 311±38 MPa compared to 345±40 MPa for the parent material, and due to large overlap in the standard deviations, it was concluded the PM and joints were statistically equal in shear strength.[8] Further, oxidation testing revealed no difference in behavior between the PM and the joint. The work by Pinc et al. is the first report of utilizing SPS to join ZrB_2 based ceramics, but the authors do propose that hot-pressing may be utilized for joining in a similar fashion.

Continued work in the SPS joining of ceramics has shown the ability to utilize solid-state joining techniques to join different ceramics.[39-42] The joining of β-SiC was studied by Grasso et al., using SPS as the joining technique.[40] As with the ZrB_2-SiC joints, SiC-SiC joints (**Figure 2.3**) appear to have a microstructure similar to that of the PM, and the presence of the joint is recognized by a slight misalignment of the two PM coupons.[40] SiC-SiC joint strengths were measured in four-point bending, and compared to the flexure strength of the PM. Similar to the joints of ZrB_2-SiC of Pinc et al., SiC-SiC joint strengths in bending were 193±21 MPa and the PM was 176±10 MPa.[8,40] The elastic modulus of the joints and PM were 436±1 GPa (joint) and 448±4 GPa (PM). The comparison of mechanical properties and microstructure reveals that there was essentially no difference between the joint and the PM.

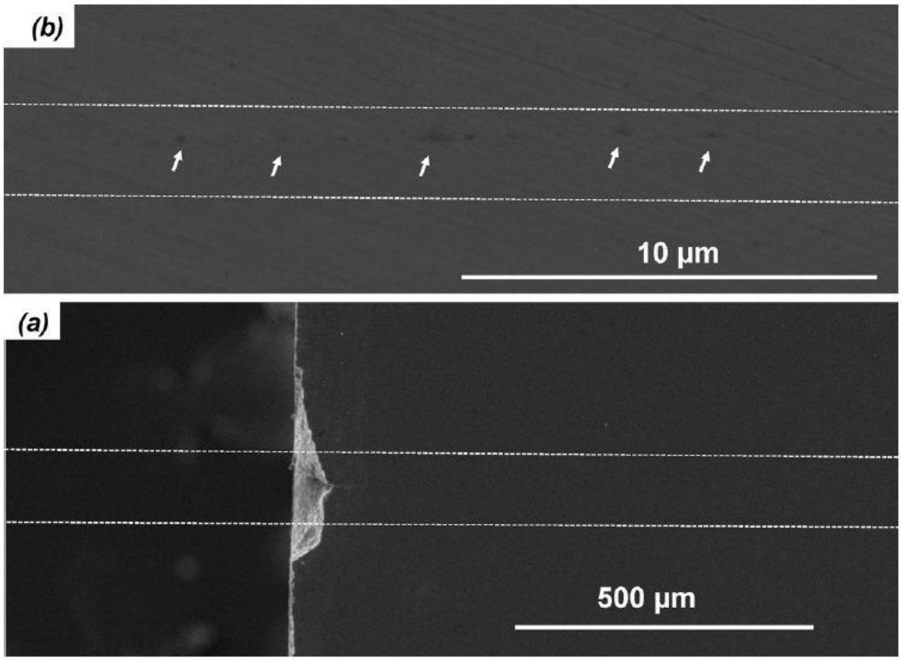

Figure 2.3: Scanning electron microscopy of SPS SiC-SiC joints, where the joint is identified by a misalignment of the SiC coupons (a). Microstructural analysis reveals the joint to have a similar microstructure to that of the parent material (b).[40]

Unfortunately, SPS and hot-pressing are limited to the fabrication of relatively simple shapes, and may require machining after densification. Therefore, pressureless sintering is necessary to take full advantage of solid-state joining in the production of complex shape ceramics.[1] However, the densification of advanced ceramics such as SiC and ZrB_2 is difficult, one of the reasons why SPS and hot-pressing are preferred methods of densification for such advanced ceramics.[6,43-46] This was observed by Grasso et al. when the SPS joining of SiC was compared to the pressureless joining of SiC.[40] Voids were observed at the interface of the joint, **Figure 2.4**. Diffusion between the two SiC coupons to be joined was observed, but the mechanical strength of the joined specimens was low enough that it could not be analyzed. While Grasso et al. focused on direct joining, rather than using an interlayer, pressureless joining using a powder interlayer may result in similar void formation through incomplete densification or contraction of the interlayer volume during densification.

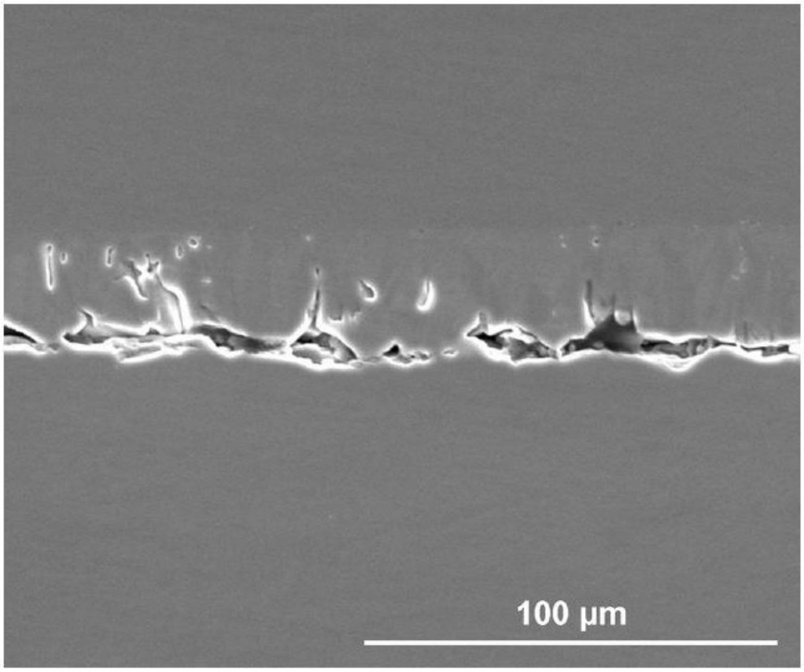

Figure 2.4: Pressurelessly sintered SiC-SiC joint. Voids formation was apparent along the interface of the joint.[40]

2.1.3 Fusion Joining. Fusion joining of ceramics has not received the same amount of interest when compared to brazing and solid-state joining techniques. But, limited research on the fusion joining of ceramics is available, where much of the fusion joining research focuses on electron beam and laser welding techniques.[10,11,47-51] Burdovitsin et al. demonstrated the ability to fusion weld non-conducting ceramics, and were able to fusion weld a fused alumina ceramic (Alundum®), quartz, and glass via electron-beam welding.[51,52] Preliminary tensile strength testing gave weld strengths of 15-30 MPa, compared to 40-50 MPa for the strength of the PM.[51] Continued work by

Burdovitsin et al. demonstrated the effect of beam exposure time on the weld pool, where increasing beam exposure time resulted in increased penetration. For two different alumina based ceramics (secondary phases included: SiO_2, Cr_2O_3, MnO, and CaO), Burdovitsin et al. achieved penetration depths up to ~3.8 mm and weld pool diameters up to ~13.8 mm.[52] Examples of welded specimens from Burdovitsin et al. (**Figure 2.5**) reveal how ceramic fusion welding can be useful in the production of ceramics with complex shapes.[52] However, the expensive nature of the equipment needed for electron beam welding (100s of thousands to millions of dollars for equipment) and the slow times reported by Burdovitsin et al. (10 min) to weld components (**Figure 2.5**) keep electron beam welding from being a cost-effective fusion joining technique.[52]

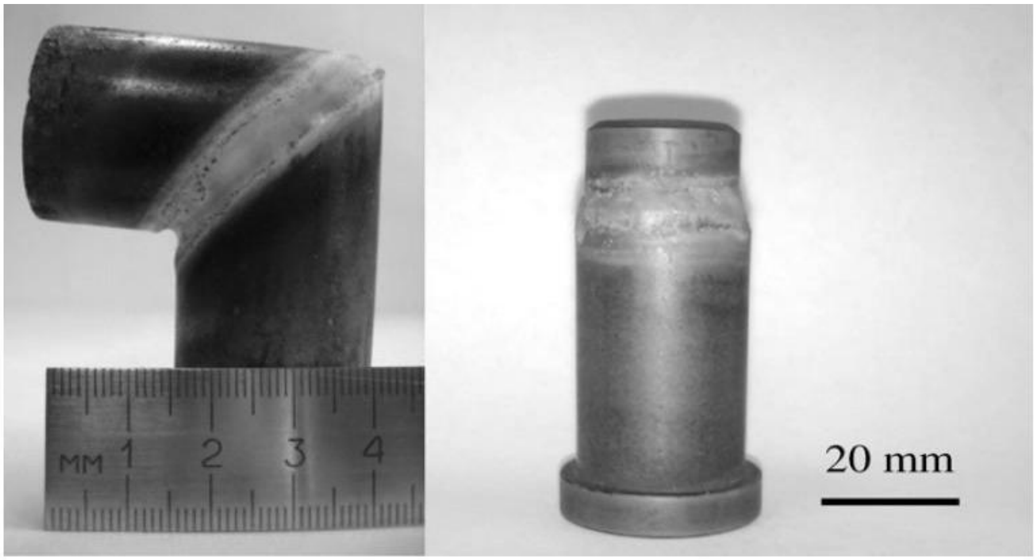

Figure 2.5: Fusion welding of alumina based ceramics, where Burdovitsin et al. utilized electron-beam processes in the production of complex shape ceramics.[52]

Laser welding techniques have also been investigated for the fusion welding of non-conducting ceramics, however, large penetration depths were not observed, like those of electron beam welds. Bradley et al. utilized laser welding with an oxy-acetylene flame assist to seal the surface of alumina based refractories.[50] Using a CO_2 laser and a power density of 5.4 MW/m^2, Bradley et al. observed penetration depths up to 1.5 mm into the refractory.[50] When compared to the power density utilized by Burdovitsin et al. (15-20 MW/m^2), the CO_2 laser presents a lack of power as a fusion welding technique, but higher powered lasers should also be useful in the fusion welding of non-conductive specimens.[52]

Both laser and electron beam welding offer the ability to fusion weld ceramics, but work by Rice also suggested that arc welding could be utilized to fusion weld ceramics.[10] Rice reported the use of arc welding to join ZrB_2 and TaC to themselves, as well as fabricating ZrB_2 ceramic composites of ZrB_2-C, ZrB_2-SiC, ZrB_2-Mo/Nb/Ta. Rice also reported the ability to arc weld W to graphite and ZrB_2 to graphite. The highest reported weld strengths by Rice were from arc welded ZrB_2-ZrB_2 specimens, with strengths ranging from 20-60 psi (~140-410 MPa).[10] Commercially available arc welding systems also have a much larger range of available power densities compared to the laser welding and electron beam welding techniques reported by Bradley et al. and Burdovitsin et al.[50,52] Power densities between 10 and 100 MW/m^2 are possible through the use of gas tungsten arc welding (GTAW), commonly referred to as tungsten inert gas (TIG) welding.[53] As Rice exhibited that arc welding of ZrB_2 based ceramics was possible, Hilmas et al. were also able to utilize the more power dense arc welding techniques to fusion weld ZrB_2-SiC-B_4C and ZrB_2-SiC ceramics.[11] Their work indicated that the welding electrode was tungsten and negatively poled, indicating that the welding process is directly comparable to GTAW welding. A cross-section of the ZrB_2-B_4C-SiC weldment microstructure was reproduced from the work of Hilmas et al. in **Figure 2.6**, where all three phases were observed.[11] It is important to note that ZrB_2 and B_4C have defined melting points (3250°C and 2450°C), and monolithic SiC is understood to dissociate (~2700°C).[1,2,54,55] Rather, eutectic reactions between SiC and ZrB_2 and SiC and B_4C have been observed.[56,57] While Rice reported the arc welding of a ZrB_2-SiC ceramic, the microstructural observations provided by Hilmas et al. provide post welding evidence that even under the high heat fluxes of an arc, a ceramic system containing non-melting phases can still melt in an equilibrium manner through invariant reactions.[10,11]

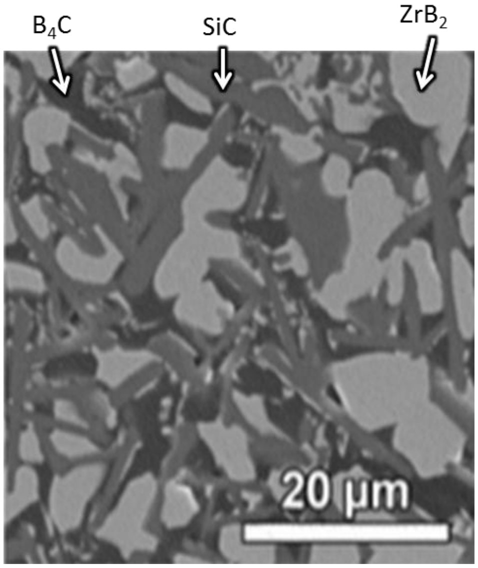

Figure 2.6: Fusion zone microstructure of a ZrB_2 (light grey), SiC (dark grey), and B_4C (black) weldment.[11]

Considering brazing, solid-state, and fusion joining, the joining techniques available to a ceramic engineer are almost as broad as metals joining techniques, but the amount of research on the fusion joining of ceramics does not compare to that of metals fusion welding. Even though laser welding, electron beam welding, and arc welding have been investigated as a possible fusion joining techniques for ceramics, but the understanding of fusion welded ceramics is still limited.

2.2 PLASMA ARC WELDING

While TIG welding processes were utilized by Hilmas et al. to weld ZrB_2 based ceramics, more powerful arc welding techniques could also be used for the fusion joining of UHTCs.[11] A process such as plasma arc welding (PAW), which has power densities ranging from 100-10,000 MW/m^2, would be useful for melting UHTCs while allowing more flexibility in welding parameters.[53]

PAW is a very similar welding technique to GTAW in that both techniques utilize a non-consumable W electrode that is negatively poled. In both PAW and GTAW, electrons transfer from the electrode to the positive workpiece. The stripping of electrons from the electrode cools the electrode, whereas electrons entering the workpiece add heat to the workpiece. The difference between PAW and GTAW is the use of a plasma gas for additional heat transfer and arc guidance in PAW. The pressure caused by the plasma jet also results in movement of molten material into the formation of a hole in the weld pool. This form of welding is known as keyhole welding, an attractive process, as it provides full penetration of the workpiece.[58,59]

Figure 2.7 is a schematic of a typical plasma arc welding torch. To strike an electric arc to the workpiece, a pilot arc is formed between an electrode and a copper sleeve. Then the pilot arc is used to ignite argon and form the plasma. Once the plasma has formed, an arc can be struck to the workpiece, where during keyhole welding, the faces of a joint melt as the arc and plasma jet are moved along the joint. When the proper welding parameters are chosen (welding current, plasma flow rate, welding speed) the weld pool fills in the hole behind the arc resulting in the completed full penetration weld. However, a narrow range of parameters exists that can be utilized for PAW, where low currents and plasma flow rates can cause the keyhole to disappear, while high currents and plasma flow rates blow the melt pool away, leading to cutting rather than joining.[59] Therefore, control of PAW parameters during keyhole welding is essential.

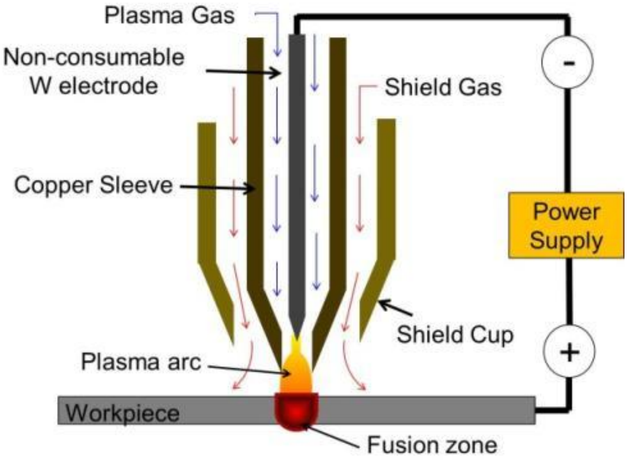

Figure 2.7: PAW torch schematic showing individual components and welding polarity.

As previously discussed, PAW has a higher power density that GTAW, due to the heating of the workpiece by both the arc and a plasma jet.[53] Metcalfe and Quigley analyzed a 10 kW (250 A current, 40 V voltage) PAW arc to determine the breakdown of heat transfer in the arc and compare it to a GTAW arc. Metcalfe and Quigley demonstrated that for heat transfer in a PAW arc, convection and radiation effects are higher, while anode effects are lower for PAW processes, compared to GTAW processes. The anode effects are defined as a combination of electron thermal energy, work function, and anode fall. In GTAW, anode effects contributed to 39% of the total power, or 89% of the transferred power. The anode effect contribution dropped to 16% of the total power, or 24% of the transferred power for a fully penetrated weld pool. For a weld pool that did not reach full penetration, the anode effects contributed 26% of the transferred power. Metcalfe and Quigley calculated that for a GTAW arc, less than 5% of the total arc power was transferred to the workpiece by convection and radiation. For PAW processes, weld penetration plays a role in the amount of heat transfer from the arc to the workpiece, as a keyhole weld will trap radiation due to the cone-like shape of the keyhole. The calculated heat transfer from radiation for a keyhole PAW arc was 19% of the total arc power (29% of transferred power), and a non-keyhole weld was 17% of the total power (29% of total power). Convective heat transfer is also affected by penetration, due to the effect of gas flow over the weld pool surface, where an impinging gas flow, as depicted in **Figure 2.8**a, will transfer less heat than flowing gas, **Figure 2.8**b. Metcalfe and Quigley then calculated the heat transfer by convection for a PAW arc to be 31% of the total power (47% of transferred power) for a keyhole weld and 27% (45% of transferred power) for a non-keyhole weld. The conclusion from Metcalfe and Quigley was that for PAW, 66% of the total arc power was transferred to the workpiece for a keyhole weld and 60% of the total arc power was transferred to the workpiece for a non-keyhole weld. The calculations from Metcalfe and Quigley also agree well with the work of Arata and Maruo who experimentally determined a PAW heat transfer efficiency ranging from 50-75%.[53,60]

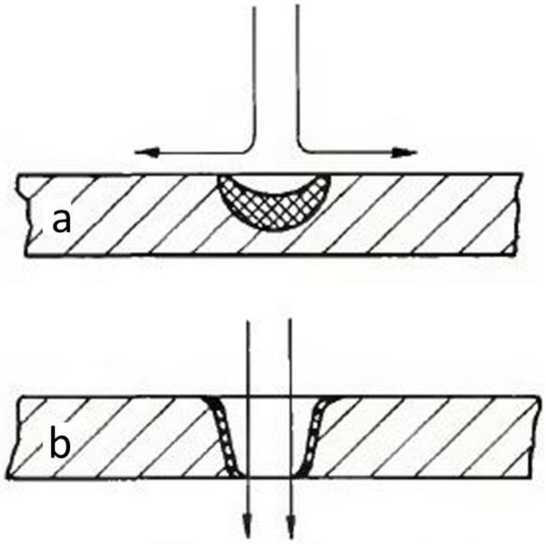

Figure 2.8: Gas flow of PAW process where penetration depth affects gas flow and heat transfer. An impinging flow (a) will result in less heat transfer than gas flow through the weld pool (b).

Evans et al. also calculated heat transfer for a PAW arc, but the work was based on a lower power arc, ~2.8 kW (110 A current, 26 V voltage), than that of Metcalfe and Quigley.[53,61] Evans et al. also utilized a lower plasma flow rate (0.94 l/min) compared to Metcalfe and Quigley (7 l/min). The change in welding parameters resulted in a reduction of the calculated heat transfer to the workpiece, 51% of the total arc power.[61] The work by Evans et al. reveals that discrepancies exist between different mathematical approaches, but their work and that of Metcalfe and Quigley agree well with the reported ranges for PAW arc heat transfer (50-75%).[60,62] Assuming that PAW of ZrB_2 based UHTCs results in 50% power transfer to the workpiece for heating, PAW will still be a more efficient technique than GTAW, where only 36-46% of the total arc power is transferred to the workpiece during welding.[63,64]

2.3 NUCLEATION AND GROWTH DURING SOLIDIFICATION

During the fusion welding of UHTCs, it is implicated by name (fusion), that the welding process involves melting. During the solidification of a the weld pool, the number and size of crystals may give insight into how hot the weld pool stayed during cooling, or how thermal gradients developed. While the exact temperature of a UHTC weld pool may not be known, understanding of nucleation and growth kinetics paired with microstructural information can give insight into cooling rates, thermal gradients, and relative temperature (i.e. where the hottest region of the weld pool was located, or what welding parameters give a hotter weld pool).

Solidification of a solid phase directly from a liquid (homogeneous nucleation) occurs first with the formation of embryos, the continued growth of which is controlled by competing processes of the energy required to create a new interface between two phases, and energy released as the volume free energy for phase transformation.[65-68] These competing processes can be written as Equation 2.1, where ΔG is free energy associated with the formation of a new spherical phase, r is the radius of the sphere, γ is the interfacial energy, and ΔG_s is the free energy change per unit volume for solidification.

$$\Delta G = 4\pi r^2\gamma + \frac{4}{3}\pi r^3\Delta G_s \qquad (2.1)$$

Equation 2.1 can also be plotted, Figure 2.9, demonstrating that there is a critical radius, r^*, at which the volume energy term becomes dominant, and the growth of a nucleated embryo will become a stable nucleus. The inflection point of the curve gives a maximum in ΔG, denoted ΔG^*, or the free energy of an embryo with the critical radius.

As ΔG^* is the inflection point of the curve, an equation can be written for the determination of ΔG^* (Equation 2.2).[65,66]

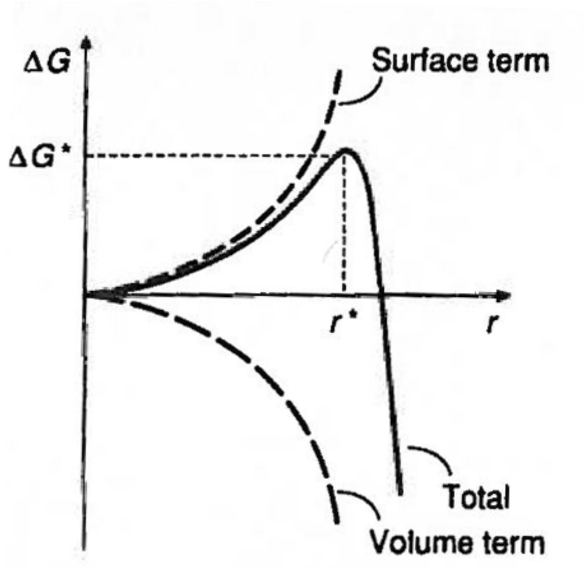

Figure 2.9: Free energy of a nucleus as a function of size. A critical size and energy must be exceeded before an embryo becomes a stable nucleus. From Evans and De Jonghe.[66]

$$\Delta G^* = \frac{16\pi\gamma^3}{3(\Delta G_s)^2} \tag{2.2}$$

From Equation 2.2, γ and ΔG_s would be expected to change with temperature, where ΔG_s is controlled by the enthalpy (ΔH_s) and entropy (ΔS_s) for a specific phase change (Equation 2.3)$\Delta G_s = \Delta H_s - T\Delta S_s$ (2.3). Taking into account that at an equilibrium transformation temperature (T_0), such as equilibrium transformation from liquid to solid, $\Delta G_s=0$, and Equation 2.3 can be rewritten as Equation 2.4. Equation 2.4 reveals that the ability to develop stable nuclei is dependent on a degree of undercooling, hence, the homogeneous nucleation rate is dependent on a degree of undercooling.[66]

$$\Delta G_s = \Delta H_s - T\Delta S_s \tag{2.3}$$

$$\Delta G_s = \Delta H_s \frac{T_0 - T}{T_0} \tag{2.4}$$

Heterogeneous nucleation may also occur from a melt, where compared to homogeneous nucleation, heterogeneous nucleation occurs on the surface of another phase. By nucleating from a surface that is already present within the liquid, the surface energy term of Equation 2.1 (first term) is reduced, and the overall barrier to form a stable nucleus is reduced.[65,66]

Once a stable nucleus is formed, it is expected to grow at a rate that is dependent on the temperature and the saturation of the surrounding liquid. Several models exist to describe crystal growth rates. Grain growth that occurs by the addition of atoms at step-like sites is known as ledge growth, and models exist to describe grain growth through surface nucleation.[65,68,69] Many other models have been developed that describe crystal growth, but a general expression for crystal growth can be described by Equation 2.5, where u is the growth rate, k is Boltzmann's constant, T is temperature, a_0 is the interatomic separation distance, and η is the liquid viscosity.[67]

$$u = \left(\frac{kT}{3\pi a_0^2 \eta}\right)\left[1 - \exp\left(\frac{\Delta G}{kT}\right)\right] \tag{2.5}$$

Like nucleation rate, Equation 2.5 changes with temperature (T), the difference is that growth can occur immediately after cooling from a melt, but only if nuclei are available.[67] This leads to the formation of the metastable growth region observed in Figure 2.10.[67] In a weld pool, nucleation and growth kinetics play an important role in the appearance of the solidified microstructure, as the cooling rate has an effect on the nucleation rate and the temperature of the weld pool will affect the grain growth, where grains in solidified weld pools are also expected to follow the largest thermal gradient.[68]

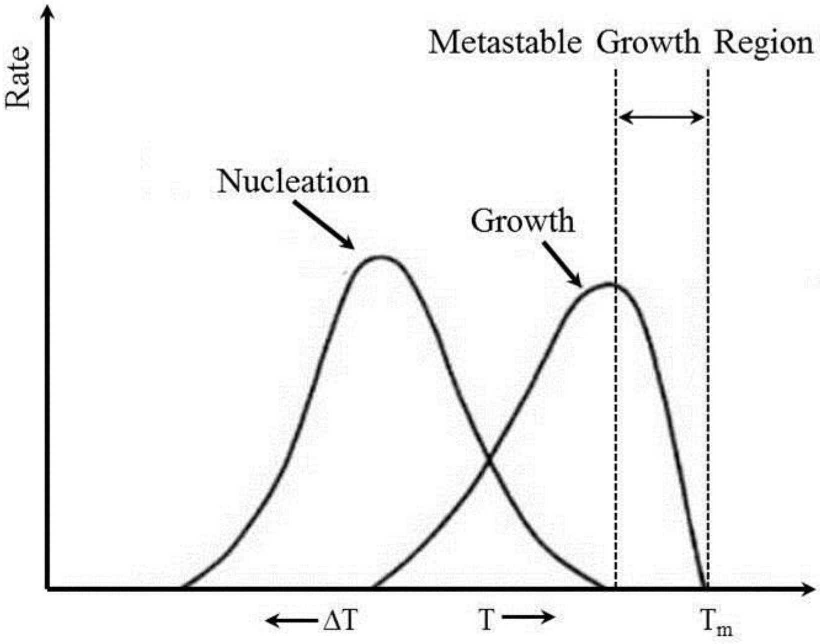

Figure 2.10: Comparison on nucleation and growth rates as a function of temperature and ΔT. Redrawn from Shelby.[67]

2.4 ANALYSIS OF MICROSTRUCTRAL ORIENTATION/TEXTURING

During welding, thermal gradients form that affect the solidification of a weld pool. As previously discussed, the rate at which the weld pool cools could affect the nucleation kinetics, while retained heat could affect growth rates. Thermal gradients created during arc welding could also affect the growth direction of crystals in a solidifying weld pool. This was observed by David et al., who studied the effects of grain orientation in solidified weld pools as a function of welding parameters and crystal orientation.[70]

David et al. used grain boundary orientation to determine the crystallographic direction of grains within the weld pool of electron beam welds on single-crystal Fe-15Cr-15Ni.[70] Their work increased the understanding of the solidification of the weld pool based on weld speed and the PM crystallographic direction. While PM crystallographic direction had no significant effect on weld pool shape, it did affect solidification. However, weld speed affected both shape and solidification. Figure 2.11a and Figure 2.12a compare the weld pool shape of a 4.2 mm/s weld and a 42 mm/s weld, where increasing weld speed compressed the weld pool width and elongated the FZ in the welding direction.[70] Figure 2.11b and Figure 2.12b compare the microstructural differences between the two weld pools made at different speeds. Figure 2.11c and Figure 2.12c are representative microstructures from the top of the weld pool, where the solidification of the rod-like dendrites was observed based on weld speed. The rod-like structure observed is due to the expected cylindrical shape of Fe-15Cr-15Ni dendrites. While the work by David et al. is contained to single-crystal specimens of just one alloy, it reveals the significant role that welding parameters play in the solidification of a weld pool.[70]

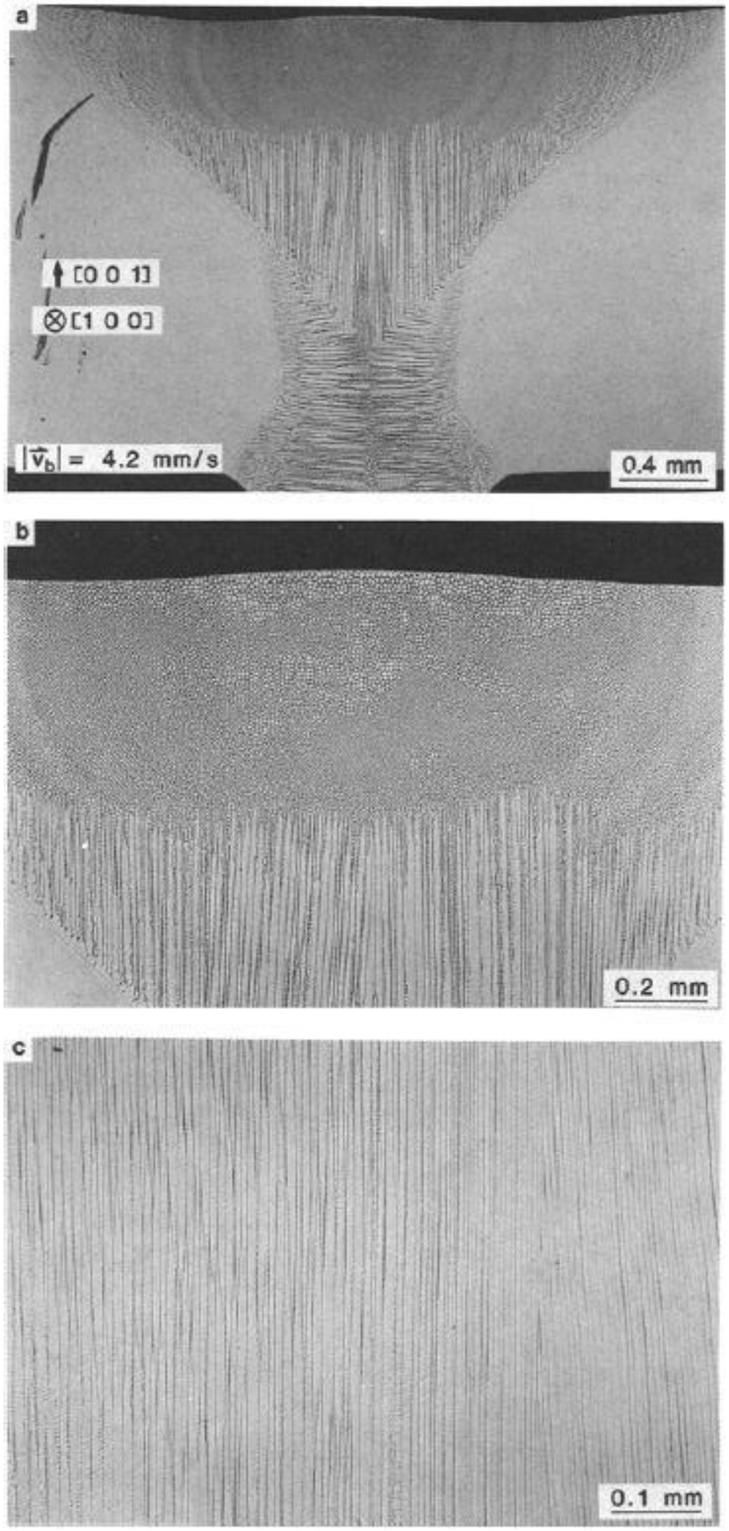

Figure 2.11: Transverse cross-section of weld made at 4.2 mm/s, on single crystal Fe-15Cr-15Ni (a) and a higher magnification image revealing more detail in the top of the weld pool (b), and the microstructure from the top, where welding direction is from the bottom to the top of the image (c). From David et. al.[70]

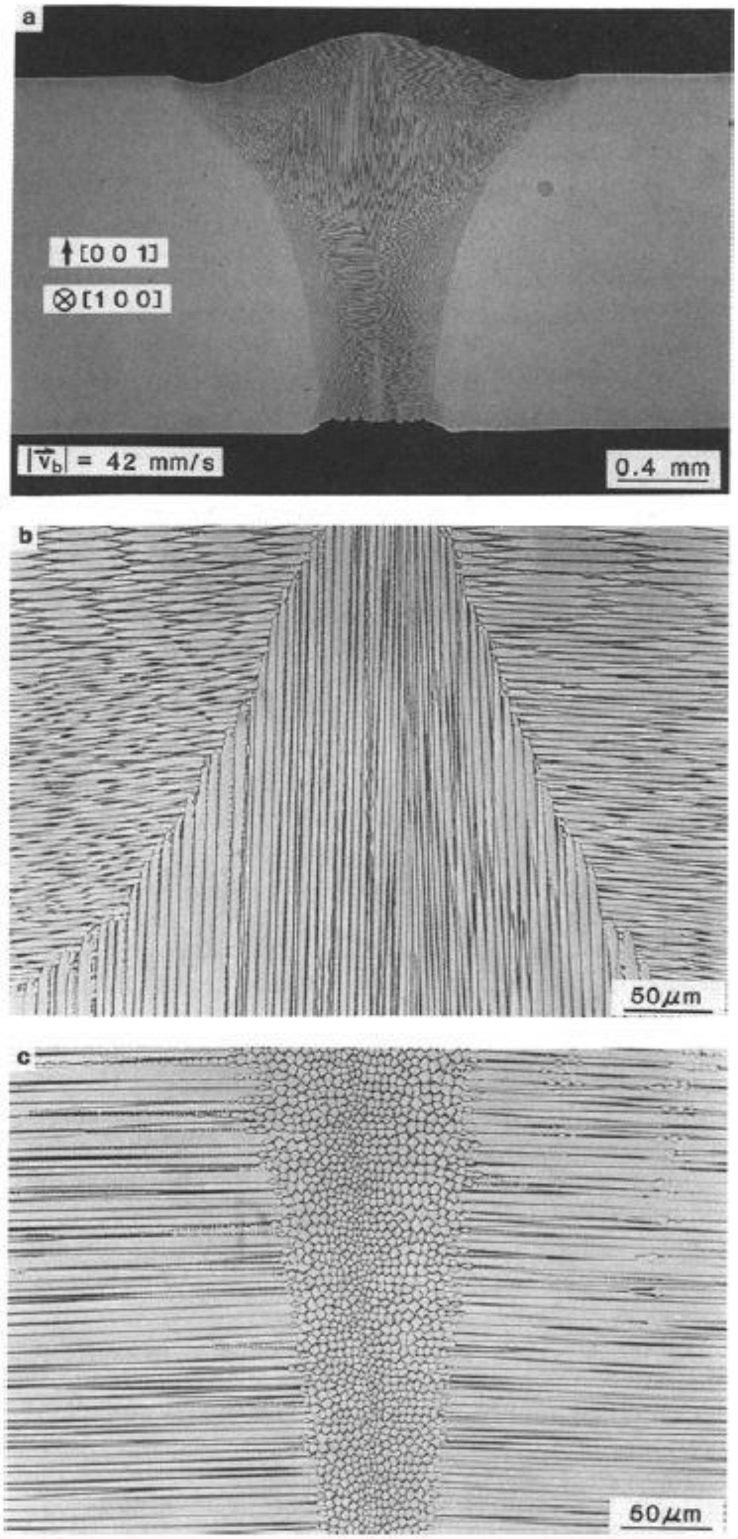

Figure 2.12: Transverse cross-section of weld made at 42 mm/s, on single crystal Fe-15Cr-15Ni (a) and a higher magnification image revealing more detail in the top of the weld pool (b), and the microstructure from the top, where welding direction is from the bottom to the top of the image (c). From David et. al.[70]

Electron backscatter diffraction (EBSD) is a microstructure analysis technique used with scanning electron microscopy (SEM) or transmission electron microscopy (TEM) to measure the crystallographic orientation of grains in a specimen.[71,72] When combined with software analysis, EBSD becomes a strong microstructural analysis tool, allowing the user to develop orientation maps, which can assist in the understanding of microstructural texture, where highly textured microstructures have grains with similar orientations. Highly textured microstructures may give insight into nucleation and growth during solidification, where heterogeneous nucleation may occur in a highly textured weld pool, as grains nucleate and grow off of the surface of other grains, but homogeneous nucleation may occur more readily in a weld pool that shows little texture. David et al. was able to utilize microstructural information to determine how welding parameters affected the solidification of single crystal Fe-15Cr-15Ni, and similarly, with enough information, predictive models could also be developed for ceramics, such that optimal fusion zone microstructures can be obtained based on welding parameters.[73-78]

2.5 ZIRCONIUM DIBORIDE

2.5.1 Crystal Structure. ZrB_2 has a hexagonal crystal structure, type AlB_2, belonging to the P6/mmm space group.[1,32] The unit cell consists of one ZrB_2 formula unit, with two Zr layers and one B layer (Figure 2.13). Each Zr atom is surrounded by six Zr neighbors (in plane) and 12 B (six above and below) neighbors. Each B atom is surrounded by three B neighbors (in plane) and six Zr neighbors (three above and below). The lattice parameters of ZrB_2 are a=b=3.17 Å and c=3.53 Å, and the calculated theoretical density of ZrB_2 is 6.10 g/cm^3.[1,79-81]

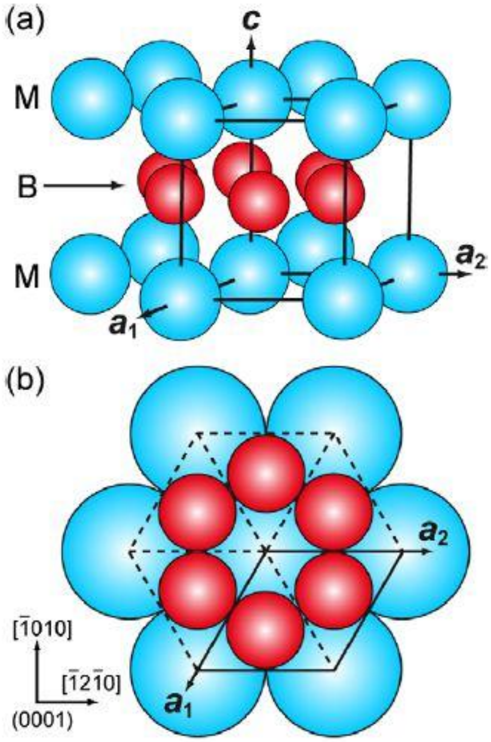

Figure 2.13: (a) Unit cell of ZrB_2 crystal structure with alternating layers of Zr (M) and B. (b) Projection of the crystal along the [0001] is included.[32]

In the transition metal (TM) layer of the AlB_2 type structure, TM-TM bonds are expected to have uniform charge distribution, indicating that Zr-Zr bonding in ZrB_2 is metallic in nature. Within the B layer, B-B bonds exhibit sp^2 hybridization, giving B layers strong covalent bonding characteristics. The electron configuration of Zr is $[Kr]5s^2 4d^2$. The electron configuration of B is $[He]2s^2 2p^1$. In the diboride structure, these electron configurations lead to the donation of two electrons from Zr, and B becomes an acceptor. This gives the Zr-B bonds ionic characteristics, but partial excitation of *d* electrons gives rise to the formation of *spd* hybrid configurations, giving the Zr-B bonds covalent character as well.[1,79,82] Hybridization leads to the separation of empty antibonding states and full, bonding states.[83] Separation of bonding states leads to the formation of a pseudogap, or a sharp valley around the Fermi level, which is exhibited by all Group IV diborides.[79,83] The result is a high cohesive energy, providing the good chemical stability and high melting temperature of ZrB_2.[79,82] Moving away from Group IV leads to the filling of antibonding states, and the valley observed in the density of states shifts away from the Fermi level, observed in Figure 2.14.[1,79,83] For other TM diborides, the shift away from the Fermi level and filling of antibonding states leads to a lowering of the cohesive energy, and non-Group IV diborides exhibit a degradation in properties, such as stiffness and melting temperature, compared to Group IV diborides.[1,79]

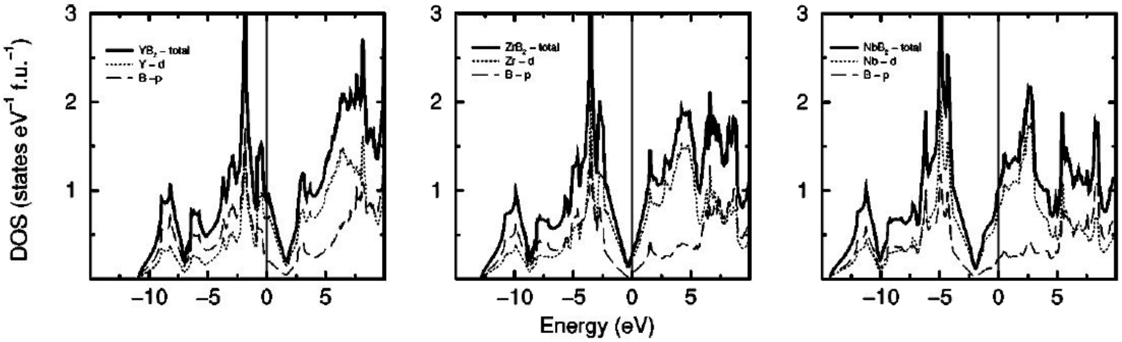

Figure 2.14: Density of states functions for YB_2, ZrB_2, and NbB_2, where ZrB_2 exhibits a pseudogap at the Fermi level. Group III and V (Y and Nb) exhibit a shift in the density of states minima, and a degradation of properties (i.e. melting temperature) is observed for YB_2 and NbB_2 compared to ZrB_2.[79]

2.5.2 Electrical Properties. Due to the bonding nature of its AlB_2 structure, ZrB_2 also exhibits good electrical properties and has even been observed to transition to superconducting at 5.5 K.[84] The room temperature electrical resistivities reported for ZrB_2 range from 6-22 $\mu\Omega\cdot$cm, where the difference between different monolithic ZrB_2 specimens is likely due to impurities.[3,85] The lowest room temperature electrical resistivity for polycrystalline ZrB_2 (6 μΩ·cm) was processed from Zr and B powders by Zhang et al., using a reaction processing method.[3] In contrast, the highest electrical resistivity (22 μΩ·cm), reported by Zimmermann et al., was processed from commercially available powder that had been ball milled with WC milling media. Zimmermann et al. noted that WC contamination was a possible cause for deviation of all reported thermophysical properties.[85]

When considering arc welding, the electrical conductivity of the material may be an issue. In order to determine if ZrB_2 has the potential to be arc welded, ZrB_2 may be compared to different metal compositions that are commonly arc welded. Figure 2.15 compares the electrical resistivities as a function of temperature of ZrB_2 with copper, aluminum, magnesium, 304 stainless steel (304 SS), and Ti6Al4V (common titanium alloy for aerospace applications). The plotted electrical resistivity of ZrB_2 follows that of Zimmermann et al., but with the understanding that pure ZrB_2 has an electrical resistivity near 6 μΩ·cm, closest to that of a pure wrought magnesium (4.48 μΩ·cm @ 25°C, interpolated from data).[85,86] With other regularly welded metals having higher electrical resistivities, electrical resistivity should not hinder the potential for arc welding as a fusion joining technique for ZrB_2 or ZrB_2 based ceramics.

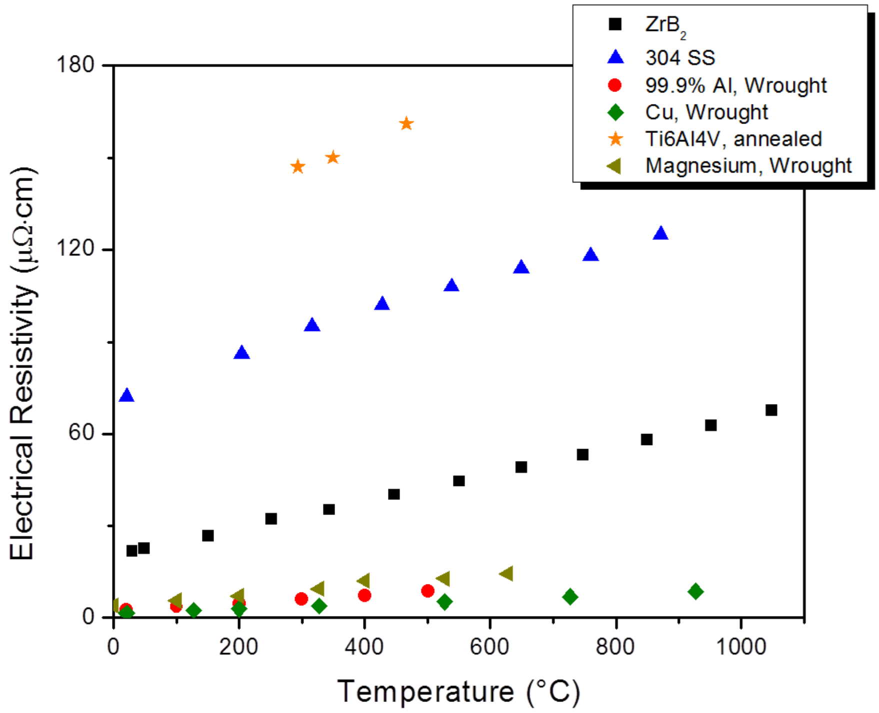

Figure 2.15: Electrical resistivity of ZrB_2 compared to some commonly arc welded metals. ZrB_2 electrical resistivity data from Zimmermann et al. and metals electrical resistivity data from ASM Ready Reference: Electrical and Magnetic Properties of Metals.[85,86]

2.6 PARTICULATE CERAMIC COMPOSITES

As demonstrated in the previous section, ZrB_2 has good electrical properties, which makes it a possible candidate ceramic for joining by arc welding. However, one of the concerns when arc welding a ceramic is its susceptibility to thermal shock, where thermal shock being is catastrophic failure of the material due to a sudden or rapid change in temperature across a sample surface, where the temperature change results in the formation of a large thermal gradient across the material. The maximum change in temperature, R, that a brittle material can withstand without initiating cracks, can be described through Equation 2.6, where σ is strength, ν is Poisson’s ratio, E is Young’s modulus, and α is CTE.[87] Assuming that heating of a sample due to arc welding is relatively instantaneous, and using a strength value of 570 MPa, a Poisson's ratio of 0.135, a Young's modulus of 526 GPa, and a CTE of 6.8×10^{-6}/°C, R for ZrB_2 can be calculated to be ~140°C.[6,32,88]

$$R = \frac{\sigma(1-\nu)}{E\alpha} \tag{2.6}$$

To change the behavior of the monolithic material, second phase particulate additions are often added to the microstructure to affect the material properties. In most cases, the mechanical properties are targeted for modification.[89-93] For example, second phase particulate additions are often utilized to improve the fracture toughness of SiC. Monolithic SiC has a fracture toughness of 2-5 $MPa \cdot m^{1/2}$, but through the addition of a secondary phase to promote crack deflection and grain pinning, the fracture toughness of SiC can be boosted to 6-9 $MPa \cdot m^{1/2}$.[94-98] Further, when Griffith criteria for failure (Equation 2.7) is investigated, it can be demonstrated that an increase in fracture toughness (K_{IC}) and a decrease in critical flaw size ("a", assuming a fully dense material where grain size would be the critical flaw) can lead to an increase in the overall strength (σ) of the material.[99,100] Equation 2.7 also takes into account a geometry factor, Y, which is determined by the shape of the critical flaw.[99]

$$K_{IC} = Y\sigma\sqrt{\pi a} \tag{2.7}$$

Particulate additions may also be utilized as a source of microcracking in the microstructure, be it spontaneous or stress-induced microcracking.[89-91,101] In spontaneous microcracking materials, thermal residual stress will arise due to a mismatch of CTE between two phases, or even between crystallographic directions. When the stresses become large enough, a microcrack may develop.[101] In TiB_2, spontaneous microcracking can occur due to the difference in the CTE between the “a” (6.4×10^{-6}/°C) and “c” (9.3×10^{-6}/°C) directions of the hexagonal crystal.[32] Ferber et al. demonstrated the effect spontaneous microcracking had on TiB_2 where TiB_2 with a grain size of 40 μm that exhibited spontaneous microcracking had a K_{IC} of 3.7 $MPa \cdot m^{1/2}$, and TiB_2 with a grain size of ~5 μm (no spontaneous microcracking) had a K_{IC} of 5.8 $MPa \cdot m^{1/2}$.[102] Alternatively, in a material that exhibits stress induced microcracking, the stresses that develop due to CTE mismatch are not large enough to cause fracture, but with the application of a tensile stress, formation of microcracks become favorable.[101] Stress-induced microcracking reduces stress in the material and shield a propagating crack tip, resulting in toughness enhancement.[89,103]

2.6.1 Particulate Additions to ZrB_2. As with SiC and TiB_2, particulate additions are often added to ZrB_2 to change its properties. Table 2.1 lists several ZrB_2 materials (monolithic and particulate composites) and includes information such as density, strength, fracture toughness, and grain size. Comparing the strength of monolithic ZrB_2 from Neuman et al. and Chamberlain et al., it can be observed that a decrease in ZrB_2 grain size (19 to 6 μm) led to an increase in the flexure strength of ZrB_2 (380 MPa to 570 MPa).[6,104] The decrease in grain size reduces the critical flaw size, affecting the strength (Equation 2.7). As previously mentioned, grain pinning is one of the advantages of particulate phase additions and was exhibited by Chamberlain et al. when the grain size of ZrB_2 was reduced from ~6 μm for monolithic ZrB_2 to ~3 μm for ZrB_2-SiC particulate composites.[6] Without an increase in fracture toughness, a reduction in grain size would affect the strength, but Chamberlain et al. also reported an increase in the fracture toughness of ZrB_2-SiC compared to monolithic ZrB_2. Additions of 10 and 30 vol% SiC led to increased K_{IC} values of 4.1 $MPa{\cdot}m^{1/2}$ (10 vol%) and 5.3 $MPa{\cdot}m^{1/2}$ (30 vol%) for ZrB_2-SiC ceramics, compared to a fracture toughness of 3.5 $MPa{\cdot}m^{1/2}$ for monolithic ZrB_2. Reporting an overall decrease in grain size and an increasing in K_{IC} with increasing SiC content, Chamberlain et al. also observed increasing strength with increasing SiC content, where monolithic ZrB_2 had a reported flexure strength of ~570 MPa and ZrB_2 containing 30 vol% SiC had a reported strength of ~1.1 GPa. Neuman et al. also reported an increase in the strength of ZrB_2 containing 30 vol.% SiC (680 MPa) compared to monolithic ZrB_2 (380 MPa).[104,105] While Neuman et al. did not report a K_{IC} of monolithic ZrB_2 for comparison, the grain size of ZrB_2 was observed to decrease, from 19 μm for ZrB_2 to 1.9 μm for the ZrB_2-SiC composite, and it can be said that the composite ceramic exhibited grain pinning effects, boosting strength by reducing the critical flaw size.

Table 2.1 Microstructure and Mechanical Properties of ZrB_2 Based Ceramics

Composition (vol%)	**Density (%)**	**σ (MPa)**	**K_{IC} ($MPa \cdot m^{1/2}$)**	**ZrB_2 Grain Size (μm)**
ZrB_2[104]	99.4	381±41	-	19.4±13.0
ZrB_2[6]	99.8	565±53	$3.5\pm0.3^{\psi}$	~6
ZrB_2[106]	87	350±40	$2.4\pm0.2^{\dagger}$	-
ZrB_2[107]	87	351±31	$2.35\pm0.15^{\dagger}$	-
ZrB_2-Ni[106]	98	370±25	$3.4\pm0.4^{\dagger}$	-
ZrB_2-5AlN[106]	92	580±80	$3.1\pm0.5^{\dagger}$	-
ZrB_2-20$MoSi_2$[108]	99.1	531±46	$2.3\pm0.2^{\infty}$	2-3
ZrB_2-20$MoSi_2$[109]	95.2	493^{*}	4.3^{ϕ}	
ZrB_2-10SiC[110]	~100	835±35	$4.8\pm0.2^{\dagger}$	~3
ZrB_2-10SiC[6]	93.2	713±48	$4.1\pm0.3^{\psi}$	~3
ZrB_2-25SiC[4]	97.7	$506\pm43^{*}$	4.0^{∞}	3-10
ZrB_2-30SiC[111]	97.2	1063±91	$5.5\pm0.3^{\psi}$	~2
ZrB_2-30SiC[112]	>99	1150±115	-	8-10 (max)
ZrB_2-30SiC[6]	99.4	1089±152	$5.3\pm0.5^{\psi}$	~3
ZrB_2-30SiC[105]	~100	682±98	$4.9\pm0.4^{\dagger}$	1.9±0.9
ZrB_2-5Si_3N_4[106]	98	595±90	$3.7\pm0.1^{\dagger}$	-
75ZrB_2-20$MoSi_2$-5SiC[113]	~100	-	$3.4\pm0.4^{\infty}$	1.9±0.4
64ZrB_2-16MoSi-20ZrO_2[109]	98.5	968	6.3^{ϕ}	2
74ZrB_2-21SiC-4ZrC[114]	97.3	747±101	$5.2\pm0.4^{\infty}$	-
48.7ZrB_2-48.9TiB_2-2.4Ni[115]	~100	599±167	$4.09\pm0.14^{\dagger}$	-
80.4ZrB_2-17TiB_2-2.6Ni[115]	99.6	643±86	$4.53\pm0.24^{\dagger}$	-
40ZrB_2-37.5HfB_2-19.5SiC-3HfN[116]	~100	765±20	$5.1\pm0.8^{\dagger}$	-

Specimens were tested in 4 point flexure unless otherwise specified * for specimens tested in 3 point flexure. † for K_{IC} measured by cheveron notch method, $^{\infty}$ for K_{IC} measured by the direct crack method, $^{\psi}$ for K_{IC} measured by indentation in bending, $^{\phi}$ for K_{IC} measured by single edge notch beam.

The mechanical properties presented in Table 2.1 demonstrate how particulate toughening can be useful in improving the mechanical properties of ZrB_2. Typically, particulate additions were shown to increase the fracture toughness and decrease grain size, leading to an increase in the strength of the particulate composite over the monolithic. Therefore, particulate additions may be useful in avoiding thermal shock in ceramics during fusion welding, as an increasing strength could increase the thermal shock resistance. This can be demonstrated by calculating R for ZrB_2-30SiC, where utilizing the Young's modulus (484 GPa) and strength (1089 MPa) from Chamberlain et al., a rule of mixtures calculation to determine Poisson's ratio for a ZrB_2-30SiC (0.151), and assuming a negligible difference in CTE between ZrB_2-30SiC and ZrB_2, R increases from ~140°C for ZrB_2 to ~280°C for ZrB_2-30SiC.[6,117]

2.6.2 ZrB_2-ZrC Ceramics. While the addition of SiC particles has been shown to be a reliable second phase addition for improving the mechanical properties of ZrB_2, SiC does not melt, but decomposes above 2800°C. Therefore, the conditions associated with arc welding may result in SiC dissociation.[118] Further, a relatively low temperature eutectic is observed in the ZrB_2-SiC system at 2270°C, which limits the possible use temperatures of ZrB_2-SiC ceramics.[119] Therefore, a similar system, ZrB_2-ZrC, can provide second phase toughening without the potential for dissociation of the second phase.

ZrB_2 and ZrC are two melting phases that form a binary system, Figure 2.16.[2] ZrB_2 has a melting temperature of 3250°C and ZrC has a range of possible melting temperatures due to the stoichiometric range of ZrC.[1,2] Rudy et al. have also reported that stoichiometric ZrC melts incongruently, and sub-stoichiometric ZrC ($ZrC_{0.88}$) melts congruently at 3430°C.[120] Therefore, the ZrC composition in Figure 2.16 contains a sub-stoichiometric ZrC. The binary system exhibits one invariant reaction, the binary eutectic (liquid→solid 1+solid 2), at a composition of 42 mole% ZrC (39 vol% or 40 wt% ZrC).[2] The ZrB_2-ZrC eutectic temperature was reported to be 2830°C by Rudy and Windish, for $ZrC_{0.88}$.[2] In Figure 2.16 , the liquidus of the ZrC-Liq. region is concave, but should be convex, like the ZrB_2-Liq. region, likely a result of calculations used to determine the curvature of the liquidus.

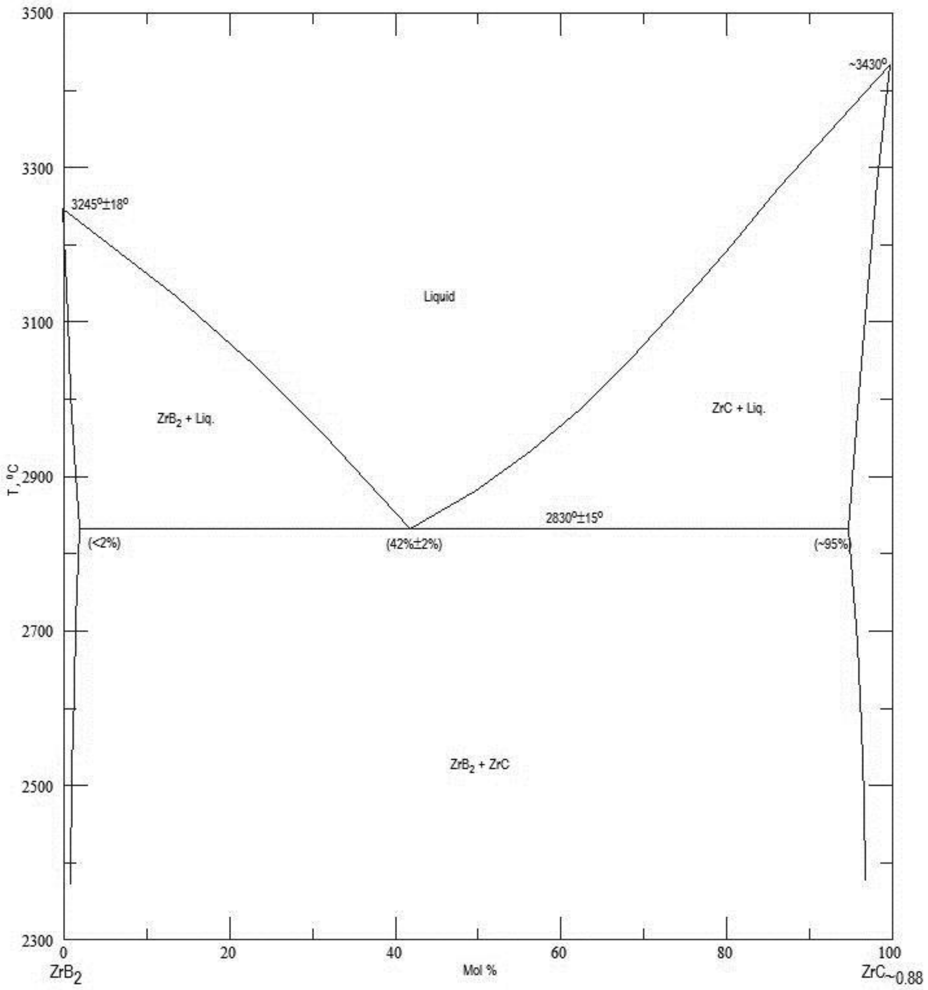

Figure 2.16: Binary phase diagram of the ZrB_2-ZrC system, from Rudy and Windish.[2]

ZrB_2-ZrC ceramics have not been as widely studied as ZrB_2-SiC ceramics, but it has been demonstrated that ZrC additions to ZrB_2 result in improvements in the mechanical properties of ZrB_2, and in some cases, the mechanical properties of a ZrB_2-ZrC particulate composite have been demonstrated to be better than that of ZrB_2-SiC.[121-123] Sorrell et al. produced directionally solidified eutectics of ZrB_2-ZrC by pulling a sintered rod of ZrB_2-ZrC (46 vol% ZrC) through an induction coil, resulting in a lamellae like microstructure.[124] Sorrell et al. measured the fracture toughness of the directionally solidified eutectic and determined that fracture toughness increased with a decreasing interlamellar spacing, where toughness exhibited a maximum at an interlamellar spacing of 1.85 μm.[121] In the transverse direction of eutectic solidification, K_{IC} was measured to be a maximum of 5.4 MPa·m$^{1/2}$, which is similar to conventional particulate reinforced ceramics.[121] Tsuchida and Yamamoto utilized a mechanically assisted reaction process to produce several ZrB_2-ZrC ceramics based on Zr-B-C molar ratios. The K_{IC} of their ZrB_2-ZrC composites ranged from 2.9 MPa·m$^{1/2}$ for a 1:1 mole ZrB_2:ZrC (40 vol% ZrC) to 5.1 MPa·m$^{1/2}$ for an 3:1 ZrB_2:ZrC (22 vol% ZrC).[122] Compared to Sorrell et al., and Tsuchida and Yamamoto, Shim et al. used SPS to densify ZrB_2 40.1 wt% ZrC (39 vol%) and obtained a K_{IC} of 7.4 MPa·m$^{1/2}$.[123] In their high fracture toughness ZrB_2-ZrC, Shim et al. also reported an average ZrB_2 grain size of 1.12 μm.[122]

Based on the reported toughness and ZrB_2 grain size of ZrB_2 with 39 vol% ZrC, the strength of the ceramic can be estimated. Using Equation $K_{IC} = Y\sigma\sqrt{\pi a}$ (2., a scratch-like flaw size of ~6 μm can be calculated for the ZrB_2-30SiC ceramic of Chamerlain et al., toughness of 5.3 MPa·m$^{1/2}$ and a strength of 1089 MPa.[6] Using the same flaw size and shape (Y=1.12 for scratch-like flaw), the strength of ZrB_2 with 39 vol% ZrC can be estimated to be 1522 MPa. Additionally, the Young's modulus and Poisson's ratio of the ZrB_2-ZrC ceramic can be estimated and used to calculate R. A ZrC Young's modulus of 407 GPa and a Poisson's ratio of 0.196 result in a Young's modulus of 480 GPa and a Poisson's ratio of 0.159 for ZrB_2-ZrC (39 vol% ZrC).[32,125] Following the previous calculation for R of ZrB_2-30SiC, the CTE difference between the composite and the monolithic was treated as negligible, and the monolithic ZrB_2 CTE was used to calculate an R of ~390 °C (Equation 2.6) for ZrB_2 with 39 vol% ZrC. It is important to note that the estimated R for ZrB_2 with 39 vol% ZrC is just that, an estimate. But, it does demonstrate that the ZrB_2-ZrC system has the potential to provide better thermal shock resistance than ZrB_2-SiC. Nonetheless, if a ZrB_2-ZrC system provides the same thermal shock resistance as a ZrB_2-SiC ceramic, the ZrB_2-ZrC system contains two melting components, and the potential risk of dissociation from SiC is eliminated.

PAPER

I. PLASMA ARC WELDING OF ZrB_2-20 VOL% ZrC CERAMICS

Derek S. King, Greg E. Hilmas, William G. Fahrenholtz
Missouri University of Science and Technology
Materials Science and Engineering Dept.
Rolla, MO 65409
Corresponding Author Contact
Email: dsk2nf@mst.edu
Phone: 1-573-341-7205
Fax: 1-573-341-6934

ABSTRACT

Zirconium diboride ceramics containing 20 vol% zirconium carbide were preheated to 1450°C and plasma arc welded to produce continuous joints. Arc welding was completed using a current of 198 A, plasma flow rate of 0.75 l/min, and welding speed of ~8 cm/min. Two fusion zones, having penetration depths of 4.4 and 2.3 mm, resulted in different microstructures. One fusion zone contained ZrB_2 crystals, up to ~1 mm in length, and a ZrB_2-ZrC eutectic. The second fusion zone revealed ZrB_2 and ZrC, along with C that was attributed to diffusion from the graphite support used during welding. ZrB_2 and ZrC grains in the latter fusion zone were asymmetric, having an average maximum Feret diameter of 52.4±53.2 and 10.8±8.1 μm, respectively. Hardness, used to identify a heat affected zone for both weldments, increased from 12 GPa at the fusion zone boundary, to the hardness of the parent material, 15.2±0.1 GPa.

1. INTRODUCTION

Most ceramics are electrical insulators. Zirconium diboride (ZrB_2), however, has a reported electrical resistivity of 7.8 $\mu\Omega\cdot$cm at room temperature, which is similar in magnitude to highly conductive metals. The electrical conductivity of ZrB_2 makes arc welding a possible joining technique.[1-6] To be amenable to arc welding, ceramics should mimic metals in as many ways as possible. While low electrical resistivity is one factor for arc welding, mechanical behavior and physical properties must also be considered. In the case of ZrB_2, its high melting temperature (3245°C), high thermal expansion coefficient (CTE; $5.9x10^{-6}/°C$), high Young's modulus (E; 489 GPa), and low fracture toughness (K_{IC}; 3.5 $MPa\cdot m^{1/2}$), increase the risk of thermal shock during rapid heating or cooling, or in the presence of large thermal gradients.[7-11] The risk of thermal shock failure through crack initiation, as described by the R and R' thermal shock parameters can be decreased by reducing E and CTE, and/or increasing thermal conductivity (k). While CTE is not strongly affected by temperature changes, E can be reduced by pre-heating welding specimens (i.e., E decreases as temperature increases).[12-14] Recently, Neuman et al. reported that the Young's modulus of ZrB_2 decreased from 524 GPa at room temperature to 263 GPa at 1600°C, a change of about 50%, approximately doubling crack initiation thermal shock resistance.[12] Rhodes et al. also measured the Young's modulus of ZrB_2 as a function of temperature, and reported a drop from 492 GPa at room temperature to 65 GPa at 2000°C.[14] Further, ZrB_2 ceramics have high thermal conductivities (>50 $W/m\cdot K$ at temperatures up to 2000°C), but further increasing k at elevated temperatures could also mitigate crack initiation controlled thermal shock.[3,15-17]

Even if a material survives rapid heating and the large thermal gradient associated with arc welding, propagation of inherent flaws or flaws generated during welding could cause failure. Therefore, resistance to crack propagation failure is described by the R’” and R’”’ thermal shock parameters should also be considered when arc welding ceramics. To increase crack propagation resistance, the addition of a particulate second phase can increase fracture toughness of ceramics.[18-22] SiC is a common second phase addition that improves the mechanical properties and oxidation resistance of ZrB_2.[7,8,10,11] However, in the ZrB_2-SiC system, the eutectic at 2270°C limits use temperature while the combination of temperature and gas pressure associated with arc welding may result in SiC dissociation above 2800°C.[9,23,24] A similar system, ZrB_2-ZrC, should provide second phase toughening without the potential for vaporization of the second phase. Fracture toughness of ZrB_2-ZrC ceramics has been shown to be higher than ZrB_2-SiC ceramics, with reported K_{IC} values as high as 7.4 MPa·m$^{1/2}$ for ZrB_2 containing 40.1 wt% ZrC (~39 vol%).[25] The eutectic temperature in the ZrB_2-ZrC system is also higher, ~2830°C, compared to ZrB_2-SiC, resulting in higher use temperatures than ZrB_2-SiC.[9] Therefore, the ZrB_2-ZrC system appears to be preferable for fusion joining by arc welding processes compared to other UHTC systems, like ZrB_2-SiC.

Research on the joining of advanced ceramics typically focuses on solid-state and brazing techniques.[26-29] Fusion welding of ceramics has been previously investigated, but research on arc welding was previously limited to the work of Rice, until recent work by Hilmas et al. and King et al.[5,6,30-32] The purpose of the present article is to demonstrate the ability to fusion weld ZrB_2, containing 20 vol% ZrC, by plasma arc welding (PAW), which is the same technique used by King et al. to fusion weld TiB_2 containing 20 vol%

TiC.[32] The electrical properties of ZrB_2 containing 20 vol% ZrC, the conditions necessary to successfully use PAW to fusion weld ZrB_2-20 vol% ZrC, and analysis of the weldment microstructure are presented.

2. EXPERIMENTAL PROCEDURE

ZrB_2-ZrC ceramics with a nominal carbide content of 20 vol% were prepared. Starting powders were mechanically mixed by ball milling ZrB_2 (H.C. Starck; Grade B; Newton, MA) and ZrC (H.C. Starck; Grade B) with 1.25 wt% phenolic resin (Georgia Pacific Chemicals; Atlanta, GA) for a nominal carbon (C) content of 0.50 wt%, or ~1.5 vol%. Milling was carried out in acetone for 2 hours using tungsten carbide media. After milling, the powder slurry was dried using rotary evaporation to minimize segregation of the constituents. Dried powders were then ground and sieved to -60 mesh before hot pressing.

Billets nominally 46.5 mm by 30.0 mm by 5.0 mm of ZrB_2-20 vol% ZrC (ZrB_2-20ZrC) were densified by hot pressing. Hot pressing was performed in a graphite element furnace (Thermal Technology; Model HP20-3060-20; Santa Rosa, CA). The milled and dried powders were loaded into a boron nitride coated graphite die. The powder was heated at a rate of 50°C/min, under a mild vacuum of ~30 Pa (200 millitorr). A one hour isothermal reaction hold at 1650°C under vacuum was performed to remove oxide contamination from the surface of the powders. After the reaction hold, the vacuum atmosphere was switched to flowing argon and a pressing pressure of 32 MPa was applied. A heating rate of 50°C/min was used to reach the final densification temperature of 1980°C. Pressing continued at temperature until recorded ram travel ceased for a period of 10 minutes. Pressed billets were removed from the graphite die and ground to a nominal thickness of 4 mm using a manual surface grinder (Chevalier Machinery Inc.; Model FSG-618; Santa Fe Springs, CA) and a 120 grit diamond grinding wheel (National Diamond Labs; Los Angeles, CA). Surface ground billets were cut using a diamond cutting wheel (National Diamond Labs) into smaller coupons for electrical resistivity measurements and welding. The densities of each coupon were determined using Archimedes method and the relative density was calculated based on rule of mixtures theoretical density for ZrB_2-20ZrC (6.18 g/cm^3). Pressed billets were also machined using an automated surface grinder (Chevalier Machinery Inc.; Model FSG-3A818) to produce test specimens for measuring thermal diffusivity and electrical resistivity.

Electrical resistivity was measured using the van der Pauw method.[33] A ZrB_2-20ZrC specimen was ground into a 25.4 mm disc using a cylindrical grinder (Crystal Lake Grinders; North Fork, CA), and surface ground to a thickness of 1.23 mm. Electrical resistivity measurements were made using a custom four point probe fixture from room temperature up to 500°C in a tungsten element furnace (Thermal Technology; 100-4080-W3).

ZrB_2-20ZrC coupons, nominally 15 mm by 15 mm by 4 mm, were butt welded in a custom welding chamber described by King et al.[32] Prior to welding, a gap was introduced between coupons such that the weld was performed on a 15 mm length side of the coupons. Butt weld gaps were ~0.35 mm and formed by separating diced coupons with 4 layers of double sided tape (3M; Scotch® Double Sided Tape; St. Paul, MN). Taped coupons were placed on a sacrificial graphite disc, then placed on the furnace and aligned with the torch prior to a weld pre-heat. The coupon specimens were covered with a layer of graphite felt and pre-heated to a temperature of ~1450°C. At 1450°C, specimens were uncovered and the torch track was moved such that the torch tip was placed at the edge of the specimen, and at one end of the gap between coupons. The arc was struck to the specimen and welding current was ramped over a period of 8 s from 25 A to the welding current, 198 A for the current study. Once the desired welding current was reached, the torch track was engaged at the slowest available speed of 8 cm/min. At the end of the weld, the current was tapered 10% over a period of 0.25 s followed by a ramp down of the current to 25 A over 12 s. Welded specimens were covered with graphite felt and the furnace was allowed to equilibrate to the pre-heat temperature. The furnace and welded specimens were then cooled at ~30°C/min from the equilibrated temperature to room temperature.

Weldment specimens were cut perpendicular to the welding direction using a manual surface grinder and diamond cutting wheel. Cross-sections were mounted in an epoxy resin and polished to a mirror finish using successively finer diamond abrasives with the finest abrasive being 0.25 μm. Etching of ZrB_2 and ZrC grains was performed in a molten KOH bath at ~210°C for ~5 s. Microstructural analysis of polished cross-sections was performed using optical microscopy (Nikon; Epiphot 200; Tokyo, Japan) and scanning electron microscopy (Hitachi; S-570; Tokyo, Japan). ZrB_2 grain sizes in the parent material and heat affected zones were determined by measuring the areas of at least 1000 grains from each weldment using ImageJ (National Institutes of Health, Bethesda, MD) and calculating the equivalent circular diameter. ZrB_2 grain sizes in the fusion zone were measured as the Feret diameter. Vickers hardness (Struers Inc., Duramin 5, Cleveland, OH) was measured using a load of 9.8 N (1kg) for a dwell time of 10 s. Reported hardness values were an average of 10 indents.

3. RESULTS AND DISCUSSION

3.1 Parent Material Characterization

After hot pressing, the density and microstructure of the parent material (PM) were analyzed. The relative density of the parent material was >99%. The microstructure of the etched PM is shown as a backscatter electron micrograph, Figure 1, and was used to confirm the nominal composition as 80 area% ZrB_2 and 20 area% ZrC. Assuming that the grains are randomly oriented, this confirms the composition of the dense microstructure. Areal image analysis of the PM revealed 1.1±0.4 vol% C, lower than the 1.5 vol% addition of C as a sintering aid. Lot analysis of the starting powder revealed the C content in the ZrC to be 49.5 at% and 0.8 at% in ZrB_2. ZrC phase has a limit of solubility limit of 50 at% C while the solubility limit of C in ZrB_2 is ~2 at%.[9,34,35] Some of the excess C will also be removed through reduction reactions with oxides on the surfaces of ZrB_2 and ZrC particles.[36,37] Therefore, the reduction in observed C content compared to the amount that was added is likely due to dissolution of C into ZrC and/or ZrB_2, and reduction reactions with oxide contamination on the surface of the starting ZrB_2 and ZrC powders. The grain sizes of ZrB_2 and ZrC were also measured after etching a polished cross-section. The average ZrB_2 grain size was 3.3±1.8 μm and the ZrC grain size was 2.2±1.4 μm. The density, carbon content, and grain sizes of ZrB_2 and ZrC are summarized in Table I.

The electrical resistivity was measured to determine how ZrC additions affected the electrical properties of ZrB_2-20ZrC. Single crystal ZrC has a reported electrical resistivity of 191 μΩ·cm at 0 K.[38] Guo et al. observed an increase in the electrical resistivity of ZrC-ZrB_2-SiC ceramics.[39] As ZrB_2 exhibits a transition to a superconducting state at 5.5K, the additions of ZrC could increase electrical resistivity and have a negative effect on the ability to weld ZrB_2.[4] The electrical resistivity of ZrB_2-20ZrC was 10.75 μΩ·cm at room temperature (Table I), and increased to 26.73 μΩ·cm at 500°C. For comparison to a readily welded alloy, the electrical resistivity of 304 stainless steel has been reported to be 72 μΩ·cm at 20°C and 108 μΩ·cm 540°C.[40] While higher than pure ZrB_2, ZrB_2-20ZrC still exhibits good electrical conductivity with an electrical resistivity lower than that of the readily welded 304 stainless steel (72 μΩ·cm), making it a good candidate for arc welding.

3.2 PAW of ZrB_2-20ZrC

Plasma arc welding was used to fusion weld ZrB_2-20ZrC. Figure 2 shows a stitched composite image of optical micrographs of the resulting fusion zone from two ZrB_2-ZrC coupons that were autogenously fusion welded by PAW, using a current of 198 A, a plasma flow rate of 0.75 l/min, and a welding speed of 8 cm/min. The weldment, referred to hereafter as weldment-1, exhibited full penetration through the fusion zone (FZ), and exhibited a keyhole at the end of the weld, a common feature associated with PAW.[41-45] The cross-section, taken 4.1 mm along the joint away from the beginning of the weld, shows a penetration depth of ~4.4 mm, and a measured cross sectional area of ~15.3 mm^2. The FZ of weldment-1 also exhibited a convex surface and a concave interface with the heat-affected zone/parent material (HAZ/PM). With a low electrical resistivity, improved toughness due to second phase ZrC additions, and reduced melting temperature due to the ZrB_2-ZrC eutectic, PAW welding was shown to be a feasible joining method for ZrB_2-ZrC ceramics.

A cross-section taken at 5.4 mm from the beginning of weldment-1 revealed slightly less penetration, ~3.3 mm, showing that the penetration is not consistent throughout the fusion zone. The shape and microstructure of the FZ at 5.4 mm is similar to that shown in Figure 2 and is not shown. Porosity within the FZ and along the FZ interface was observed in both cross-sections. Image analysis of both cross-sections revealed the amount of induced porosity in the FZ was ~2.5 area percent (equivalent to 2.5 vol%, if the pores are randomly oriented). Along the interface, the largest pore diameter was ~310 μm. Within the FZ, the largest pore length was ~280 μm, with an aspect ratio of ~3.8:1. Pores along the FZ interface and within the FZ were likely to be formed by trapping plasma gas in the fusion zone after the closure of the keyhole. Porosity was observed along the interface, and throughout the FZ, where interface pores were circular and FZ pores were asymmetric.

In an effort to limit the formation of porosity within the fusion zone, a notch ~1.1 mm wide and ~1.1 mm deep was added to the graphite disc that supports the specimens during joining. The notch in the graphite was aligned with the gap between the pieces being joined. Figure 3 shows how ZrB_2-20ZrC coupons were arranged for welding without and with a notch in the graphite disc. The notch under the joint should provide an escape route for any plasma gas that penetrates through the joint during keyhole formation, preventing the gas from becoming trapped in the melt.[44-46] Using the same parameters for weldment-1, ZrB_2-20ZrC was joined on a notched graphite disc to produce weldment-2. The resulting FZ is shown as a stitched composite image of optical micrographs in Figure 4. Unlike the first weldment, weldment-2 became attached to the graphite disc during PAW. The resulting weldment-2 FZ cross-section was examined ~4.1 mm from the start of the weld. The weldment had a center depth of ~2.3 mm, and a cross sectional area of ~22.9 mm^2. The FZ had a concave surface, while the FZ retained a concave interface with the HAZ/PM, similar to weldment-1. Porosity along the interface was eliminated using the notched sacrificial graphite disc under the ZrB_2-20ZrC coupons. Welding with a notched graphite spacer resulted in elimination of porosity, but reduced the penetration depth.

3.3 Fusion Zone Characterization

3.3.1 Weldment-1

Carbon is expected to be present in the weldment FZs due to excess C in the PM and residual C from the tape used to separate coupons before welding. Thermal analysis of the tape revealed ~8 wt% residual C after thermal decomposition at 800°C in argon, which is equivalent to ~0.002 g of C for a 15 mm by 4 mm coupon edge. Assuming the FZ cross-section stays constant along the joint, the FZ volume can be extrapolated to be 343 mm^3 (0.343 cm^3), and the additional C from tape would increase the C content by ~0.1 vol%. Based on the evaluation of the PM, 1.1 vol% C, the overall expected composition of the solidified FZ would be 79 vol% ZrB_2, 19.8 vol% ZrC, and 1.2 vol% C. With excess C present in the PM, the compositions lie in the ternary Zr-B-C system.

Even though C was expected to be in the weldments based on the composition of the PM, analysis of the FZ for weldment-1 revealed that no excess C was observed. Hence, the microstructure of the FZ of weldment-1 could be analyzed with the binary ZrB_2-ZrC phase diagram. Exaggerated growth of ZrB_2 (white phase) was observed in weldment-1 and is shown in Figure 5, where ZrB_2 grains grew to lengths up to ~1 mm. Without C in the FZ, ZrB_2 grains were allowed to grow uninhibited as weldment-1 cooled through the ZrB_2 crystallization field in the ZrB_2-ZrC system. Measured aspect ratios ranged from 7.5:1 to 25:1 for ZrB_2 grains within the FZ, where smaller aspect ratio grains were observed at the top surface and the bottom half of the FZ. Growth of smaller aspect ratio grains occurred in greater quantities than larger aspect ratio grains. Nucleation and growth kinetics support these observations, as the surface of the FZ is expected to cool rapidly through convection. Similarly, the bottom side of the FZ is effectively in contact with a heat sink, the graphite spacer. Therefore, higher nucleation rates and lower times for the subsequent grain growth are expected near the top and bottom surfaces of the FZ, which should result in finer grain sizes. In contrast, the middle of the FZ remains hotter since heat must transfer through the solidified outer layers, leading to increased time for grain growth.[32,47] As a consequence, ZrB_2 exhibited exaggerated grain growth within the FZ of weldment-1, where grains grew up to ~1 mm in length with aspect ratios as high as 25:1.

Within the FZ of weldment-1, the binary ZrB_2-ZrC eutectic phase exhibited a cellular eutectic structure containing ZrC rods surrounded by ZrB_2 (Figure 6). Image analysis of the cellular eutectic provided ZrB_2 and ZrC amounts in area percent, which was equated to volume percent due to the rod-like directional solidification. The ZrC content of the eutectic phase in weldment-1 was 43.2±6.1 vol% (47.2±6.7 mole%). Hence, the observed eutectic composition was comparable, within the variance associated with image analysis, to the composition shown on the ZrC-ZrB_2 binary phase diagram, which is 39 vol% (43 mole% ZrC). Even though cooling occurred quickly, the composition and microstructure of the FZ of weldment-1 is consistent with an equilibrium cooling path.[9] This conclusion also agrees with the observed cooling of a TiB_2-20 vol% TiC weldment, reported by King et al, as the measured eutectic composition of 49.5±6.5 vol% TiC (55.4±8.1 mole%) agreed well with the reported eutectic composition of 51 vol% (57 mole%) TiC.[9,32,48]

No C was observed in the FZ of weldment-1. Two of the possible mechanisms for C loss are vaporization during the rapid heating provided by the arc and reaction with oxygen impurities (gaseous or oxides impurities in the ceramic) to form CO. Loss of carbon likely occurred prior to formation of an equilibrium melt, otherwise C would have dissolved in the molten FZ and then reprecipitated during cooling. The absence of C in the weldment-1 FZ, along with the observation that the composition of the ZrB_2-ZrC eutectic was nearly identical to the composition predicted by the phase diagram, shows that the FZ was free of excess C, leaving ZrB_2 and ZrC as the constituent phases of the FZ after solidification. Further, solidification of the FZ appeared to follow an equilibrium cooling path based on its composition and microstructure.

<u>3.3.2 Weldment-2</u>

Microstructural analysis revealed significant differences between weldment-1 and weldment-2. Examination of the microstructure of weldment-2 (Figure 4) at higher magnification showed that the eutectic in the FZ of weldment-2 contained three phases (Figure 7). X-ray diffraction of the FZ of weldment-2 detected only two crystalline phases in the FZ, ZrB_2 and ZrC, despite the observation of three phases by electron microscopy. The FZ of weldment-2 was attached to the sacrificial graphite spacer after PAW, so the black phase in Figure 7 is likely to be C, which would be difficult to detect in XRD due to its low x-ray scattering cross section compared to ZrB_2 and ZrC. Raman spectroscopy was used to characterize the black phase from three different locations within the FZ, and revealed two peaks, one at 1333 cm^{-1} and one at 1585 cm^{-1}, corresponding to the D and G peaks for C.[49] Image analysis of BEI micrographs from the FZ revealed a C content of 11.8±3.5 area% (assumed to be equivalent to vol%). Further, the C in weldment-2 appeared to be contained within the eutectic in the FZ. Attachment of weldment-2 to the graphite disc during welding provided a path for transport of C from the source (i.e., the sacrificial disc) into the FZ. Image analysis of BEI micrographs of the FZ revealed average contents 47.6±14.2 area% ZrB_2, 10.1±4.1 area% ZrC, and 38.1±14.9 area% eutectic. Because the microstructure of the solidified FZ was equiaxed, the area content from the images was equated directly to volume content of the FZ, which was rounded to 50 vol% ZrB_2, 10 vol% ZrC, and 40 vol% eutectic (ZrB_2, ZrC, and C) for further analysis.

Comparing the FZs from weldment-1 (Figure 5) and weldment-2 (Figure 7), grain growth of ZrB_2 within the FZ was hindered when welding on the notched graphite disc. While analysis of the weldment-1 FZ revealed large, elongated grains of ZrB_2, more uniform growth of ZrB_2 and ZrC was observed in weldment-2. From Figure 7, both ZrB_2 and ZrC grew asymmetrically, so their grain sizes are based on the maximum Feret diameter of each grain. Within the FZ of weldment-2, ZrB_2 grains had an average maximum Feret diameter of 52.4±53.2 μm, with a maximum size of 225.9 μm. In the FZ of weldment-2 FZ, ~17% of ZrB_2 grains were over 100 μm, leading to a large standard deviation. The average Feret diameter for ZrC was 10.8±8.1 μm with a maximum size of 59.2 μm. When compared to the length of ZrB_2 grains in the weldment-1 FZ, both ZrB_2 and ZrC had smaller average grain sizes in the weldment-2 FZ.

Two hypotheses are proposed to elucidate why the three phases present in the FZ of weldment-2 affected the growth of ZrB_2, which had a maximum size of ~226 μm for the longest axis in weldment-2 compared to ~1 mm for weldment-1. Analysis of weldment-1 suggested that the FZ followed an equilibrium cooling path, so it is reasonable to assume that weldment-2 also cooled along an equilibrium cooling path. The difference is that the cooling path for weldment-2is controlled by the ZrB_2-ZrC-C ternary system, which has a lower reported eutectic temperature (2360°C) compared to the binary ZrB_2-ZrC system (2830°C) examined for weldment-1.[9] The eutectic composition shown on the ZrB_2-ZrC-C diagram presented by Rudy et al. is 80.6 vol% ZrB_2, 8.1 vol% ZrC, and 11.3 vol% C. However, the C content within the FZ was 29.5 vol%, much greater than the C content shown on the phase diagram. Therefore, the cooling path of the FZ for weldment-2 does not appear to be consistent with the Zr-B-C phase diagram. Instead, the melt composition appeared to change continuously due to C diffusion into the melt during welding and solidification, which, in turn changed the cooling path of the FZ melt. As this occurred ZrB_2 and ZrC likely crystallized individually and simultaneously as the melt composition moved through each respective crystallization field during cooling. Cooling through the ZrB_2 primary crystallization field was likely to be rapid, effectively limiting the time in which ZrB_2 crystals had to nucleate and grow without the presence of the second phase (ZrC) to pin grain growth. Thus, the first hypothesis, which is based on image analysis of the FZ of weldment-2, is that C diffusion into the FZ melt altered the crystallization path of the weldment-2 FZ.

The second hypothesis focuses on the effect of C on the FZ of weldment-2. While no thermochemical data are available for the melting of C, the dissolution of C into the melt pool is endothermic. Not only is melting endothermic (i.e., the enthalpy of fusion (ΔH_f) is positive for all materials), but the enthalpy of mixing (ΔH_{mix}) is also expected to be positive in this system due to the limited solubility of carbon in the solid phases (i.e., carbon exhibits positive deviation from ideal solution behavior and should have a positive enthalpy of mixing). Therefore, energy is absorbed as C dissolves into the FZ of weldment-2, which should decrease the melt pool temperature for the same heat input compared to weldment-1. A decrease in melt pool temperature could promote higher nucleation rates for ZrB_2 and ZrC as well as lower growth rates when compared to weldment-1. While these two hypotheses were presented separately, it is likely that both mechanisms occurred simultaneously during solidification of the FZ. That is to say, the lower melt pool temperature due to the incorporation of C leads to higher nucleation rates for ZrB_2 and ZrC, while a composition shift of the melt pool limits the total time for nucleation of only ZrB_2 as the melt pool composition moves out of the ZrB_2 primary crystallization field. In addition, ZrB_2 growth in the weldment-2 FZ may be hindered by lowering the melt pool temperature, leading to reduced crystal growth rates.

3.4 HAZ/PM Characterization

A distinct HAZ could not be discerned from the PM using optical or electron microscopy. As an alternative, Vickers hardness measurements were made at a depth of ~0.80 mm from the top surface of the FZ to determine if a HAZ was present in either weldment. Hardness of the PM was 15.2±0.1 GPa. Figure 8 is a plot of the hardness measurements of both weldment-1 and weldment-2, which are marked to indicate the locations of the FZ, HAZ, and PM. Within the FZ, the hardness was <12 GPa for both weldments. Across the interface of the FZ, the hardness was ~12 GPa for weldment-1 and ~13.5 GPa for weldment-2. Moving farther away from the FZ into the HAZ, the hardness gradually increased to the value of the PM over a distance of ~1.25 mm for weldment-1 and ~2 mm for weldment-2.

While the HAZ and PM can be identified through hardness measurements, grain size analysis of both the HAZ and PM was carried out to elucidate the microstructural differences between the two regions. More than 1000 ZrB_2 grains were measured for both the HAZ and PM to determine the reported grain size distributions. The average ZrB_2 grain size within the HAZ was 4.9±3.2 μm for weldment-1 and 4.4±2.5 μm for weldment-2, compared to an average ZrB_2 grain size of 3.3±1.8 μm in the PM. The calculated averages of ZrB_2 grain size show a difference between the HAZ and PM for both weldments; however, overlap of the standard deviations may be interpreted such that the difference between the grain sizes is not statistically significant. Therefore, a grain size distribution plot was used to compare the grain sizes in the HAZ for weldment-2 and the PM (Figure 9) to support the assertion that ZrB_2 grain growth occurred in the HAZ. The grain size distributions of the HAZs for weldment-1 and weldment-2 were similar, therefore only one was presented. Figure 9 shows that most of the ZrB_2 grains (92%) in the PM were less than 6 μm in diameter. However, the distribution broadened for ZrB_2 grains within the HAZ, as most of the grains (91%) measured up to 8 μm. Furthermore, less than 2% of the PM distribution lies above the 8 μm grain size. The broadening of the HAZ grain size distribution compared to the PM distribution shows that the average size of ZrB_2 grains increased by ~50% in weldment-1 and ~33% in weldment-2 compared to the PM.

Grain growth within the HAZ explains the difference in hardness between the

HAZ and PM. Increasing grain size leads to adverse effects on measured hardness, especially for anisotropic materials.[50-53] As both weldment-1 and weldment-2 had similar hardness values at the FZ/HAZ interface, grain size appeared to have the largest effect on hardness. However, C diffusion from the FZ of weldment-2 into the surrounding HAZ may adversely affect the hardness.[54,55] Image analysis of carbon content revealed average area fractions of 4.3±2.0% and 1.1±0.4% for the HAZ and PM, respectively. Further, C content within the HAZ ranged from 7.9 to 2.2 vol%, where higher C contents were observed near the FZ. Since the HAZ was wider in weldment-2, 2 mm compared to 1.25 mm for weldment-1, C diffusion from the FZ had an effect on the final width of the weldment-2 HAZ.

4. CONCLUSIONS

Plasma arc welding was used to join dense ZrB_2-20ZrC ceramics that exhibited low electrical resistivity (10.8 $\mu\Omega\cdot$cm). Two different FZ shapes and microstructures were achieved when welded on graphite discs with (weldment-2) and without (weldment-1) a notch placed under the joint. Analysis of weldment-1 revealed the FZ contained two phases, with elongated ZrB_2 grains up to 1 mm in length, surrounded by a ZrB_2-ZrC eutectic (43.2±6.1 vol% ZrC), which had a composition that was comparable to previously reported eutectic compositions (39 vol% ZrC). The weldment-1 FZ appeared to solidify along an equilibrium cooling path. Analysis of weldment-2 revealed three phases in the FZ, identified as ZrB_2, ZrC, and C. It was determined that C diffused into the melt from the underlying graphite disc. ZrB_2 grains in the FZ of weldment-2 were smaller than those in weldment-1, having an average maximum Feret diameter of

52.4±53.2 μm with a maximum size of 225.9 μm. Hardness measurements were used to differentiate the FZ, HAZ, and PM where hardness of the FZ was <12 GPa. Within the HAZ, hardness increased from a value of 12 GPa for weldment-1 and 13.5 GPa for weldment-2 to the hardness of the PM (15.2 GPa) over a distance of 1.25 mm for weldment-1 and 2 mm for weldment-2. Grain size analysis of ZrB_2 revealed growth of ZrB_2 grains to an average of more than 4.5 μm within the HAZ compared to 3.3±1.8 μm in the PM, which could account for the decrease in the hardness of the HAZ. C content within weldment-2 HAZ was observed to decrease from an amount of 7.9 vol% near the FZ to 2.2 vol% near the HAZ/PM increasing the width of the weldment-2 HAZ. Plasma arc welding was viable for fusion joining of ZrB_2-20ZrC ceramics, and may be appropriate for any ceramic with electrical conductivity similar to metals.

ACKNOWLEDGEMENTS

Research was conducted in cooperation with MO-SCI Corporation and supported by AFOSR Grant # FA9550-12-C-0060.

REFERENCES

[1]M. Rahman, C. C. Wang, W. Chen, S. A. Akbar, and C. Mroz, "Electrical Resistivity of Titanium Diboride and Zirconium Diboride," *J. Am. Ceram. Soc.,* **78**[5] 1380-82 (1995).

[2]F. Monteverde, A. Bellosi, and S. Guicciardi, "Processing and properties of zirconium diboride-based composites," *J. Eur. Ceram. Soc.,* **22**[3] 279-88 (2002).

[3]M. J. Thompson, W. G. Fahrenholtz, and G. E. Hilmas, "Elevated Temperature Thermal Properties of ZrB_2 with Carbon Additions," *J. Am. Ceram. Soc.,* **95**[3] 1077-85 (2012).

[4]V. A. Gasparov, N. S. Sidorov, I. I. Zver'kova, and M. P. Kulakov, "Electron transport in diborides: Observation of superconductivity in ZrB_2," *Journal of Experimental and Theoretical Physics Letters,* **73**[10] 532-35 (2001).

[5]R. W. Rice, "Joining of Ceramics," pp. 69-111 in Advances in joining technology: proceeding of the 4th Army Materials Technology Conference, Boston, MA, 1976.

[6]G. E. Hilmas, W. G. Fahrenholtz, J. L. Watts, and H. J. Brown-Shaklee, "Ceramic welds, and a method for producing the same," U.S. Patent 8,715,803, (2014).

[7]W. G. Fahrenholtz, G. E. Hilmas, I. G. Talmy, and J. A. Zaykoski, "Refractory Diborides of Zirconium and Hafnium," *J. Am. Ceram. Soc.,* **90**[5] 1347-64 (2007).

[8]A. L. Chamberlain, W. G. Fahrenholtz, G. E. Hilmas, and D. T. Ellerby, "High-Strength Zirconium Diboride-Based Ceramics," *J. Am. Ceram. Soc.,* **87**[6] 1170-72 (2004).

[9]E. Rudy and S. Windish, "Ternary Phase Equilibria in Transition Metal-Boron-Carbon-Silicon System: Part V. Compendium of Phase Diagram Data." in**.** Air Force Materials Laboratory, AFML-TR-65-2, Wright Patterson Air Force Base, OH, 1966.

[10]J. W. Zimmermann, G. E. Hilmas, and W. G. Fahrenholtz, "Thermal shock resistance of ZrB_2 and ZrB_2–30% SiC," *Mater. Chem. Phys.,* **112**[1] 140-45 (2008).

[11]F. Monteverde and L. Scatteia, "Resistance to Thermal Shock and to Oxidation of Metal Diborides–SiC Ceramics for Aerospace Application," *J. Am. Ceram. Soc.,* **90**[4] 1130-38 (2007).

[12]E. W. Neuman, G. E. Hilmas, and W. G. Fahrenholtz, "Strength of Zirconium Diboride to 2300°C," *J. Am. Ceram. Soc.,* **96**[1] 47-50 (2013).

[13]J. B. Wachtman and D. G. Lam, "Young's Modulus of Various Refractory Materials as a Function of Temperature," *J. Am. Ceram. Soc.,* **42**[5] 254-60 (1959).

[14]W. H. Rhodes, E. V. Clougherty, and D. Kalish, "Research and development of refractory oxidation-resistant diborides. Part II. Volume IV. Mechanical properties." in**.** AFML-TR-68-190 (Pt. 2)(Vol. 4), Wright Patterson Air Force Base, OH, 1970.

[15]M. Ikegami, K. Matsumura, S. Q. Guo, Y. Kagawa, and J. M. Yang, "Effect of SiC particle dispersion on thermal properties of SiC particle-dispersed ZrB_2 matrix composites," *J. Mater. Sci.,* **45**[19] 5420-23 (2010).

[16]E. Zapata-Solvas, D. D. Jayaseelan, P. M. Brown, and W. E. Lee, "Thermal properties of La_2O_3-doped ZrB_2- and HfB_2-based ultra-high temperature ceramics," *J. Eur. Ceram. Soc.,* **33**[15–16] 3467-72 (2013).

[17]L. Zhang, D. A. Pejaković, J. Marschall, and M. Gasch, "Thermal and Electrical Transport Properties of Spark Plasma-Sintered HfB_2 and ZrB_2 Ceramics," *J. Am. Ceram. Soc.,* **94**[8] 2562-70 (2011).

[18]W. H. Gu, K. T. Faber, and R. W. Steinbrech, "Microcracking and R-curve behavior in SiC-TiB_2 composites," *Acta Metall. Mater.,* **40**[11] 3121-28 (1992).

[19]D. J. Green, "Stress-Induced Microcracking at Second-Phase Inclusions," *J. Am. Ceram. Soc.,* **64**[3] 138-41 (1981).

[20]N. Claussen, "Fracture Toughness of Al_2O_3 with an Unstabilized ZrO_2 Dispersed Phase," *J. Am. Ceram. Soc.,* **59**[1-2] 49-51 (1976).

[21]R. W. Steinbrech, "Toughening mechanisms for ceramic materials," *J. Eur. Ceram. Soc.,* **10**[3] 131-42 (1992).

[22]D. J. Green, "Critical Microstructures for Microcracking in Al_2O_3-ZrO_2 Composites," *J. Am. Ceram. Soc.,* **65**[12] 610-14 (1982).

[23]A. H. Heuer and V. L. K. Lou, "Volatility Diagrams for Silica, Silicon Nitride, and Silicon Carbide and Their Application to High-Temperature Decomposition and Oxidation," *J. Am. Ceram. Soc.,* **73**[10] 2789-803 (1990).

[24]S. S. Ordan'yan, A. I. Dmitriev, and E. S. Moroshkina, *Inorg. Mater.,* **25**[10] 1487-89 (1989).

[25]S. H. Shim, K. Niihara, K. H. Auh, and K. B. Shim, "Crystallographic orientation of ZrB_2-ZrC composites manufactured by the spark plasma sintering method," *Journal of Microscopy,* **205**[3] 238-44 (2002).

[26]W. R. Pinc, M. Di Prima, L. S. Walker, Z. N. Wing, and E. L. Corral, "Spark Plasma Joining of ZrB_2–SiC Composites Using Zirconium–Boron Reactive Filler Layers," *J. Am. Ceram. Soc.*, **94**[11] 3825-32 (2011).

[27]M. Singh and R. Asthana, "Joining and integration of ZrB_2-based ultra-high temperature ceramic composites using advanced brazing technology," *J. Mater. Sci.*, **45**[16] 4308-20 (2010).

[28]L. M. Nguyen, D. Leguillon, O. Gillia, and E. Riviere, "Bond failure of a SiC/SiC brazed assembly," *Mechanics of Materials,* **50**[0] 1-8 (2012).

[29]M. Singh, T. Matsunaga, H.-T. Lin, R. Asthana, and T. Ishikawa, "Microstructure and mechanical properties of joints in sintered SiC fiber-bonded ceramics brazed with Ag–Cu–Ti alloy," *Materials Science and Engineering: A*, **557**[0] 69-76 (2012).

[30]G. N. Mikhailova, B. P. Mikhailov, and A. V. Troitskii, "Laser welding of HTSC ceramics," *Laser Physics Letters*, **1**[10] 525-27 (2004).

[31]M. Ikeda, "Ceramics Welding with Laser," *Taikabutsu Overseas*, **5**[3] 27-33 (1985).

[32]D. S. King, G. E. Hilmas, and W. G. Fahrenholtz, "Plasma Arc Welding of TiB_2-20 vol.% TiC," *J. Am. Ceram. Soc.*, **97**[1] 56-59 (2014).

[33]ASTM (ASTM International), "Standard Test Methods for Measuring Resistivity and Hall Coefficient and Determining Hall Mobility in Single-Crystal Semiconducters", ASTM Standard F76-08, West Conshohocken, PA., (2008).

[34]L. N. Grossman, "High-Temperature Thermophysical Properties of Zirconium Carbide," *J. Am. Ceram. Soc.,* **48**[5] 236-42 (1965).

[35]T. Tsuchida, M. Kawaguchi, and K. Kodaira, "Synthesis of ZrC and ZrN in air from mechanically activated Zr·C powder mixtures," *Solid State Ionics,* **101–103, Part 1**[0] 149-54 (1997).

[36]S. C. Zhang, G. E. Hilmas, and W. G. Fahrenholtz, "Pressureless Densification of Zirconium Diboride with Boron Carbide Additions," *J. Am. Ceram. Soc.,* **89**[5] 1544-50 (2006).

[37]S. Zhu, W. G. Fahrenholtz, G. E. Hilmas, and S. C. Zhang, "Pressureless Sintering of Zirconium Diboride Using Boron Carbide and Carbon Additions," *J. Am. Ceram. Soc.*, **90**[11] 3660-63 (2007).

[38]F. A. Modine, T. W. Haywood, and C. Y. Allison, "Optical and electrical properties of single-crystalline zirconium carbide," *Physical Review B,* **32**[12] 7743-47 (1985).

[39]S.-Q. Guo, Y. Kagawa, T. Nishimura, D. Chung, and J.-M. Yang, "Mechanical and physical behavior of spark plasma sintered ZrC–ZrB_2–SiC composites," *J. Eur. Ceram. Soc.*, **28**[6] 1279-85 (2008).

[40]A. S. M. International, "ASM Ready Reference: Electrical and Magnetic Properties of Metals." ASM International: Materials Park, OH, (2000).

[41]C. S. Wu, C. B. Jia, and M. A. Chen, "A Control System for Keyhole Plasma Arc Welding of Stainless Steel Plates with Medium Thickness," *Supplement to the Welding Journal*, **89** 225-31 (2010).

[42]Z. Liu, C. S. Wu, and J. Gao, "Vision-based observation of keyhole geometry in plasma arc welding," *International Journal of Thermal Sciences*, **63**[0] 38-45 (2013).

[43]H. G. Fan and R. Kovacevic, "Keyhole formation and collapse in plasma arc welding," *J. Phys. D: Appl. Phys.*, **32**[22] 2902-09 (1999).

[44]Z. M. Liu, C. S. Wu, and M. A. Chen, "Visualizing the influence of the process parameters on the keyhole dimensions in plasma arc welding," *Meas. Sci. Technol.*, **23**[10] (2012).

[45]Y. M. Zhang and S. B. Zhang, "Observation of the keyhole during plasma arc welding," *Welding Journal*, **78**[2] 53s-58s (1999).

[46]T. Zhang, C. S. We, and Y. Feng, "Numerical Analysis of Heat Transfer and Fluid Flow in Keyhole Plasma Arc Welding," *International Journal of Computation and Methodology*, **60**[8] 685-98 (2011).

[47]E. S. Machlin, pp. 263-88. in An Introduction to Aspects of Themodynamics and Kinetics Relevant to Materials Science**.** Elsevier, Oxford, UK, 2007.

[48]S. S. Ordan'yan, V. I. Unrod, and A. I. Avgustinik, "Reactions in the System TiC_x-TiB_2," *Sov. Powder Metall. Met. Ceram.*, **14**[9] 729-31 (1975).

[49]P. V. Huong, "Structural studies of diamond films and ultrahard materials by Raman and micro-Raman spectroscopies," *Diamond Relat. Mater.*, **1**[1] 33-41 (1991).

[50]A. Krell, "A new look at grain size and load effects in the hardness of ceramics," *Mater. Sci. Eng., A* 277-84 (1998).

[51]A. Krell, "A new look at the influences of load, grain size and grain boundaries on the room temperature hardness of ceramics," *International Journal of Refractory Metals and Hard Materials*, **16** 331-35 (1998).

[52]F. Monteverde and A. Bellosi, "Microstructure and Properties of an HfB_2-SiC Composite for Ultra High Temperature Applications," *Advanced Engineering Materials,* **6**[5] 331-36 (2004).

[53]W.-M. Guo, Z.-G. Yang, and G.-J. Zhang, "Effect of Carbon Impurities on Hot-Pressed ZrB_2–SiC Ceramics," *J. Am. Ceram. Soc.*, **94**[10] 3241-44 (2011).

[54]S. Zhu, W. G. Fahrenholtz, G. E. Hilmas, and S. C. Zhang, "Pressureless sintering of carbon-coated zirconium diboride powders," *Materials Science and Engineering: A*, **459**[1–2] 167-71 (2007).

[55]M. Sakai, Y. Nakano, and S. Shimizu, "Elastoplastic Indentation on Heat-Treated Carbons," *J. Am. Ceram. Soc.*, **85**[6] 1522-28 (2002).

Table I: Properties of ZrB_2-20ZrC Parent Material

Material	ρ (%)	C Content (vol%)	ZrB_2 Grain Size (μm)	ZrC Grain Size (μm)	Room Temp. Electrical Resistivity (μΩ·cm)
ZrB_2-20ZrC	>99	1.1±0.4	3.3±1.8	2.2±1.4	10.75

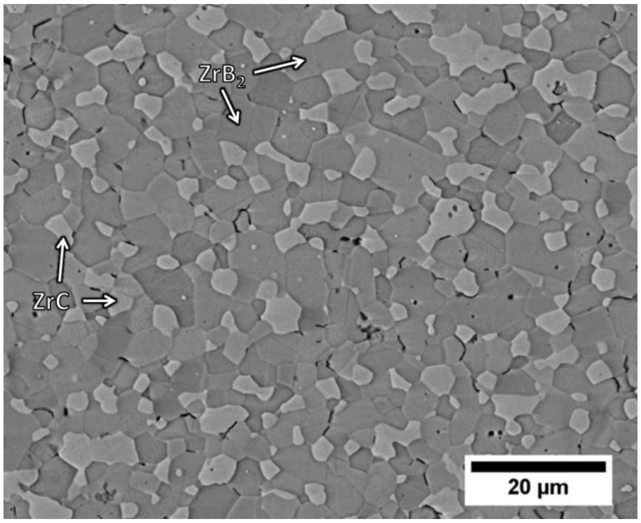

Figure 1: Backscattered electron image of etched ZrB_2-20ZrC parent material. ZrB_2 appears dark grey, ZrC appears light grey, and C/porosity appears black.

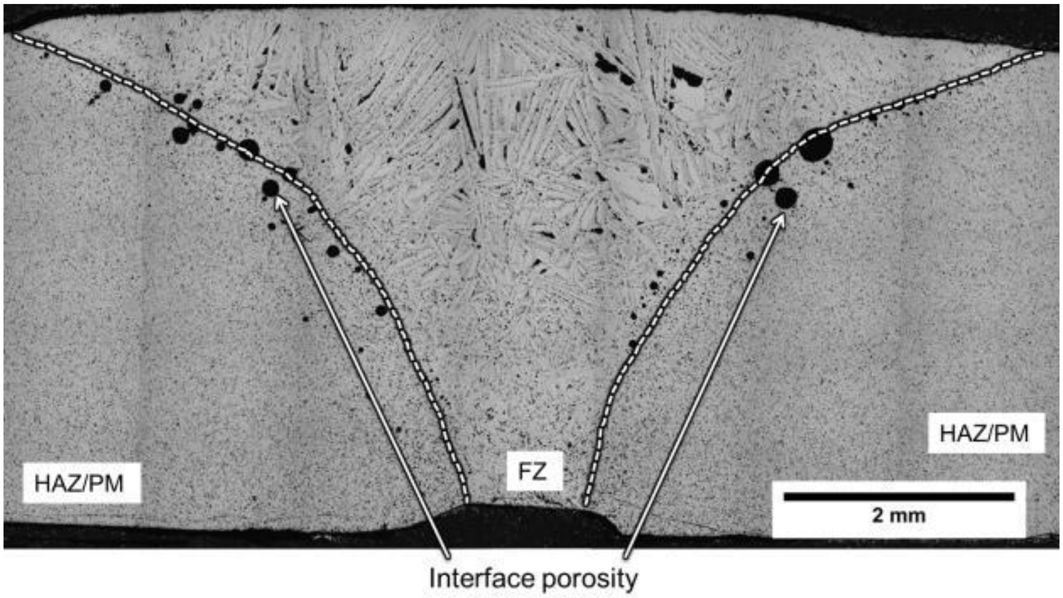

Figure 2: Cross-section of ZrB_2-20ZrC FZ taken ~4.1 mm from the start of the weld. Induced porosity (black) occurs at the interface of the FZ and the HAZ/PM.

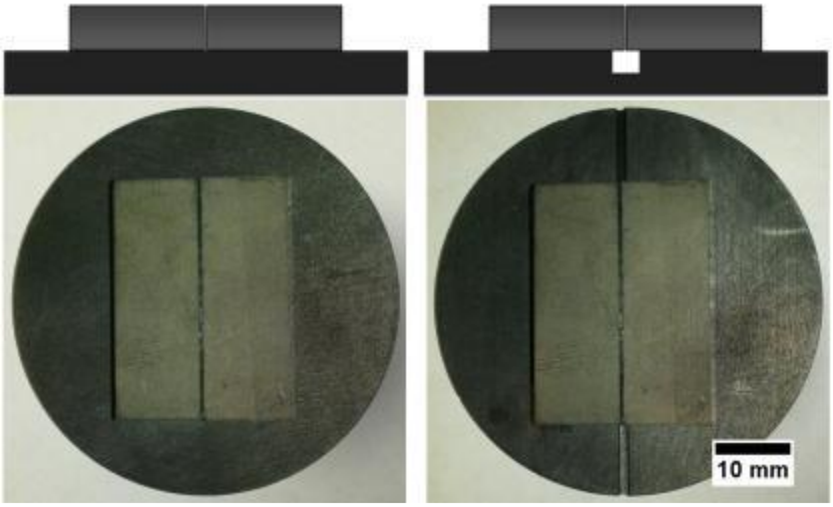

Figure 3: Schematic of graphite support disc (black) and ZrB_2-20ZrC (grey) coupons without (top) and with (bottom) a notch for escape of plasma gas during PAW.

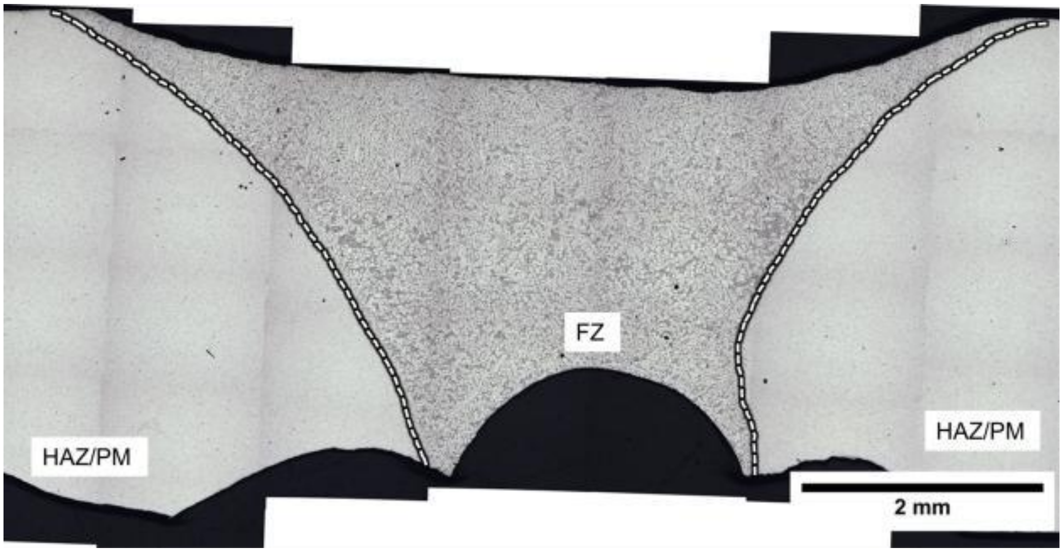

Figure 4: Cross-section of ZrB_2-20ZrC FZ taken ~4.1 mm from the start of the weld. Minimal porosity (black) was observed throughout the microstructure.

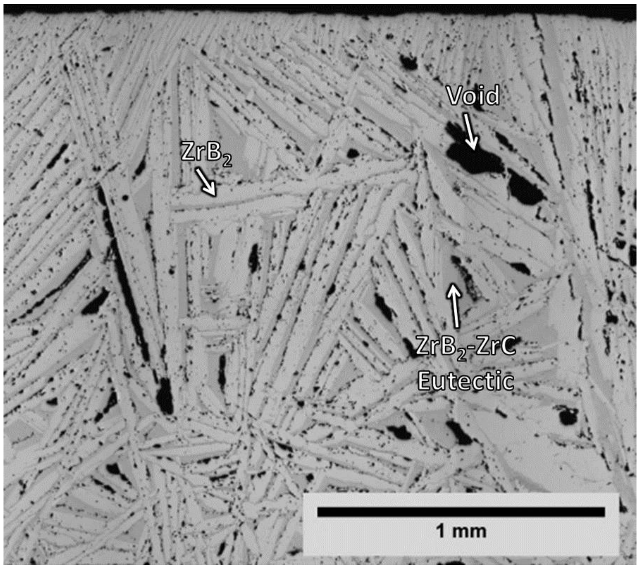

Figure 5: Optical image of weldment-1 FZ exhibiting exaggerated growth of ZrB_2 (white) and void (black) formation in the FZ.

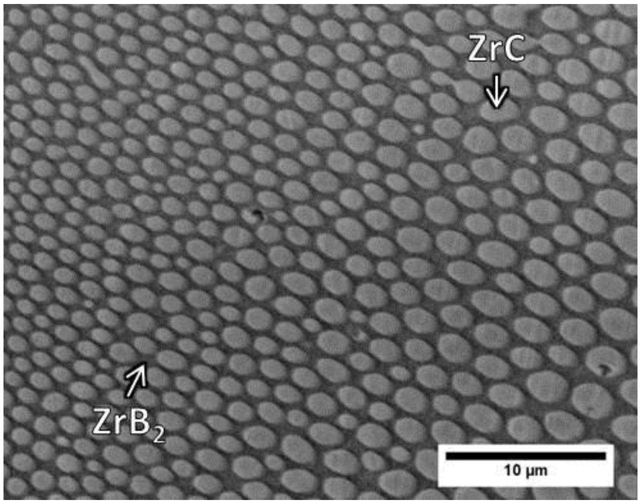

Figure 6: BEI of directionally solidified ZrB_2-ZrC eutectic in weldment-1. ZrC appears light grey and forms rods, solidifying in the direction perpendicular to the cross-section.

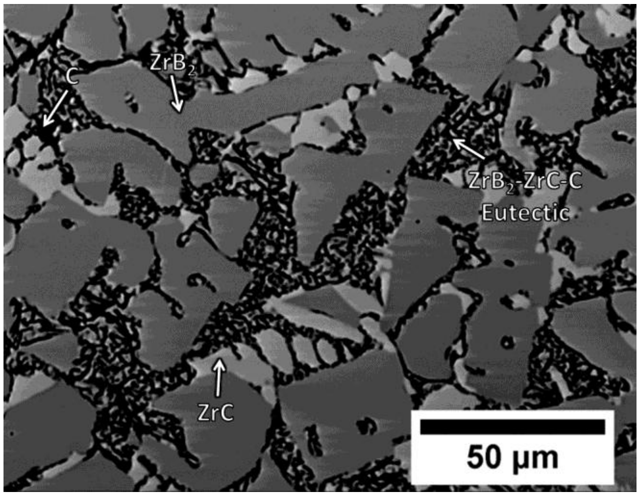

Figure 7: BEI image of the weldment-2 FZ showing the presence of three phases, ZrB_2 (dark grey), ZrC (light grey), and C (black).

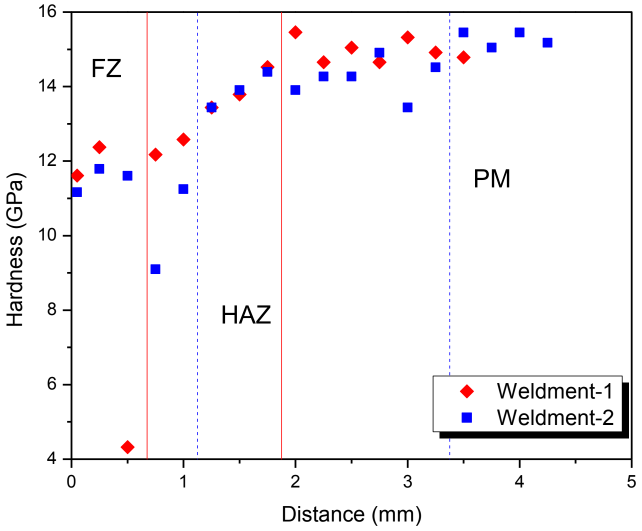

Figure 8: Hardness across the weldments. HAZ widths of ~1.25 and ~2 mm were identified for weldment-1 and welment-2, respectively, as shown by the solid (weldment-1) and dashed (weldment-2) vertical lines**.**

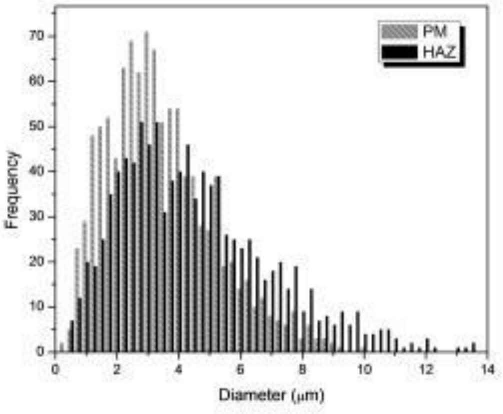

Figure 9: Grain size distributions of the HAZ and PM for ZrB_2 in weldment-2, showing growth of ZrB_2 within the HAZs.

II. MECHANICAL BEHAVIOR AND APPLICATIONS OF ARC WELDED CERAMICS

Derek S. King, Greg E. Hilmas, William G. Fahrenholtz
Missouri University of Science and Technology
Materials Science and Engineering Dept.
Rolla, MO 65409
Corresponding Author Contact
Email: dsk2nf@mst.edu
Phone: 1-573-341-7205
Fax: 1-573-341-6934

ABSTRACT

Zirconium diboride and zirconium carbide based ceramics were joined by plasma arc welding to demonstrate the versatility of this technique. A parent material composition consisting of ZrB_2 with 20 vol% ZrC was hot pressed to near full density, sectioned to produce specimens for welding, and welded together to produce billets for mechanical property studies. The four-point flexure strength of the parent material was ~660 MPa, while the strength of the welded specimens ranged from ~140 to ~250 MPa. Microstructural analysis revealed that decreased strength in the welded specimens was caused by volume flaws, microcracking of large ZrB_2 grains (up to 1 mm in length), and residual tensile stresses that developed at the surface of weld pools during cooling. The versatility of plasma arc welding was demonstrated by joining of ZrC based ceramics and fabricating three ZrB_2-ZrC components for potential applications, including a high temperature electrical contact, an ultra-high temperature thermocouple, and a wedge that

was a notional wing leading edge. These three applications demonstrated the ability to join ceramics to a refractory metal, fabricate a chemically inert high temperature thermocouple, and produce complex shapes for aerospace applications.

1. INTRODUCTION

Many non-oxide structural ceramics require densification by hot-pressing or spark plasma sintering, which produce relatively simple shapes.[1] Even when pressureless sintering can be utilized, green processing techniques may limit complex shape fabrication. Therefore, ceramic joining techniques, such as brazing and solid-state bonding are needed for manufacturing components with complex geometry.[1-7] Brazing is a highly versatile joining technique where a lower melting temperature material is utilized to bond ceramics that remain solid throughout the bonding process. Brazes for joining ceramics typically consist of glasses or metal alloys that wet the surfaces of the ceramics to be bonded.[4-6] While brazing is useful for applications such as fusion reactors, brazed joints are limited to lower use temperatures due to the presence of the glass or alloy phase at the joined interface.[2,4] For example, Pd braze alloys have been developed for UHTC (ultra-high temperature ceramic) applications; however, braze alloys have melting temperatures that are below the expected use temperatures for UHTCs (2000°C or higher).[1,8] Instead of brazing, for high temperature applications, solid-state bonding can be utilized. Unfortunately, solid-state bonding of UHTCs typically requires high temperatures and pressures, meaning that joints require the entire assembly to be joined to be heated to at least the densification temperature used for the powder compact.

Fusion welding of ceramics can be useful in applications where brazing or solid-state bonding are not appropriate. While fusion welding of ceramics has not received the same attention as fusion welding of metals, it has been demonstrated.[9-11] Specifically, arc welding offers the ability to fusion weld ceramics while being cost effective compared to methods such as laser or electron beam welding.[9] The purpose of this article is to compare the flexure strength of ZrB_2 containing 20 vol% ZrC (ZrB_2-20ZrC) with that of ZrB_2-20ZrC weldments fabricated by plasma arc welding (PAW) techniques, and demonstrate the versatility of PAW as a ceramic joining technique. The joining techniques utilized were based on work by King et al. on the PAW of ZrB_2-20ZrC.[12]

2. EXPERIMENTAL PROCEDURE

2.2 Material Processing

ZrB_2 ceramics with a nominal ZrC content of 20 vol% were prepared for joining. ZrB_2-ZrC powders were mechanically mixed by ball milling ZrB_2 (H.C. Starck; Grade B; Newton, MA) and ZrC (H.C. Starck; Grade B) with 0.625 wt.% phenolic resin (Georgia Pacific Chemicals; Atlanta, GA) to obtain a final carbon (C) content of 0.25 wt% (~0.7 vol%). Milling was carried out in acetone for 2 hours using tungsten carbide media. After milling, the powder slurry was dried using rotary evaporation to minimize segregation of the constituents. Dried powders were then ground and sieved to -60 mesh before hot-pressing.

Billets nominally 45 mm by 30 mm by 5 mm of ZrB_2-20ZrC were fabricated through hot-pressing. Hot-pressing was performed in a graphite element furnace (Thermal Technology; Model HP50-7010G; Santa Rosa, CA) using a graphite die. A heating rate of 50°C/min and a vacuum of ~30 Pa (200 millitorr) were used during heating. A one hour isothermal reaction hold at 1700°C under vacuum was performed to remove oxide contamination form the surface of the powders. After the reaction hold, the vacuum atmosphere was switched to flowing argon and a pressing pressure of 32 MPa was applied. A heating rate of 50°C/min was used to reach the final densification temperature of 2030°C. Pressing continued at temperature until recorded ram travel ceased for a period of 10 minutes. Pressed billets were removed from the graphite die and ground to a nominal thickness of 4 mm, using a manual surface grinder (Chevalier Machinery Inc.; Model FSG-618; Santa Fe Springs, CA) and a 120 grit diamond grinding wheel (National Diamond Labs; Los Angeles, CA). Surface ground billets were then cut using a diamond cutting wheel (National Diamond Labs) into smaller coupons for welding. The densities of each coupon were determined using the Archimedes method and the relative density was calculated based on a rule of mixtures theoretical density for ZrB_2-20ZrC (6.18 g/cm^3). ZrC ceramics containing 20 vol% TiC (Materion Advanced Chemicals; -325 mesh; Milwaukee, WI) were processed using the same methods outlined above.

2.3 UHTC Welding

All welding experiments were conducted in a custom welding apparatus described by King et al.[13] Joints requiring a gap between the coupons prior to welding were separated with 4 layers of double sided tape (3M; Scotch® Double Sided Tape; St. Paul, MN) resulting in a gap width of ~0.35 mm. Coupons were covered with a layer of graphite felt and pre-heated to a set temperature. At the pre-heat temperature, the samples were uncovered and the torch tip was placed at the edge of the coupons and aligned with the gap between the coupons to be joined. The arc was struck to the specimen and welding current was ramped at a rate of 20 A/s from an initial current of 25 A to the target welding current. Once the welding current was reached, the torch track was engaged at the desired weld speed. At the end of the weld, the current was reduced by 10% over 0.25 s followed by a ramp down to 25 A over ~12 s. Welded specimens were then covered with graphite felt and the furnace was allowed to equilibrate to the furnace set temperature. The furnace and welded specimens were then cooled at a rate of ~30°C/min from the equilibrated temperature to room temperature. Pulsed plasma arc welding (PPAW) was also utilized, and is characterized by pulsing of the current between peak and background presets. Coupons welded using PPAW were pulsed at the peak current for 0.1 s and a 50% background current for 0.2 s. Specimens joined using PAW and PPAW parameters were selected for mechanical behavior analysis. Both PAW and PPAW were utilized to fabricate a high temperature electrical connection between W wire and ZrB_2 or ZrB_2-20ZrC coupons. In addition, a UHTC thermocouple was fabricated by joining filaments of ZrB_2 and ZrB_2-20ZrC. A hollow wedge, meant to represent a UHTC wing leading edge segment for a hypothetical hypersonic vehicle, was also fabricated from ZrB_2-20ZrC using PPAW. Finally, PAW was used to butt-weld ZrC containing 20 vol% TiC to demonstrate the versatility of the technique. Table I summarizes parameters used for arc welding with peak/background currents listed for PPAW welds. All voltages were ~30 V.

2.3 Mechanical Properties and Microstructural Analysis

Mechanical properties of the ZrB_2-20ZrC parent material (PM) were analyzed. Parent material specimens were mounted in epoxy and polished to a mirror finish using successively finer diamond abrasives, with the finest abrasive being 0.25 μm. Vickers hardness was measured (Struers Inc.; Duramin 5; Cleveland OH) on polished surfaces using a load of 1 kg (9.8 N) for a dwell time of 10 s. Young's modulus (E) of the PM was measured by the impulse excitation technique (J.W. Lemmens Inc.; Grindosonic Mk5 Industrial; Heverlee, Belgium), described by ASTM C 1259.[14] Fracture toughness (K_{IC}) of the PM was measured by the Chevron notch method, described by ASTM C 1421, using modified configuration A bars.[15] The modified bars were shorter (~23 mm) than the standard (45 mm), therefore the strain rate was adjusted to remain within the range specified in the standard. Flexure strength (σ) of the PM was measured by testing configuration B bars in four-point bending, described by ASTM C1161, and analyzed with a Weibull distribution.[16] For comparison to the PM, ASTM C 1161 configuration A bars were tested in four-point bending for PAW, PPAW, and PAW/C-rich weldments, where the top surface of the weldment was placed in tension during testing. The weldment nomenclature of PAW and PAW/C-rich are based on those used for weldments-1 and 2 presented by King et al., while PPAW had not been previously investigated.[12] All flexure bars were cut from PM or welded billets using an automatic surface grinder (Chevalier Machinery Inc.; Model FSG-3A818) and a diamond cutting wheel. Cut bars were ground to size on an automatic surface grinder using a 600 grit diamond grinding wheel (National Diamond Labs). Microstructural analysis of ground or polished weldment cross-sections was performed using optical microscopy (Nikon; Epiphot 200; Tokyo, Japan) and scanning electron microscopy (Hitachi; S-570; Tokyo, Japan). Fracture surfaces were analyzed using scanning electron microscopy.

3. RESULTS AND DISCUSSION

3.1 Parent Material Mechanical Properties

Mechanical properties measured for the PM are summarized in Table II. Vickers hardness was 15.2±0.1 GPa, which falls within the range of hardness values reported by Tsuchida and Yamamoto (14.5 GPa, 23 vol% ZrC) for ZrB_2-ZrC ceramic composites.[17] Young's modulus of the PM was 512±2 GPa.[14] A volumetric rule of mixtures of reported Young's moduli for single crystal ZrB_2 (526 GPa) and single crystal ZrC (406 GPa) suggests that the Young's modulus of the PM should be 502 GPa.[18,19] When compared to the rule of mixtures calculation, the measured value is higher than expected. Assuming the value of 526 GPa is correct for the Young's modulus of ZrB_2 (the highest reported Young's modulus for ZrB_2), the Young's modulus of ZrC was estimated to be 456 GPa using a volumetric rule of mixtures and the measured Young's modulus of the composite. This value falls within the reported range for the Young's modulus of ZrC, which is 400 GPa to 470 GPa.[17,20] Therefore, the measured Young's modulus value is consistent with a fully dense ZrB_2-20ZrC ceramic. The values of both Vickers hardness and Young's modulus of the PM compare well with previously reported literature values.

The strength of the PM was 656±79 MPa, an average of 26 ASTM B-bars (4 mm by 3 mm by 45 mm) that were tested in four-point flexure. The strengths were further analyzed using a two parameter Weibull distribution.[16] Monolithic ZrB_2 has been reported to have four-point bend strengths up to ~570 MPa.[21] With an average strength of ~660 MPa, the PM ZrB_2-ZrC composite has a higher strength than monolithic ZrB_2, which has also been observed for similar particulate reinforced ceramic composites.[21-23] Similarly, the K_{IC} of the particulate composite is expected to be higher than the monolithic ceramic. The K_{IC} was 7.0±0.4 MPa·m$^{1/2}$ for the PM compared to values of 3.5-4.5 MPa·m$^{1/2}$ reported for monolithic ZrB_2.[8] This value agrees well with a K_{IC} of 7.4 MPa·m$^{1/2}$ for a ZrB_2-ZrC composite containing 39 vol% ZrC.[24] The measured K_{IC} was higher than the reported K_{IC} of Tsuchida and Yamamoto, 5.1 MPa·m$^{1/2}$, for ZrB_2-ZrC containing 23 vol% ZrC.[17] The Weibull distribution (Figure 1) was used to calculate a Weibull modulus of 9.5 for the PM. For commercial applications, a Weibull modulus of 10-12 is common, where a higher Weibull modulus indicates a narrower flaw size distribution, which allows for more predictable designs with ceramics.[25] The Weibull modulus of the PM is near that of commercial values for ceramics and the addition of ZrC led to an increase in strength and K_{IC} for the PM compared to monolithic ZrB_2.

3.2 Weldment Microstructure and Mechanical Behavior

Microstructural analysis of PAW welds has previously been performed by King et al., where PAW welds exhibited exaggerated/abnormal growth of ZrB_2 grains.[12] In the latter study, ZrB_2 grains up to ~1 mm long, but ~0.09 mm in the orthogonal direction, resulted in a grain size aspect ratio of ~11:1.[12] To limit the excessive grain length, and the amount of porosity associated with PAW welds, PPAW of ZrB_2-20ZrC was utilized for fusion welding in the present study.[12] Microstructural analysis of PPAW welds reveals that grain growth of ZrB_2 was affected by pulsing the weld current (Figure 2). Measurements of ZrB_2 grains in the PPAW fusion zone (FZ) indicated lengths up to 0.76 mm, with aspect ratios ranging from 13.5:1 to 43:1. The larger grain lengths and lower aspect ratio grains in PAW welds reveals that PPAW hindered the growth, in length and width, of ZrB_2 grains in the FZ. PPAW was used to weld ZrB_2-20ZrC and was observed to hinder the growth of ZrB_2 compared to PAW of ZrB_2-20ZrC.

For the present study, three weldments, PAW, PAW/C-rich, and PPAW, were tested in four-point flexure for comparison to the parent material. Flexure strength measurements were performed such that fracture occurred in the FZ of each weldment. Initially, fracture was observed in the heat affect zone (HAZ) of PAW/C-rich weldments, so an annealing procedure was utilized to reduce stresses. After annealing at 1500°C for 2 hours, fracture of PAW/C-rich flexure specimens occurred in the FZ. Fracture outside of the FZ did not occur in PAW or PPAW weldments, which were not annealed. The flexure strength of PAW weldments was 143±34 MPa, PPAW weldments were 166±22 MPa, and PAW/C-rich weldments were 247±21 MPa, which represent decreases in strength of 78% for PAW, 75% for PPAW, and 62% for PAW/C-rich compared to the PM. The lowest strength measured in the Weibull analysis of the PM was 509 MPa, and the highest strength for each weldment was 209 MPa for PAW, 205 MPa for PPAW, and 273 MPa for PAW/C-rich. This means that the highest PAW and PPAW weldment have strengths that are ~40% of the lowest PM strengths. In comparison, the strongest PAW/C-rich weldment had a strength that was ~53% of the lowest strength measured for a bar of the PM. The average weldment strengths are comparable to those reported by Rice, where arc welded ZrB_2 based ceramics exhibited strengths ranging from ~100 MPa to ~210 MPa with a maximum strength of ~410 MPa for monolithic ZrB_2.[9] ZrB_2-20ZrC weldments had lower measured strengths compared to the PM, with weldments exhibiting strengths comparable to previously reported strengths for ZrB_2 based fusion welds.[9]

While Rice produced ceramic fusion welds with strengths up to 415 MPa, data were reported as preliminary, with no further discussion of strength or microstructure.[9]

Therefore, the microstructures and fracture behavior of the weldments were evaluated in this study to determine the strength limiting features. Measured mechanical properties, fractography, and Griffith criterion calculations were utilized in the present study to determine critical flaw sizes of the PM and each weldment. The failure origin of PM specimens were scratch-like flaws that had depths similar to the estimated flaw size of 29 μm, calculated using the Griffith criterion.[25] Thus, the strength limiting flaws were likely surface damage from machining of the specimens. K_{IC} of the weldments was not measured, but due to the large grain sizes in PAW and PPAW, and the C-rich nature of PAW/C-rich welds, a value of K_{IC} of 2.3 MPa·m$^{1/2}$ (comparable to the lowest K_{IC} values reported for monolithic ZrB_2) was used for calculating weldment critical flaw sizes.[26] Fractographic analysis of PAW weld pools revealed that a likely source for failure was a circular penny crack in the volume of the specimen (Figure 3). The formation of the flaw likely occurred during cooling when ZrB_2-ZrC eutectic solidified and pulled away from primary ZrB_2 that had initially precipitated from the melt. Solidification of the eutectic results in volume contraction when going from a liquid to a solid. The observed flaw in Figure 3, a penny crack of ~280 μm in diameter, was smaller than the predicted size of 406 μm for the diameter of the penny shaped crack. While the measured flaw was smaller than predicted, similar flaws were observed in PAW weldment cross-sections (Figure 2 from King et al.), where penny shaped flaws up 660 μm in diameter were observed. Hence, volume flaws may be considered a source of failure initiation.[12] Multiple fracture mirrors were also observed on one ZrB_2 grain on a PPAW fracture surface (Figure 4). This indicates that spontaneous, or stress-induced, microcracking occurred in the ZrB_2 grains. Due to the anisotropic crystal structure of ZrB_2, residual stresses may result from differences in the coefficient of thermal expansion between the different crystallographic directions in the grains, which leads to cracking of grains.[18,27,28] Watts et al. previously estimated a band of grain sizes that may result in spontaneous microcracking of ZrB_2 as 980 to 2100 μm.[28] Lengths of ZrB_2 grains in FZs of PAW specimens fall into this range, suggesting that spontaneous microcracking of ZrB_2 grains could occur in the FZs of ZrB_2-ZrC joined by PAW. These microcracks may also link up, which would lead to the formation of volume flaws large enough to initiate failure. Therefore, initiation of failure in the FZs of ZrB_2-ZrC joined by PAW can occur from two different volume flaws (voids produced by liquid/crystal separation and the link up of microcracks).

In contrast, the lengths of ZrB_2 grains in PPAW welds are less than the range predicted for spontaneous microcracking. Hence, the fracture mirrors observed in Figure 4 are likely a result of stress-induced microcracking in the PPAW FZ, where link up of microcracks could result in a large enough volume flaw (calculated to be ~300 μm) to initiate failure. A volume critical flaw for PAW/C-rich was calculated to be ~140 μm (diameter) while a surface penny crack was calculated to be ~60 μm (radius), and a scratch-like flaw was calculated to be ~20 μm (depth). Machining with a 600 grit diamond wheel should leave scratches ~15 μm deep, while ZrB_2 grains within the PAW/C-rich FZ are also large enough to initiate failure, volume or surface, and a specific critical flaws could not be defined for PAW/C-rich weldments. However, as with volume contraction in the solidifying eutectic in PAW FZs, tensile residual stresses may develop at the surface of PAW/C-rich weldments, which could also affect the weldment strength. The effects of these stresses appear to act on cracks radiating from a 30 kg (294 N) indent, placed near the surface of a PAW/C-rich FZ, as the cracks deflected towards the surface of the FZ (Figure 5). As the surface of the FZs were placed in tension during flexure testing, tensile residual stresses may have led to weaker weldments by lowering the stress needed for crack initiation. Internal flaws (eutectic separation and microcracking) and tensile residual stresses at the surface of weldments lead to failure initiation of arc welded ZrB_2-ZrC weldments.

3.3 Carbide Fusion Welding

While the present study and several previous reports on arc welding of ceramics have focused on diboride based ceramics, joining by arc welding is not limited to diboride ceramics.[9,12,13] PAW of ZrC containing 20 vol% TiC (ZrC-20TiC) was accomplished using the parameters listed in Table II. A cross-section of the ZrC-20TiC weld (Figure 6) revealed that at the center of the weld, the FZ was 2.3 mm thick, but contacted the HAZ throughout the thickness of the coupon (4 mm). Porosity was observed at the edge of the FZ, where oblong pores were up to 0.9 mm in size along their longest axis. Porosity and grain pullout were also observed in the HAZ. Areal analysis revealed that C content increased from 0.4 area% in the PM to 1.7 area% in the HAZ, leading to increased grain pullout in the HAZ. X-ray diffraction detected the presence of TiO (hongquiite) in the PM, but not the FZ, suggesting that pores in the FZ and HAZ are possibly formed during active oxidation of the carbide. Removal of oxygen impurities from the ceramic during processing may result in improved weldments. Based on these results, PAW appears to be a viable method for joining carbide ceramics.

3.4 UHTC Welding Applications

Fusion welding of UHTCs could prove to be a versatile technique for fabricating components with complex shapes. The first example application demonstrated was a high temperature electrical contact. For the contact, a W wire (0.8 mm diameter) was spot welded to a ZrB_2 coupon (28.0 mm by 9.0 mm by 3.6 mm) using the parameters listed in Table II. A representative image of a weld pool is presented in Figure 7. The W wire was curved into a “P” shape prior to joining to cover more of the surface of the 9 mm by 3 mm ZrB_2 coupon, which is outlined in Figure 7. The weld pool area was 23.7 mm^2, which was ~73% of the coupon area. Partial melting of the W wire occurred. Excess W wire was observed at the far left, and the bottom, of the weld due to shifting of the “P” during melting/welding. Porosity, Figure 7, was also observed at the surface of the weld. Below the FZ of the weld, cracking was observed in the ZrB_2 coupon. To reduce cracking, W wire was welded to ZrB_2-20ZrC coupons, which have a lower melting temperature (2830°C), lower elastic modulus (512 GPa), and higher strength (656 MPa) than monolithic ZrB_2 (T_m=3245°C, E=526 GPa, σ=570 MPa).[8,18,29] A lower melting temperature and elastic modulus reduce thermal residual stresses that may develop during cooling ($\sigma=\Delta\alpha\cdot\Delta T\cdot E$), while higher strength increases resistance to crack initiation.[30] Welds made on ZrB_2-20ZrC coupons covered >95% of the end of the coupon and exhibited porosity at the surface of the weld; however, cracking of the PM was not observed for ZrB_2-20ZrC coupons. Based on these preliminary studies, spot welding appears to be a viable technique for joining refractory metals to boride ceramics.

Cross-sections of spot welded W contacts on ZrB_2-20ZrC coupons were analyzed using secondary and backscattered electron microscopy techniques. A backscattered electron image (BEI) of the contact interface (Figure 8) revealed a distinct division between the FZ and the PM. Dissolution of the parent material by the melt pool was observed, where grains at the FZ/PM interface appear to have been attacked by the melt pool (FZ surrounds grains of the PM). Diffusion of W from the melt pool into the PM was also observed, appearing as a brighter grain boundary phase. The presence of W in the grain boundary phase was confirmed using energy dispersive spectroscopy (EDS), and the depth of W diffusion was measured to be ~90 μm. Core-shell structures were also observed in ZrC grains within the W diffusion layer. Figure 9 reveals the presence of core-shell ZrC grains and the grain boundary W phase where ZrB_2 appears dark grey, ZrC appears light grey, and W appears white. The core-shell structure occurs as W forms a solid solution with ZrC, indicating the brighter shell to be (Zr,W)C which would appear brighter in a BEI image, compared to ZrC.[31,32] A distinct FZ and PM were observed, as was the diffusion of W into the PM (90 μm depth), in a successful ZrB_2-20ZrC to W weld.

Fusion welding was also used to fabricate an extreme environment UHTC thermocouple. Two thermocouple leads, one ZrB_2 and the other ZrB_2-20ZrC, were fabricated by extruding a thermoplastic polymer (ethylene ethyl acrylate) loaded with ceramic powder based on parameters discussed in previous studies.[33] For the present study, green filaments with a diameter of 2.4 mm were produced. After binder burnout to remove the polymer from the filaments, sintering was carried out at 2150°C for 2 hours. Sintered ZrB_2 filaments had a diameter of ~2.08 mm and ZrB_2-20ZrC filaments had a diameter of ~2.05 mm. Measurements by the Archimedes method revealed a relative density of ~60% for both the ZrB_2 and ZrB_2-20ZrC filaments. After sintering, the tips of a ZrB_2 and a ZrB_2-20ZrC filament were joined using the parameters listed in Table II. The resulting thermocouple (Figure 10) was 54 mm in length, while the length of the fusion zone was ~3.5 mm. The voltage difference between the ZrB_2 and ZrB_2-20ZrC leads was measured as a function of temperature. Independent temperature measurements were made using a type B thermocouple. The thermocouple did not exhibit a voltage response below ~500°C; however, repeatable voltage differences were measured at higher temperatures. For example, the voltage difference was 0.12 mV at 750°C, 0.23 mV at 1000°C, and 0.46 mV at 1250°C. Voltage differences at higher temperatures were obscured by heating of the connections between the thermocouple and the multimeter due to the high thermal conductivity of the leads. Hence, PAW appears to be a viable technique for fabricating UHTC thermocouples.

The fabrication of a ZrB_2-20ZrC wedge, which was a mock-up of a wing leading edge for a hypersonic aerospace vehicle, was completed using PPAW. One face on each of two ZrB_2-20ZrC billets (nominally 45 mm by 30 mm by 4 mm) was ground at a 10° angle to produce a wedge with a 20° angle. The billets were then welded using PPAW using the parameters summarized in Table II. During welding, melt back of the billets occurred and excess melt flowed to the side of the leading edge. Excess material was removed using wire electric discharge machining (EDM). The leading edge was cut in half to examine the FZ for porosity and penetration depth of the weld, and to measure the amount of melt back from the tip. Porosity was apparent at the base of the weld pool; however, the FZ appeared to be dense, Figure 11. The penetration depth of the FZ was ~2.8 mm. The melt back of the billets after welding was ~4.5 mm. The hollow center of the wedge allows for the potential to cool the leading edge with a gas, liquid, or a higher conductivity solid.[34,35] The hollow center also decreases the mass of the leading edge compared to solid wedges. The welded wedge presented in Figure 11 has ~16 area%

void space, giving the hollow wedge a 16% reduction in mass compared to a solid wedge. PPAW was utilized to fabricate a hollow ZrB_2-20ZrC leading edge, demonstrating the ability to fabricate complex ceramic shapes by fusion welding.

4. CONCLUSIONS

Plasma arc welding was used to join ZrB_2-20ZrC and ZrC-20TiC ceramics. The fusion welding of both diboride and carbide ceramics demonstrates versatility in PAW as a ceramic joining technique. Different PAW techniques were also utilized in the fabrication of ZrB_2-20ZrC butt welds that were analyzed for flexure strength. The failure of the weldments was attributed to the formation of large volume flaws. Future work to minimize the formation of flaws should lead to improved mechanical properties. Along with the fusion welding of ZrC-20TiC, three applications were presented which can benefit from the fusion welding of ceramics. Conclusions of this study include:

1. The hardness (15.2 GPa), Young's modulus (512 GPa), fracture toughness (7.0 $MPa\cdot m^{1/2}$), flexure strength (656 MPa), and Weibull modulus (9.5) of ZrB_2-20ZrC, utilized as a parent material (PM) for welding studies, were analyzed. The mechanical properties of the PM agreed well with previously reported values.
2. PPAW was utilized to weld ZrB_2-20ZrC ceramics. The grain lengths of ZrB_2 were reduced to <0.8 mm in comparison to PAW FZ's (1 mm). ZrB_2 grain aspect ratios were increased to a range of 25:1 to 43:1 for PPAW when compared to PAW (11:1) as a welding technique, indicating not only a reduction in grain length, but also grain width in PPAW FZs.

3. Flexure strengths for PAW (143 MPa), PPAW (166 MPa), and PAW/C-rich (247 MPa) were less than the PM (656 MPa), where internal flaws and tensile residual stresses affected the strength of weldments.
4. PAW was used to weld a carbide ceramic, ZrC-20TiC. Porosity was observed in the FZ and HAZ, possibly formed as a result of active oxidation of the carbide, and removal of oxygen impurities in the PM should result in improved weldments.
5. PAW was utilized to fusion weld two ceramics (ZrB_2 and ZrB_2-20ZrC) to a refractory metal (W). Attack of the PM by the melt pool was apparent, and the composition of the FZ contained the two constituents of the PM. W diffusion into the PM was observed to be 90 μm in depth.
6. A UHTC thermocouple was fabricated using PAW to weld ZrB_2 and ZrB_2-20ZrC filaments together. A systematic voltage response from the thermocouple was observed above 750°C.
7. Complex shape fabrication was demonstrated as PPAW was utilized in the fabrication of a hollow ZrB_2-20ZrC wedge. The FZ was 2.8 mm in depth, where melt back of the PM was 4.5 mm and porosity was observed at the base of the FZ. The hollow leading edge offers weight savings, and the ability to cool the inside of the leading edge with a gas, liquid, or high thermal conductivity solid.

ACKNOWLEDGEMENTS

Research was conducted in cooperation with MO-SCI Corporation and supported by AFOSR Grant # FA9550-12-C-0060. The authors would also like to acknowledge

Andrew Schlup and Cari Swanson for their assistance with materials processing. The authors would also like to thank the Advanced Materials Characterization Laboratory (AMCL) at Missouri S&T for use of their equipment.

REFERENCES

[1]W. R. Pinc, M. Di Prima, L. S. Walker, Z. N. Wing, and E. L. Corral, "Spark Plasma Joining of ZrB_2–SiC Composites Using Zirconium–Boron Reactive Filler Layers," *J. Am. Ceram. Soc.*, **94**[11] 3825-32 (2011).

[2]M. Singh and R. Asthana, "Joining and integration of ZrB_2-based ultra-high temperature ceramic composites using advanced brazing technology," *J. Mater. Sci.*, **45**[16] 4308-20 (2010).

[3]M. L. Shalz, B. J. Dalgleish, A. P. Tomsia, and A. M. Glaeser, "Ceramic joining," *J. Mater. Sci.*, **28**[6] 1673-84 (1993).

[4]P. Colombo, B. Riccardi, A. Donato, and G. Scarinci, "Joining of SiC/SiCf ceramic matrix composites for fusion reactor blanket applications," *J. Nucl. Mater.*, **278**[2–3] 127-35 (2000).

[5]M. L. Shalz, B. J. Dalgleish, A. P. Tomsia, R. M. Cannon, and A. M. Glaeser, "Ceramic joining III bonding of alumina via Cu/Nb/Cu interlayers," *J. Mater. Sci.*, **29**[14] 3678-90 (1994).

[6]J. Chen, P. Wei, Q. Mei, and Y. Huang, "The wettability of Y–Al–Si–O–N oxynitride glasses and its application in silicon nitride joining," *J. Eur. Ceram. Soc.*, **20**[14–15] 2685-89 (2000).

[7]M. Singh, "Joining of sintered silicon carbide ceramics for high-temperature applications," *J. Mater. Sci. Lett.*, **17**[6] 459-61 (1998).

[8]W. G. Fahrenholtz, G. E. Hilmas, I. G. Talmy, and J. A. Zaykoski, "Refractory Diborides of Zirconium and Hafnium," *J. Am. Ceram. Soc.*, **90**[5] 1347-64 (2007).

[9]R. W. Rice, "Joining of Ceramics," pp. 69-111 in Advances in joining technology: proceeding of the 4th Army Materials Technology Conference, Boston, MA, 1976.

[10]G. N. Mikhailova, B. P. Mikhailov, and A. V. Troitskii, "Laser welding of HTSC ceramics," *Laser Physics Letters*, **1**[10] 525-27 (2004).

[11]V. A. Burdovitsin, A. S. Klimov, A. V. Medovnik, and E. M. Oks, "Electron beam treatment of non-conducting materials by a fore-pump-pressure plasma-cathode electron beam source," *Plasma Sources Science and Technology*, **19**[5] 055003 (2010).

[12]D. S. King, G. E. Hilmas, and W. G. Fahrenholtz, "Plasma arc welding of ZrB_2-20 vol% ZrC ceramics," *J. Eur. Ceram. Soc.*, **34**[15] 3549-57 (2014).

[13]D. S. King, G. E. Hilmas, and W. G. Fahrenholtz, "Plasma Arc Welding of TiB_2-20 vol.% TiC," *J. Am. Ceram. Soc.*, **97**[1] 56-59 (2014).

[14]ASTM (ASTM International), "Dynamic Young's Modulus, Shear Modulus, and Poisson's Ratio for Advanced Ceramics by Impulse Excitation of Vibration", ASTM Standard C1259-08E1, West Conshohocken, PA., (2008).

[15]ASTM (ASTM International), "Standard Test Methods for Determination of Fracture Toughness of Advanced Ceramics at Ambient Temperature", ASTM Standard C1421-10, West Conshohocken, PA., (2010).

[16]ASTM International (ASTM), "Standard Test Method for Flexural Strength of Advanced Ceramics at Ambient Temperature", ASTM Standard C1161-02c, West Conshohocken, PA., (2008).

[17]T. Tsuchida and S. Yamamoto, "Spark plasma sintering of ZrB_2–ZrC powder mixtures synthesized by MA-SHS in air," *J. Mater. Sci.*, **42**[3] 772-78 (2007).

[18]N. L. Okamoto, M. Kusakari, K. Tanaka, H. Inui, and S. Otani, "Anisotropic elastic constants and thermal expansivities in monocrystal CrB_2, TiB_2, and ZrB_2," *Acta Mater.*, **58**[1] 76-84 (2010).

[19]R. Chang and L. J. Graham, "Low Temperature Elastic Properties of ZrC and TiC," *J. Appl. Phys.*, **37**[10] 3778-83 (1966).

[20]L. Silvestroni and D. Sciti, "Oxidation of ZrB_2 Ceramics Containing SiC as Particles, Whiskers, or Short Fibers," *J. Am. Ceram. Soc.*, **94**[9] 2796-99 (2011).

[21]A. L. Chamberlain, W. G. Fahrenholtz, G. E. Hilmas, and D. T. Ellerby, "High-Strength Zirconium Diboride-Based Ceramics," *J. Am. Ceram. Soc.*, **87**[6] 1170-72 (2004).

[22]E. W. Neuman, G. E. Hilmas, and W. G. Fahrenholtz, "Strength of Zirconium Diboride to 2300°C," *J. Am. Ceram. Soc.*, **96**[1] 47-50 (2013).

[23]E. Kang and C. Kim, "Improvements in mechanical properties of TiB_2 by the dispersion of B_4C particles," *J. Mater. Sci.*, **25**[1] 580-84 (1990).

[24]S. H. Shim, K. Niihara, K. H. Auh, and K. B. Shim, "Crystallographic orientation of ZrB_2-ZrC composites manufactured by the spark plasma sintering method," *Journal of Microscopy*, **205**[3] 238-44 (2002).

[25]J. B. Wachtman, W. R. Cannon, and M. J. Matthewson, "Mechanical Properties of Ceramics," 2nd ed. John Wiley & Sons, Inc.: Hoboken, NJ, (2009).

[26]J. J. Meléndez-Martínez, A. Domínguez-Rodríguez, F. Monteverde, C. Melandri, and G. de Portu, "Characterisation and high temperature mechanical properties of zirconium boride-based materials," *J. Eur. Ceram. Soc.,* **22**[14–15] 2543-49 (2002).

[27]J. J. Cleveland and R. C. Bradt, "Grain Size/Microcracking Relations for Pseudobrookite Oxides," *J. Am. Ceram. Soc.,* **61**[11-12] 478-81 (1978).

[28]J. Watts, G. Hilmas, and W. G. Fahrenholtz, "Mechanical Characterization of ZrB_2–SiC Composites with Varying SiC Particle Sizes," *J. Am. Ceram. Soc.,* **94**[12] 4410-18 (2011).

[29]E. Rudy and S. Windish, "Ternary Phase Equilibria in Transition Metal-Boron-Carbon-Silicon System: Part V. Compendium of Phase Diagram Data." in**.** Air Force Materials Laboratory, AFML-TR-65-2, Wright Patterson Air Force Base, OH, 1966.

[30]K. K. Chawla, "Composite Materials: Science and Engineering," Second ed. Springer: New York, NY, (1998).

[31]V. N. Eremenko, T. Y. Velikanova, L. V. Artyukh, G. M. Akselrod, and A. S. Vishnevskii, "Study of the Ternary W-HfC-C and W-ZrC-C Systems at Temperatures Below the Solidus," *Dop. Akad. Nauk Ukr. RSR*[1] 80 (1976).

[32]G. S. Upadhyaya, "Materials science of cemented carbides — an overview," *Materials & Design,* **22**[6] 483-89 (2001).

[33]G. E. Hilmas, D. R. Beeaff, A. C. Mulligan, M. M. Opeka, M. J. Rigali, and M. P. Sutaria, "Forming feed rod comprising a thermoplastic polymer and ceramic or metallic particulate material; forming hole in rod; inserting start of continuous spool of ceramic fiber, metal fiber, or carbon fiber; extruding to form continuous filament," U.S. Patent 6,355,338, (2002).

[34]G. T. Colwell and J. M. Modlin, "Heat pipe and surface mass transfer cooling of hypersonic vehicle structures," *J. Thermophys. Heat Transfer,* **6**[3] 492-99 (1992).

[35]J. M. Modlin and G. T. Colwell, "Surface cooling of scramjet engine inlets using heat pipe, transpiration, and film cooling," *J. Thermophys. Heat Transfer,* **6**[3] 500-04 (1992).

Table I: Weldment designations and welding parameters for ZrB_2 based ceramics

Weldment	**Coupon dimensions (mm)**	**Gap**	**Current (A)**	**Plasma flow rate (l/min)**	**Welding speed (cm/min)**	**Pre-heat temperature (°C)**
PAW	45x15x4	Yes	198	0.75	8	1450
PAW/C-rich	45x15x4	Yes	198	0.75	8	1450
PPAW	45x15x4	Yes	260/130	1	12	1450
E-contact	28x9x3	No	60	1	Spot weld	1650
Thermocouple	N/A	No	60	1	Spot weld	1650
Leading edge	45x30x4	Yes	260/130	1	12	1450
ZrC-20TiC	30x11x4	Yes	198	1	8	1450

Table II: Mechanical Properties of ZrB_2-20ZrC

Mechanical Property	**Value**
Hardness (GPa)	15.2±0.1
Young's modulus (GPa)	512±2
Flexure strength, average (MPa)	656±79
Weibull modulus	9.5
Fracture toughness ($MPa \cdot m^{1/2}$)	7.0±0.4

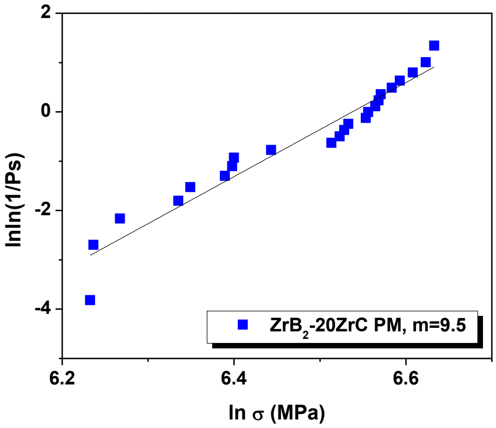

Figure 1: Two parameter Weibull distribution of the PM strengths. The Weibull modulus was calculated to be 9.5.

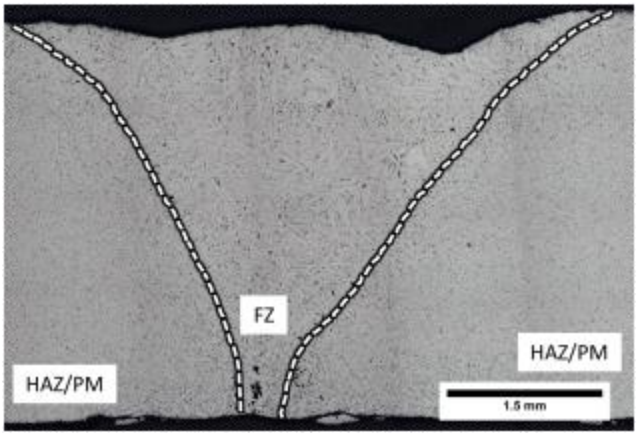

Figure 2: Optical micrograph cross-section of ZrB_2-20ZrC PPAW FZ exhibiting a reduction in ZrB_2 grain size and FZ porosity compared to ZrB_2-20ZrC PAW welds. The fusion zone (FZ) and heat affected zone/parent material (HAZ/PM) are identified.

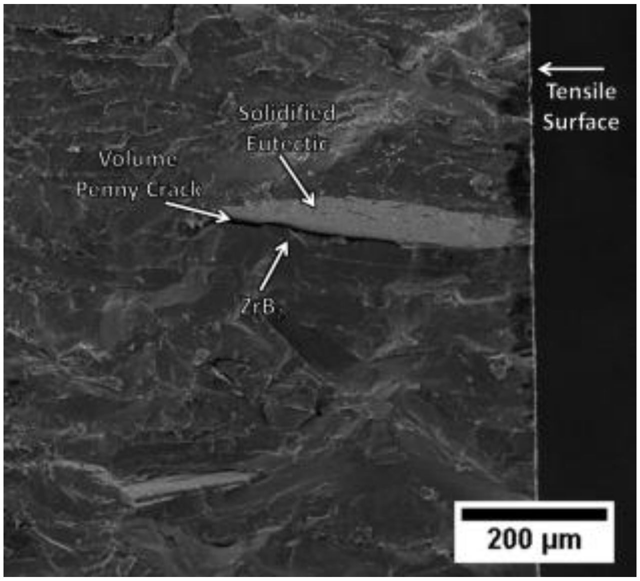

Figure 3: Secondary electron image of PAW fracture surface where during cooling of the weld, eutectic pulled away from a ZrB_2 grain, leaving a penny shaped crack.

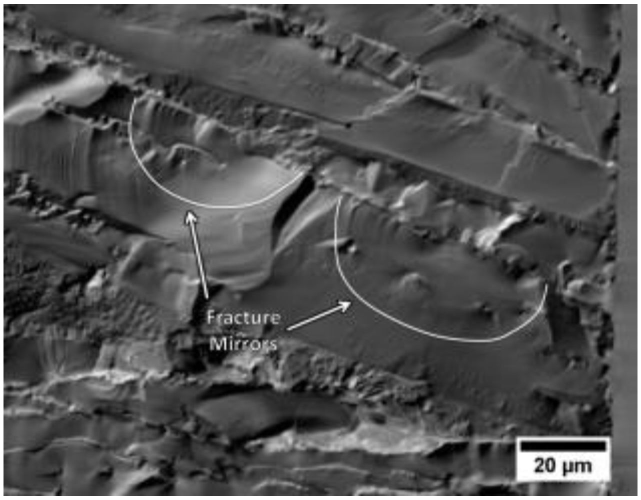

Figure 4: Multiple fracture mirrors were observed in one ZrB_2 gain in a PPAW weld.

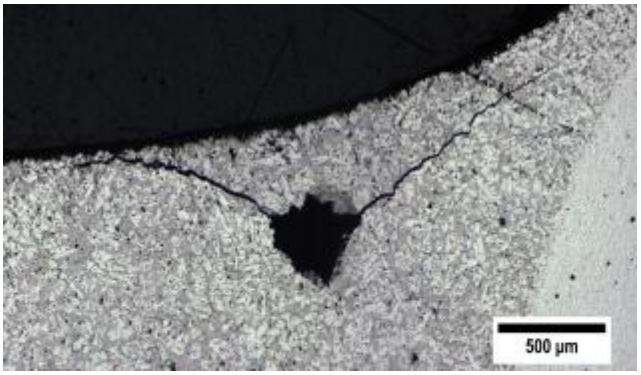

Figure 5: Cracking outlet from the corners of a 30 kg (294 N) Vickers indent in PAW/C-rich weldment. Cracks deflect toward the surface of the weldment.

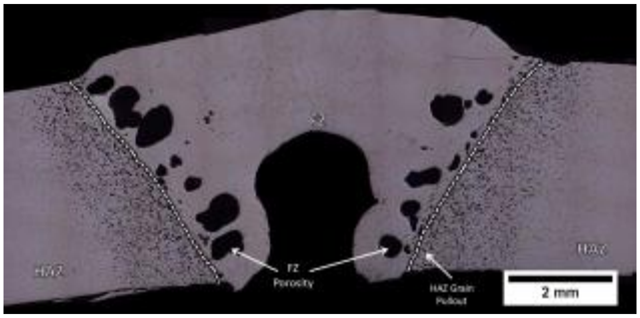

Figure 6: Optical micrograph cross-section of ZrC-20TiC joined using PAW. Porosity was observed at the edge of the FZ and HAZ, along with grain pullout in the HAZ.

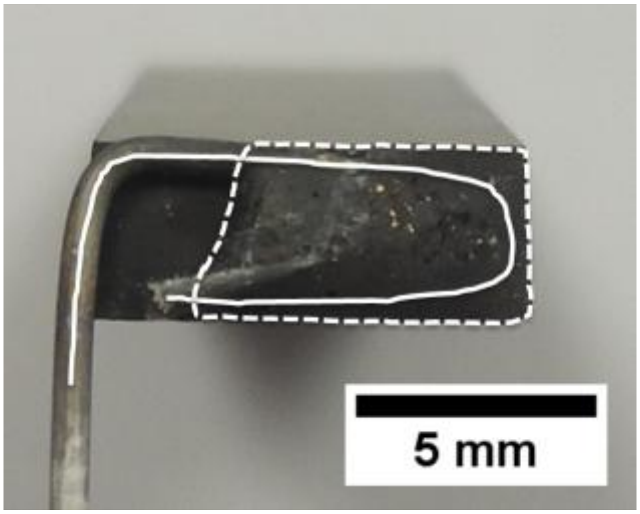

Figure 7: Final spot weld of W wire onto a ZrB_2 coupon. A dashed line outlines the FZ and a solid line outlines the shape of the W wire prior to welding where a shift of the W wire at the bottom of the ZrB_2 coupon was observed.

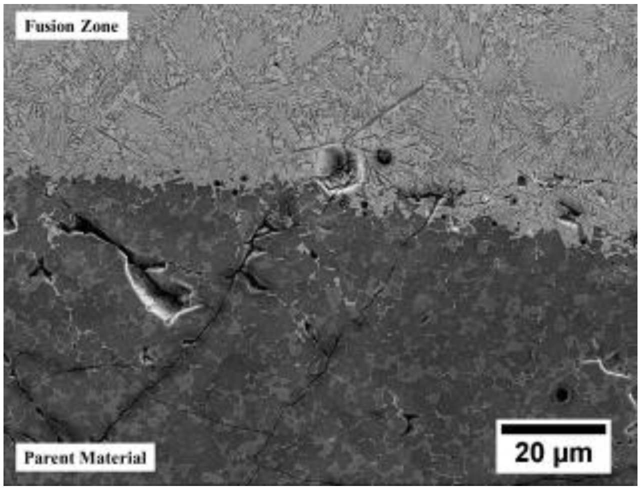

Figure 8: SEM image of the interface between a spot weld of W wire onto a ZrB_2 coupon. A distinct interface exists between the FZ and the PM. Attack of the PM by the weld pool is exhibited by grain pullout of the PM.

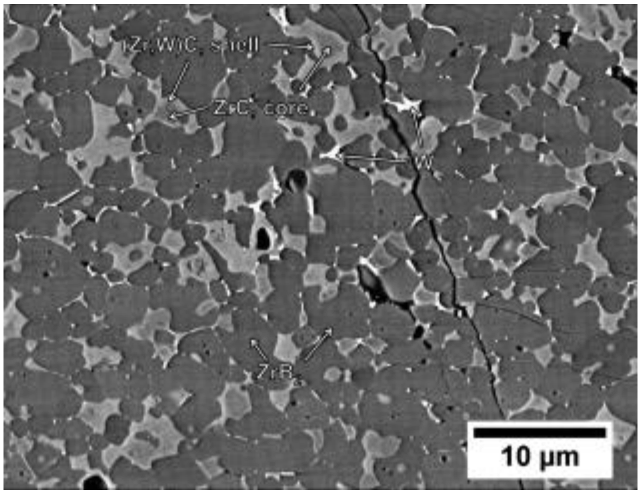

Figure 9: BEI image of ZrB_2-20ZrC where a core-shell structure was observed in the ZrC grains (light grey) of PM as W (white) diffused into the PM. The core-shell occurs as W forms a ZrC-WC solid solution. ZrB_2 appears dark grey.

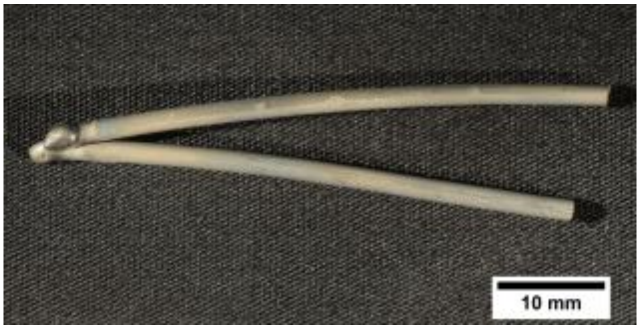

Figure 10: UHTC thermocouple fabricated from ZrB_2 and ZrB_2-20ZrC filaments.

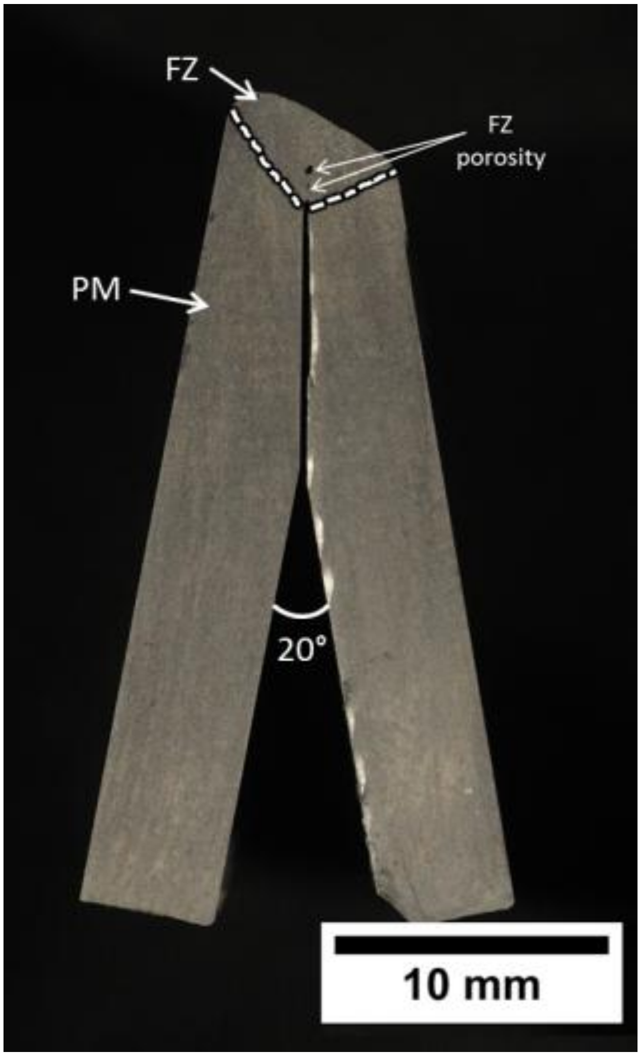

Figure 11: Hollow ZrB_2-20ZrC leading edge. Porosity is observed near the base of the FZ.

III. GROWTH OF ZrB_2 IN PLASMA ARC WELDED ZrB_2-20 VOL% ZrC

Derek S. King, Greg E. Hilmas, William G. Fahrenholtz
Missouri University of Science and Technology
Materials Science and Engineering Dept.
Rolla, MO 65409
Corresponding Author Contact
Email: dsk2nf@mst.edu
Phone: 1-573-341-7205
Fax: 1-573-341-6934

ABSTRACT

The growth and texture of ZrB_2 grains were analyzed for three plasma arc welded ZrB_2-20 vol% ZrC ceramics. The arc to workpiece power transfer efficiency was estimated for each weldment, and determined to be <20% for keyhole welds, and <15% for non-keyhole welds. Weld pool temperatures, and growth rates of ZrB_2 were expected to be highest in the non-keyhole weld, resulting in a textured fusion zone. Texture was not observed in the keyhole fusion zones. From the surface of the non-keyhole fusion zone, it was observed that ZrB_2 grew preferentially along the basal plane, resulting in grains with a plate-like structure. Analysis of a ZrB_2 free surface revealed that grains grew by ledge growth mechanism. Equilibrium and non-equilibrium solidification of ZrB_2 and ZrC was observed in each weldment. Non-equilibrium solidification of the fusion zone occurred when desaturation of B in the weld pool liquid forced the precipitation of ZrC inside of ZrB_2 grains.

1. INTRODUCTION

Ultra high temperature ceramics (UHTCs) are a family of ceramics that have high melting temperatures (>3000°C), and consists of several carbides, nitrides, and diborides.[1-3] Because of their high melting temperature, UHTCs are leading candidate materials for hypersonic flight applications, such as atmospheric re-entry vehicles, where application temperatures are expected to be greater than 2000°C.[1,3-7] One UHTC that has received much attention is ZrB_2, where ZrB_2 is of interest for applications such as molten metal crucibles, high temperature electrodes, and high temperature engine components.[5-12] However, like many non-oxide advanced ceramics, ZrB_2 has a very strong covalent bonding nature, and a low self-diffusion coefficient.[5,9,13] This leads to processes like hot-pressing and spark plasma sintering (SPS) being the preferred methods for densification, and limiting production to relatively simple shapes.[7,11,14]

Due to the limited shape formation of hot-pressing and SPS, joining has become important for the integration of ZrB_2 into hypersonic flight systems. To join ZrB_2-SiC ceramics, Sing et al. used palladium based brazes e.g., Palco® and Palni®, as a joint material.[15,16] However, the melting temperature of the brazes, ~1780°C, is lower than the expected use temperature of ≥2000°C for UHTCs.[15] The use of glass brazes for joining ZrB_2 has also been reported, but the melting temperature of the brazes would still be an issue (1200-1400°C).[17] This was demonstrated by Esposito and Bellosi, who joined ZrB_2-SiC (20 wt% SiC) with a SiO_2-Al_2O_3-CaO glass, and measured the three point flexure strength of the joint to be ~280 MPa at room temperature. The strength of the parent material (PM) at room temperature was ~700 MPa. At 1000°C, the strength of the joint dropped to ~90 MPa, and the PM strength dropped to ~400 MPa.[17] To eliminate braze melting temperature issues, solid-state joining techniques are attractive, and have been used to join ceramics like ZrB_2, SiC, AlN, and graphite.[18-21] The joining of ZrB_2-SiC (30 vol% SiC) UHTCs, by SPS, was demonstrated by Pinc et al., where joints exhibited shear strengths of 311 MPa at RT and 284 MPa at 1350°C, similar to the shear strength of the PM, 345 MPa at RT and 266 MPa at 1350°C.[14] Statistically, Pinc et al. demonstrated no difference between the joint and PM, but as SPS was the joining method, shape limitation could still be considered an issue.[14]

Brazing and solid-state joining techniques both have their advantages and disadvantages, and when compared to metals joining techniques, it is evident that the extent of ceramic joining techniques is limited. However, more recently, research on the fusion joining of ceramics has started to broaden the spectrum of ceramic joining techniques.[22-28] Burdovitsin et al. used electron-beam welding to fusion weld fused alumina (Alundum®), quartz, and glass. Tensile strengths of the fused alumina were 15-30 MPa for the joint and 40-50 MPa for the PM. While Burdovitsin et al. investigated the fusion welding of non-conducting materials, Hilmas et al. expanded on work set forth by Rice, fusion welding ZrB_2-SiC and ZrB_2-SiC-B_4C materials with an arc welding technique similar to gas tungsten arc welding (GTAW).[24,29] Recently, King et al. has demonstrated that plasma arc welding (PAW) can be used to fusion weld TiB_2-TiC and ZrB_2-ZrC ceramics (20 vol% carbide).[22,23] The microstructure of a TiB_2-TiC fusion zone was related to the relative temperatures of the weld, where grains at the surface and bottom of the weld pool grew to lengths of ~200 μm, and grains in the middle of the weld pool grew to lengths >1 mm. The larger grains in the center of the weld pool indicated higher growth rates and temperatures, while the surface cooled more quickly, leading to a higher growth rate and lower melt temperatures.[23] Further analysis by King et al. on both TiB_2-TiC and ZrB_2-ZrC welds revealed that the eutectic compositions agreed well with previously reported eutectic compositions, indicating that the weld pool solidified along an equilibrium cooling path.[2,22,23,30]

Recent progress in PAW of diboride-carbide ceramics has revealed the potential of arc welding as a fusion joining technique for ceramics. Still, the understanding of ceramic weld pool solidification is quite limited. The purpose of this article is to estimate the weld pool temperatures of three ZrB_2-20ZrC weldments, based on the welding power for each weld, and utilize microstructural information to gain understanding on the solidification of UHTC weld pools. The joining techniques utilized were based on work by King et al. on the PAW of ZrB_2-20ZrC.[22]

2. EXPERIMENTAL PROCEDURE

ZrB_2 ceramics with a nominal ZrC content of 20 vol% were prepared for joining. ZrB_2-ZrC powders were mechanically mixed by ball milling ZrB_2 (H.C. Starck; Grade B; Newton, MA) and ZrC (H.C. Starck; Grade B) with 0.625 wt.% phenolic resin (Georgia Pacific Chemicals; Atlanta, GA) to obtain a final carbon (C) content of 0.25 wt% (~0.7 vol%). Milling was carried out in acetone for 2 hours using tungsten carbide media. After milling, the powder slurry was dried using rotary evaporation to minimize segregation of the constituents. Dried powders were then ground and sieved to -60 mesh before hot-pressing.

Billets nominally 45 mm by 30 mm by 5 mm of ZrB_2-20ZrC were densified through hot-pressing. Hot-pressing was performed in a graphite element furnace (Thermal Technology; Model HP20-3060; Santa Rosa, CA) using a graphite die. A heating rate of 50°C/min and a vacuum of ~30 Pa (200 millitorr) were used during heating. A one hour isothermal reaction hold at 1650°C under vacuum was performed to remove oxide contamination from the surface of the powders. After the reaction hold, the vacuum atmosphere was switched to flowing argon and a pressing pressure of 32 MPa was applied. A heating rate of 50°C/min was used to reach the final densification temperature of 1980°C. Pressing continued at the densification temperature until recorded ram travel ceased for a period of 10 minutes. Pressed billets were removed from the graphite die and ground to a nominal thickness of 4 mm, using a manual surface grinder (Chevalier Machinery Inc.; Model FSG-618; Santa Fe Springs, CA) and a 120 grit diamond grinding wheel (National Diamond Labs; Los Angeles, CA). Surface ground billets were then cut using a diamond cutting wheel (National Diamond Labs) into smaller coupons for welding, nominally 30 mm by 11 mm by 4 mm. The densities of each coupon were determined using the Archimedes method and the relative density was calculated based on a rule of mixtures theoretical density for ZrB_2-20ZrC (6.18 g/cm^3).

All welding experiments were conducted in a custom welding apparatus described by King et al.[23] Joints requiring a gap between the coupons prior to welding were separated with 2 layers of double sided tape (3M; Scotch® Double Sided Tape; St. Paul, MN) resulting in a gap width of ~0.18 mm. Coupons were covered with a layer of graphite felt insulation and pre-heated to a set temperature. At the pre-heat temperature, the samples were uncovered and the torch tip was placed at the edge of the coupons and aligned with the gap between the coupons to be joined. The arc was struck to the specimen and welding current was ramped at a rate of 20 A/s from an initial current of 25

A to the target welding current. Once the welding current was reached, the torch track was engaged at the desired weld speed. At the end of the weld, the current was reduced by 10% over 0.25 s followed by a ramp down to 25 A over ~12 s. Welded specimens were then covered with graphite felt and the furnace was allowed to equilibrate to the furnace set temperature. The furnace and welded specimens were then cooled at a rate of ~30°C/min from the equilibrated temperature to room temperature. All voltages were ~28 V.

Three sets of PAW parameters were used to fusion weld ZrB_2-20ZrC. Parameters included a high (222 A), medium (198 A), and low (176 A) current with corresponding low (0.50 l/min), medium (0.75 l/min), and high (1.00 l/min) plasma flow rates. A two digit nomenclature was used to indicate the current (1st number) and plasma flow rate (2nd number) for each weld, where a 2 represents the highest parameter setting and a 0 represents the lowest parameter setting. All welds were performed at a welding speed of 8 cm/min. Based on the welding parameters, the linear heat input (in J/mm) for each weldment was calculated by dividing the arc power (voltage*current) by the welding speed. Table I lists the parameters for each weld.

Weldments were cross-sectioned perpendicular to the welding direction at a distance of ~8 mm from the start of the weld. Cross-sections were polished to a mirror finish using successively finer diamond abrasives, down to 0.25 μm. Microstructural analysis of polished weldment cross-sections was performed using optical microscopy (Nikon; Epiphot 200; Tokyo, Japan) and scanning electron microscopy (Helios Nanolab 600; FEI; Hillsboro, OR). Fusion zone (FZ) areas were measured from optical images, using computer image analysis (ImageJ; National Institute of Health; Bethesda, MD), and combined with thermochemical data to estimate weld pool temperatures. Electron backscatter diffraction (EBSD) was performed on different locations in each weldment FZ. Computer software was used during the acquisition of EBSD data (Channel 5, Flamenco software; Oxford Instruments HKL; Abingdon, UK), and the creation of inverse pole figures (Channel 5, Tango and Mambo software).

3. RESULTS AND DISCUSSION

3.1 Weldment FZ Analysis

The weld pool area of each weldment was measured from perpendicular cross-sections of each weldment, Figure 1. Weldment 02 (Figure 1a) was full penetration, and had a surface width of 5.7 mm and a base width of 0.5 mm. The FZ depth of weldment 02 was 3.8 mm. Weldment 02 had a FZ cross-sectional area of 0.096 cm^2. Weldment 11 (Figure 1b) was also full penetration, and had a surface width of 6.2 mm and a base width of 0.7 mm. The surface of the weldment 11 FZ was convex, and the FZ depth was 4.6 mm. Weldment 11 had a FZ cross-sectional area of 0.132 cm^2. Spherical pores up to ~110 μm were observed at the FZ/HAZ (fusion zone/heat affected zone) interface for both weldments 02 and 11. The weldment 20 FZ was observed throughout thickness of the weldment (Figure 1c), but the weldment 20 FZ did not have the cone-like appearance of a keyhole weld.[31-33] The FZ below the outline in Figure 1c also contained C, like that of weldment-2 from King et al., and FZ area under the outline in Figure 1c was not considered in further calculations, therefore, only ZrB_2-ZrC FZs (composition) were analyzed.[22] Weldment 20 had a surface width of 9.3 mm, and a penetration depth of ~2.3 mm. The cross-sectional area considered for weldment 20 was 0.086 cm^2. Considering the FZ width to be equivalent to the diameter of the arc (arc spot size), it was observed that arc spot size increased with increasing current, but decreasing the plasma flow rate to 0.50 l/min affected the penetration depth of weldment 20. Weldment 11 had the largest cross-sectional area (0.132 cm^2), followed by weldment 02 (0.096 cm^2), and weldment 20 had the smallest cross-sectional area (0.086 cm^2).

3.2 PAW Heat Input

Thermochemical data from the NIST-JANAF tables was used with Equation 1 to calculate the energy required to melt the weld pool (E_{melt}) volumes in Table I (starting temperature of 1450°C/1723 K), where m is the number of moles in the weld pool, $C_{p,s}$ is the heat capacity of the solid, and ΔH_{fusion} is the latent heat of fusion, where $C_{p,s}$ and ΔH_{fusion} were calculated using a linear volumetric rule of mixtures.[34] Weldment volumes were calculated by assuming a constant cross-sectional area for a length of 1 mm, and the number of moles in the volume of each weld pool was calculated by assuming that the density of each weld pool was that of the PM. Also, the ZrB_2-ZrC system has a binary eutectic, but a single melting temperature (ZrB_2, T_m=3245°C/2618 K) was used when calculating the energy required for melting the weld pool volume. The E_{melt} was calculated to be 133 J for weldment 02, 183 J for weldment 11, and 119 J for weldment 20.

$$E_{melt} = m\left(\Delta H_{fusion} + \int_{1723}^{2618} C_{p,s}\, dT\right) \qquad \text{(Eq. 1)}$$

Heating of the PM was also taken into account, as during welding, the entire ZrB_2-20ZrC coupon becomes visibly brighter, i.e. hotter. To estimate the energy required to heat the PM, the temperature in the HAZ was assumed to be 3245°C at the FZ interface, but not melted, and the temperature of the PM at the end of the coupon was assumed to be 1980°C, as no change was observed in the PM microstructure, and the PM was processed at 1980°C. By removing ΔH_{fusion} from Equation 1, and integrating over the 11 mm width of the coupons (22 mm for the width of two coupons being welded together), the energy required to heat the PM was calculated to be 482 J. Therefore, the energy required to melt the volume of each weld pool, from Table I, and the energy required to heat the PM were combined, giving a necessary energy input of 601 J for weldment 02, 665 J for weldment 11, and 615 J for weldment 20. The calculated energies for melting and heating the PM agree well with the observation that weldment 11 (highest energy input, 665 J) had the largest weld pool volume, and weldment 20 (lowest energy input, 601 J) had the smallest weld pool volume.

Equation 2 was used as an initial estimate for the weld pool temperature (T_w), where η is the power transfer efficiency for PAW, E_I is the energy input for the weldment, E_{PM} is the energy required for heating the PM, and $C_{p,l}$ is the heat capacity of the liquid. Previously reported η for PAW, 50 to 75%, were used for T_w calculations.[35-37] For weldment 02, T_w was calculated to be between ~29,000°C (50% efficiency) and ~48,000°C (75% efficiency). For weldment 11, T_w was between ~25,000°C and ~40,000°C, and T_w was between ~43,000°C and ~70,000°C for weldment 20. With expected PAW arc temperatures between 10,000°C and 20,000°C, it was concluded that the estimated arc temperatures for each weldment were incorrect.[36]

$$T_w = T_m + \frac{\eta E_I - (E_m + E_{PM})}{m C_{p,l}} \qquad \text{(Eq. 2)}$$

For comparison, the FZ of a Duplex 2205 stainless steel (UNS S32205) from Ureña et al. was analyzed in the same manner as the ZrB_2-20ZrC weldments, however, heating of the PM was ignored.[33] Using thermochemical data for pure iron, T_w of the Duplex 2205 FZ, a cross-sectional area of 0.085 cm^2 (length of 1 mm), was calculated to be ~2900°C (50% efficiency), slightly above the boiling point for pure iron (2750°C). Similarly, a commercially pure Ti keyhole welded by GTAW was analyzed. Titanium welds were those of Lathabai et al., and η for GTAW was assumed to be 45%.[32,36] With a fusion zone cross-sectional area of 1.3 cm^2 (length of 1 mm), T_w was calculated to be ~2200°C, well below the boiling point of Ti (3287°C). Since PM heating was ignored for both metal welds, the estimated weld pool temperatures were concluded to be reasonable, and the calculated weld pool temperatures for the ZrB_2-20ZrC weldments were overestimated due to an incorrect assumption for the value of η. The NIST-JANAF thermochemical tables include data for ZrC to 6000 K and 5000 K for ZrB_2, however, no data are available for gaseous phases, and T_w for the ZrB_2-20ZrC weldments was assumed to reach the maximum temperature which data are available for ZrC, ~5700°C.[34] Therefore, η can be estimated to be less <20% for weldments 02 and 11, and <15% for weldment 20. It was determined that power transfer, from the arc to the workpiece, during PAW of ZrB_2-20ZrC was less efficient than observed for metals.

Although the weld pool temperatures could not be accurately estimated, normalizing T_w calculations to the respective weld pool volumes for each weldment can be used to estimate the relative weld pool temperature. By this method, weldment 20 would have reached the highest temperature. Assuming the same η for weldment 02 and weldment 11, weldment 02 would have had the second highest temperature and weldment 11 would have had the lowest weld pool temperature of the three weldments. This same method demonstrated that η for weldment 20 was the lowest. This agreed well with the work of Metcalfe and Quigley, who calculated η for keyhole and non-keyhole welds, where non-keyhole welds had an η of 60%, and keyhole welds had an η of 66%.

This occurs as the heat transfer from a plasma gas that flows through the weld pool (keyhole) is more efficient at heat transfer than an impinging gas flow (non-keyhole). Weld pool temperatures were not accurately estimated, but weld pool temperatures of each weldment were determined relative each other, with weldment 20 having the hottest weld pool, weldment 02 second hottest, and weldment 11 having the coolest weld pool temperature.

3.3 ZrB_2 Texture

EBSD was performed on the PM. A grain map and an inverse pole figure (Figure 2) were made from the crystallographic data to determine if texture was present in the PM. The distribution of ZrB_2 orientations in the inverse pole figure indicated that the PM had a random distribution of ZrB_2 crystallographic directions. White space in Figure 2 was the location of ZrC grains in the PM. The orientation of ZrC grains was mapped and the crystallographic orientation of ZrC was also random, but orientation maps of ZrC were not presented. The crystallographic orientation of the PM was random, revealing that the PM did not have microstructural texture.

EBSD was also performed on 3 different locations within the FZ for each weldment. EBSD patterns were taken at the surface, middle, and bases of each FZ. White space within weldment FZ EBSD maps was the location of either ZrC or ZrB_2-ZrC eutectic, which will be discussed later, as current discussion will focus on mapped ZrB_2. In weldment 02, grains near the surface of the weld were the largest of the weldment, with grains more than 100 μm in length. This was observed in Figure 3a, where the ZrB_2 grains take up most of the EBSD map. Due to the large size of the ZrB_2 grains, the surface of the weldment 02 FZ appears heavily textured. Near the middle of the weld pool, the growth of grains was hindered (~65 to ~160 μm grain lengths), and the number of grains was observed to increase (Figure 3b). The growth of ZrB_2 grains was observed to occur in clusters, or stacks, where grains growing within the same stack had the same crystallographic orientation. In the base of the weldment 02 FZ (Figure 3c), the frequency of ZrB_2 grains increased, while their lengths were similar to the middle of the FZ (~25 to ~170 μm grain lengths). Grain stacks were also observed at the base of the FZ, similar to those in the middle of the FZ. As the grain size throughout the FZ appeared to decrease deeper into the FZ, the FZ temperature is thought to have also decreased through the thickness of the FZ. Texture and grain size decreased, and the frequency of ZrB_2 grains increased when moving from the surface to the base of the weldment 02 FZ. Globally (all inverse pole figures considered), the weldment 02 FZ had no measurable texture.

EBSD maps of the weldment 11 FZ are presented in Figure 4. At the surface of the FZ grains ranged from ~40 to ~200 μm in length (Figure 4a). Weldment 11 did not exhibit observed surface texture, like weldment 02, indicated by the increased number of points in the inverse pole figure (Figure 4a vs Figure 3a). However, similar to the middle of the weldment 02 FZ, grain growth at the surface of the weldment 11 FZ occurred in stacks, and at a higher magnification, the surface of the weldment 11 FZ appeared to have texture. In the middle of the FZ (Figure 4b), grain stacks were observed, but the number of grains within a stack decreased. ZrB_2 grains also increased in size (~80 to ~380 μm in length). The change in ZrB_2 grain size between the surface and the middle of the FZ is likely a result of temperature, as the middle of the FZ was insulated by the rest of the weldment and PM during cooling, it stayed hotter, leading to increased grain growth.[38] At the base of the weldment 11 FZ (Figure 4c), grain sizes were observed to be within a similar range to that of the surface, 25 to 140+ μm in length. Grain stacks were also observed in the base of the weldment 11 FZ, but the number of grains within a stack was observed to be similar to the middle of the FZ. Texture was not observed to change throughout the weldment 11 FZ. Weldment 02 and weldment 11 had similar EBSD maps and inverse pole figures throughout the FZ, with the exception of the surface map for weldment 02. However, comparing Figure 1a and 1b, reveals that the microstructures of weldments 02 and 11 are similar near the surface, and the texture in Figure 3a was location dependent. Another EBSD map is not presented, but other indexed locations at the surface of the weldment 11 FZ exhibited texture, like the surface of weldment 02. Grain lengths were similar at the surface and base of the weldment 11 FZ, but grain sizes increased in the middle of the FZ. Globally, the weldment 11 FZ was not textured. Weldments 02 and 11 were determined to have similar microstructures and microstructural textures, therefore, the temperature profiles of the two FZs were likely similar.

Grains in the weldment 20 FZ were larger than grains in the FZs for weldments 02 and 11. ZrB_2 grains in Figure 5 were larger than the image, therefore, ZrB_2 grains in the weldment 20 FZ were estimated to be between ~100 and +200 μm in length. Similar grain sizes were observed throughout the depth of the weldment 20 FZ. Large ZrB_2 grains give the appearance of texture at the surface (Figure 5a) and base (Figure 5b) of the FZ. As the depth of the weldment 20 FZ was only ~2.3 mm, the FZ base was similar in depth to the middle of the weldment 02 and 11 FZs. A third location at the side of the FZ was indexed (Figure 5c), and the side of the FZ also exhibited texture. At each location, grain stacks were observed. As weldment 20 was expected to have the highest weld pool temperature, the growth of grains was likely the dominant solidification mechanism, compared to the nucleation of new grains.[38] Hence, weldment 20 contained the largest observed ZrB_2 grains and the weldment 20 FZ had texture at the micro and global levels.

Due to the exaggerated growth (preferred growth in one direction) of ZrB_2 in the weldment 20 FZ, the surface of the weldment was examined from a top-down perspective, or the area of arc impingement. A stitched optical image of the FZ surface (Figure 6) reveals that the weld pool diameter was not consistent, and varied from 5.9 mm (bottom of Figure 6) to 6.8 mm (top of Figure 6) in width. This width does not agree with the previously reported FZ width of 9.3 mm. From Figure 1a and 1c, it can be observed that the depth of the FZ was not consistent across the width of the weldment, e.g. wavy, which could occur with slight inconsistencies in the welding current, plasma flow rate, or speed, as more or less material is melted. It was determined that during grinding and polishing, the sides of the FZ in Figure 6 were ground more than the center of the FZ, and the center of the Figure 6 FZ is representative of the direct weldment surface, while the sides of the FZ were ground ~0.3 mm deep into the FZ, hence the decrease in observed FZ width. At the center of the FZ, ZrB_2 grew in the welding direction, with ZrB_2 grains growing to lengths of >2 mm. The direction of growth agrees well with the notion that for arc welding processes, grains grow toward the heat source.[39] As the grains at the surface follow the thermal gradient produced by arc movement, EBSD indexing of the weldment 20 surface (Figure 7) was used to determine how ZrB_2 grew after nucleation. The surface appeared highly textured and indicated that ZrB_2

growth was in the basal plane, giving ZrB_2 a plate-like structure. Further analysis on a fracture surface of a previously welded specimen (same welding parameters as weldment 11), revealed a free surface, and ledge growth of ZrB_2 was observed (Figure 8).[39,40] ZrB_2 grains were determined to grew along the basal plane, increasing their thickness by ledge growth mechanisms.

3.4 ZrC Precipitation

The precipitation of ZrC in each weldment occurred by two different mechanisms. The first mechanism was solidification of the binary eutectic. The ZrB_2-ZrC eutectic solidified along a thermal gradient, leading to the formation of cellular ZrB_2-ZrC eutectic (~43 vol% ZrC).[2] The formation of cellular diboride-carbide eutectic in fusion welded ceramics was previously observed, leading to the conclusion that the eutectic solidified along an equilibrium cooling path.[22,23] Solidification of ZrC through the eutectic was determined to be equilibrium solidification for all three weldments described in the present study.

The formation of cellular ZrB_2-ZrC eutectic was observed in each weldment, but it should also be noted that the presence of eutectic was not observed between ZrB_2 grains in a grain stack. Rather, between ZrB_2 grains within a stack, only ZrC is present. It was determined that these regions did not solidify on an equilibrium cooling path, but, when ZrB_2 nucleated and/or grews at high enough rates, the weld pool liquid became depleted of B, forcing the precipitation of ZrC from the liquid. As previously mentioned, this occured within ZrB_2 grain stacks, and ZrB_2 grains “split” as ZrC began to precipitate. Demonstrated with the secondary electron image of the Figure 7 EBSD map, in Figure 9, two ZrB_2 grains of different orientations were observed to split and grow around ZrC.

This suggests that instead of a grain stack, consisting of individual ZrB_2 grains of similar orientation, a ZrB_2 stack at the surface of the 20 weld is one grain. Splitting of the grain stacks was also observed in the higher nucleation rate regions of weldment 02 (middle and base) and weldment 11 (surface, middle, and base), where stacks of the same orientation were connected. EBSD indexing of ZrC within a ZrB_2 stack/grain revealed multiple orientations of ZrC, indicating that ZrC did not grow epitaxially from the crystallographic orientation of ZrB_2. Precipitation of ZrC occurred through the formation of the equilibrium ZrB_2-ZrC eutectic (equilibrium solidification), or by forced precipitation as rapid growth of ZrB_2 desaturated the weld pool liquid of B (non-equilibrium solidification), also revealing that a stack of ZrB_2 grains was not multiple grains, but a single grain.

4. SUMMARY

Three sets of PAW parameters were used to fusion weld ZrB_2-20ZrC ceramics. Cross-sectional areas were 0.096 cm^2 for weldment 02 (176 A, 1.00 l/min), 0.132 cm^2 for weldment 11 (198 A, 0.75 l/min), and 0.086 cm^2 for weldment 20 (222 A, 0.50 l/min). Weld pool cross-sectional areas were normalized to a weld pool length of 1 mm, and the amount of material in the weld pool volume was used to estimate weld pool temperature. Weld pool temperatures ranging from ~24,000°C to ~70,000°C were estimated using estimated heat input efficiencies of 50-65%, but were not realistic. By assuming a lower melt pool temperature for each weldment, 5700°C, heat input efficiencies were estimated to be <20% for keyhole welds (weldments 02 and 11), and <15% for non-keyhole welds (weldment 20). Weld pool temperatures were determined relative to the other weldments, where the hottest weld pool was from weldment 20, and the coolest weld pool was from weldment 11. The hottest weld pool resulted in the growth of large ZrB_2 grains (+200 μm) the FZ, and the FZ had texture at micro and global levels. ZrB_2 grain lengths were shorter in weldments 02 and 11, but ranged from 25 to 380 μm. Microstructurally, weldment 02 and 11 were observed to have texture at the surface of the FZ, but globally their FZs did not have texture. Exaggerated growth of ZrB_2 at the surface of weldment 20 and an exposed free surface revealed that ZrB_2 grew as plates along the basal plane, and by ledge growth mechanisms. In regions of high nucleation and growth rates, ZrB_2 grains appeared to form grain stacks, rather, ZrB_2 grains split around ZrC that was forced to precipitate, due to desaturation of B from the melt pool liquid by fast nucleation/growth of ZrB_2. Lower nucleation and growth rates resulted in equilibrium cooling of the weld pool liquid, where ZrC was observed to precipitate in the binary eutectic.

ACKNOWLEDGEMENTS

Research was conducted in cooperation with MO-SCI Corporation and supported by AFOSR Grant # FA9550-12-C-0060. The authors acknowledge Andrew Schlup and Cari Swanson for their assistance with materials and image processing. The authors would also like to thank the Advanced Materials Characterization Laboratory (AMCL) at Missouri S&T for use of their equipment.

REFERENCES

[1]F. Monteverde, A. Bellosi, and S. Guicciardi, "Processing and properties of zirconium diboride-based composites," *J. Eur. Ceram. Soc.*, **22**[3] 279-88 (2002).

[2]E. Rudy and S. Windish, "Ternary Phase Equilibria in Transition Metal-Boron-Carbon-Silicon System: Part V. Compendium of Phase Diagram Data." in**.** Air Force Materials Laboratory, AFML-TR-65-2, Wright Patterson Air Force Base, OH, 1966.

[3]W. G. Fahrenholtz, G. E. Hilmas, I. G. Talmy, and J. A. Zaykoski, "Refractory Diborides of Zirconium and Hafnium," *J. Am. Ceram. Soc.*, **90**[5] 1347-64 (2007).

[4]S.-Q. Guo, T. Nishimura, T. Mizuguchi, and Y. Kagawa, "Mechanical properties of hot-pressed ZrB_2–$MoSi_2$–SiC composites," *J. Eur. Ceram. Soc.*, **28**[9] 1891-98 (2008).

[5]S. C. Zhang, G. E. Hilmas, and W. G. Fahrenholtz, "Pressureless Densification of Zirconium Diboride with Boron Carbide Additions," *J. Am. Ceram. Soc.*, **89**[5] 1544-50 (2006).

[6]J. Watts, G. Hilmas, and W. G. Fahrenholtz, "Mechanical Characterization of ZrB_2–SiC Composites with Varying SiC Particle Sizes," *J. Am. Ceram. Soc.*, **94**[12] 4410-18 (2011).

[7]A. L. Chamberlain, W. G. Fahrenholtz, G. E. Hilmas, and D. T. Ellerby, "High-Strength Zirconium Diboride-Based Ceramics," *J. Am. Ceram. Soc.*, **87**[6] 1170-72 (2004).

[8]D. Sciti, F. Monteverde, S. Guicciardi, G. Pezzotti, and A. Bellosi, "Microstructure and mechanical properties of ZrB_2–$MoSi_2$ ceramic composites produced by different sintering techniques," *Materials Science and Engineering: A*, **434**[1–2] 303-09 (2006).

[9]S. C. Zhang, G. E. Hilmas, and W. G. Fahrenholtz, "Mechanical properties of sintered ZrB_2–SiC ceramics," *J. Eur. Ceram. Soc.*, **31**[5] 893-901 (2011).

[10]S. C. Zhang, G. E. Hilmas, and W. G. Fahrenholtz, "Pressureless Sintering of ZrB_2–SiC Ceramics," *J. Am. Ceram. Soc.*, **91**[1] 26-32 (2008).

[11]E. W. Neuman, G. E. Hilmas, and W. G. Fahrenholtz, "Strength of Zirconium Diboride to 2300°C," *J. Am. Ceram. Soc.,* **96**[1] 47-50 (2013).

[12]J. Barcena, J. Coleto, S. C. Zhang, G. E. Hilmas, and W. G. Fahrenholtz, "Processing of Carbon Nanofiber Reinforced ZrB2 Matrix Composites for Aerospace Applications," *Advanced Engineering Materials,* **12**[7] 623-26 (2010).

[13]S. Prochazka and R. M. Scanlan, "Effect of Boron and Carbon on Sintering of SiC," *J. Am. Ceram. Soc.,* **58**[1-2] 72-72 (1975).

[14]W. R. Pinc, M. Di Prima, L. S. Walker, Z. N. Wing, and E. L. Corral, "Spark Plasma Joining of ZrB_2–SiC Composites Using Zirconium–Boron Reactive Filler Layers," *J. Am. Ceram. Soc.,* **94**[11] 3825-32 (2011).

[15]M. Singh and R. Asthana, "Joining and integration of ZrB_2-based ultra-high temperature ceramic composites using advanced brazing technology," *J. Mater. Sci.,* **45**[16] 4308-20 (2010).

[16]M. Singh and R. Asthana, "Joining of ZrB_2-Based Ultra-High-Temperature Ceramic Composites to Cu–Clad–Molybdenum for Advanced Aerospace Applications," *Int. J. Appl. Ceram. Technol.,* **6**[2] 113-33 (2009).

[17]L. Esposito and A. Bellosi, "Joining ZrB_2-SiC composites using glass interlayers," *J. Mater. Sci.,* **40**[17] 4445-53 (2005).

[18]S. Grasso, P. Tatarko, S. Rizzo, H. Porwal, C. Hu, Y. Katoh, M. Salvo, M. J. Reece, and M. Ferraris, "Joining of β-SiC by spark plasma sintering," *J. Eur. Ceram. Soc.,* **34**[7] 1681-86 (2014).

[19]S. Rizzo, S. Grasso, M. Salvo, V. Casalegno, M. J. Reece, and M. Ferraris, "Joining of C/SiC composites by spark plasma sintering technique," *J. Eur. Ceram. Soc.,* **34**[4] 903-13 (2014).

[20]T. Okuni, Y. Miyamoto, H. Abe, and M. Naito, "Joining of AlN and graphite disks using interlayer tapes by spark plasma sintering," *Materials & Design,* **54**[0] 755-59 (2014).

[21]T. Okuni, Y. Miyamoto, H. Abe, and M. Naito, "Joining of silicon carbide and graphite by spark plasma sintering," *Ceram. Int.,* **40**[1, Part B] 1359-63 (2014).

[22]D. S. King, G. E. Hilmas, and W. G. Fahrenholtz, "Plasma arc welding of ZrB_2-20 vol% ZrC ceramics," *J. Eur. Ceram. Soc.*, **34**[15] 3549-57 (2014).

[23]D. S. King, G. E. Hilmas, and W. G. Fahrenholtz, "Plasma Arc Welding of TiB_2-20 vol.% TiC," *J. Am. Ceram. Soc.*, **97**[1] 56-59 (2014).

[24]G. E. Hilmas, W. G. Fahrenholtz, J. L. Watts, and H. J. Brown-Shaklee, "Ceramic welds, and a method for producing the same," U.S. Patent 8,715,803, (2014).

[25]M. Ikeda, "Ceramics Welding with Laser," *Taikabutsu Overseas*, **5**[3] 27-33 (1985).

[26]J. F. Li, L. Li, and F. H. Stott, "Thermal stresses and their implication on cracking during laser melting of ceramic materials," *Acta Mater.*, **52**[14] 4385-98 (2004).

[27]V. A. Burdovitsin, A. S. Klimov, and E. M. Oks, "On the possibility of electron-beam processing of dielectrics using a forevacuum plasma electron source," *Technical Physics Letters*, **35**[6] 511-13 (2009).

[28]V. A. Burdovitsin, A. S. Klimov, A. V. Medovnik, and E. M. Oks, "Electron beam treatment of non-conducting materials by a fore-pump-pressure plasma-cathode electron beam source," *Plasma Sources Science and Technology,* **19**[5] 055003 (2010).

[29]R. W. Rice, "Joining of Ceramics," pp. 69-111 in Advances in joining technology: proceeding of the 4th Army Materials Technology Conference, Boston, MA, 1976.

[30]S. S. Ordan'yan, V. I. Unrod, and A. I. Avgustinik, "Reactions in the System TiC_x-TiB_2," *Sov. Powder Metall. Met. Ceram.*, **14**[9] 729-31 (1975).

[31]C. S. Wu, C. B. Jia, and M. A. Chen, "A Control System for Keyhole Plasma Arc Welding of Stainless Steel Plates with Medium Thickness," *Supplement to the Welding Journal,* **89** 225-31 (2010).

[32]S. Lathabai, B. L. Jarvis, and K. J. Barton, "Comparison of keyhole and conventional gas tungsten arc welds in commercially pure titanium," *Materials Science and Engineering: A*, **299**[1–2] 81-93 (2001).

[33] A. Ureña, E. Otero, M. V. Utrilla, and C. J. Múnez, "Weldability of a 2205 duplex stainless steel using plasma arc welding," *Journal of Materials Processing Technology,* **182**[1–3] 624-31 (2007).

[34] J. M.W. Chase, C. A. Davies, J. J.R. Downey, D. J. Frurip, R. A. McDonald, and A. N. Syverud, "NIST-JANAF Thermochemical Tables," http://kinetics.nist.gov/janaf/.

[35] W. G. Essers and R. Walter, "Heat Transfer and Penetration Mechanisms with GMA and Plasma-GMA Welding," *Welding Journal,* **60**[2] 37-42 (1981).

[36] J. C. Metcalfe and M. B. C. Quigley, "Heat transfer in plasma-arc welding," *Welding Journal*, **54**[3] 99-103 (1975).

[37] D. M. Evans, D. Huang, J. C. McClure, and A. C. Nunes, "Arc Efficiency of Plasma Arc Welding," *Welding Journal,* **77**[2] 53-8 (1998).

[38] J. E. Shelby, "Introduction to Glass Science and Technology," Second ed. The Royal Society of Chemistry: Cambridge, UK, (2005).

[39] D. A. Porter and K. E. Easterling, "Phase Transformations in Metals and Alloys," Second ed. Chapman & Hill: London, UK, (1992).

[40] G. J. Shiflet, M. A. Mangan, and W. G. Meng, "Growth by Ledges," *Interface Science,* **6**[1-2] 133-54 (1998).

Table I: PAW parameters, heat input, and FZ size

Weldment	Current (A)	Voltage (V)	Plasma Flow Rate (l/min)	Welding Speed (cm/min)	Heat Input (J/mm)	Weld Pool Volume (cm^3)
02	176	28	1.00	8	3697	$9.6x10^{-3}$
11	198	28	0.75	8	4159	$1.3x10^{-2}$
20	222	28	0.50	8	4663	$8.6x10^{-3}$

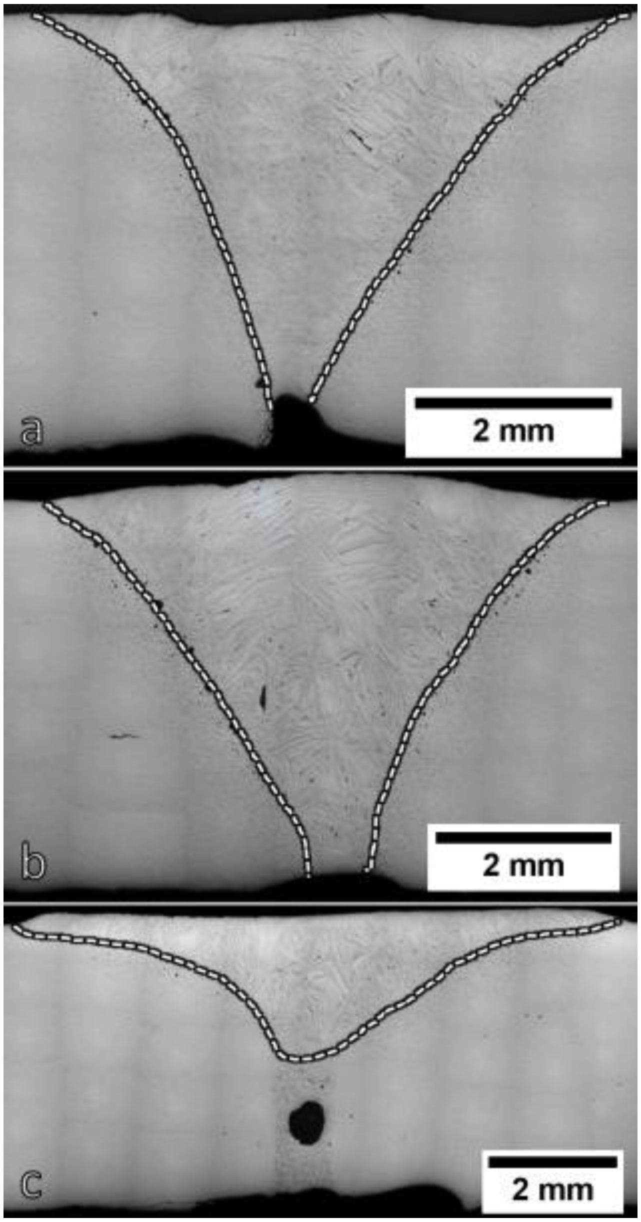

Figure 1: Three weldment cross-sections, cut perpendicular to the welding direction, with the FZ outlined. Weldment 02 (a) and weldment 11 (b) were considered full penetration keyhole welds, due to their cone-like appearance. Weldment 20 (c) was not considered a to be a key hole weld.

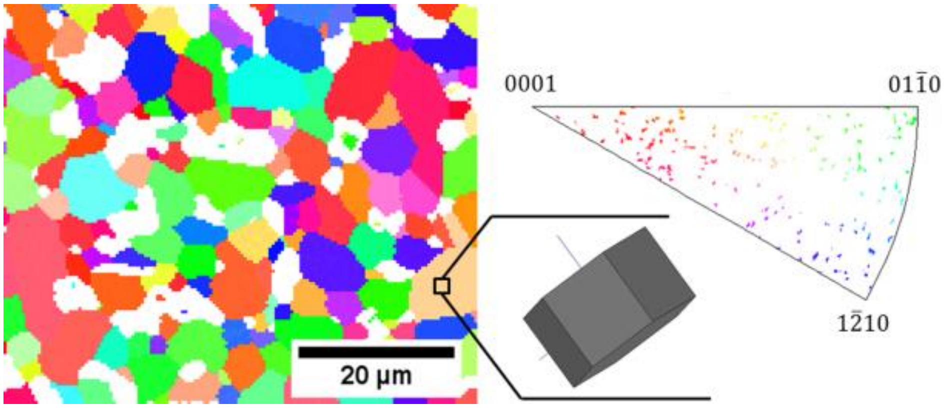

Figure 2: EBSD map of the PM with the corresponding inverse pole figure, where the PM exhibits random orientation. White space in the map on the left indicates the location of ZrC in the PM.

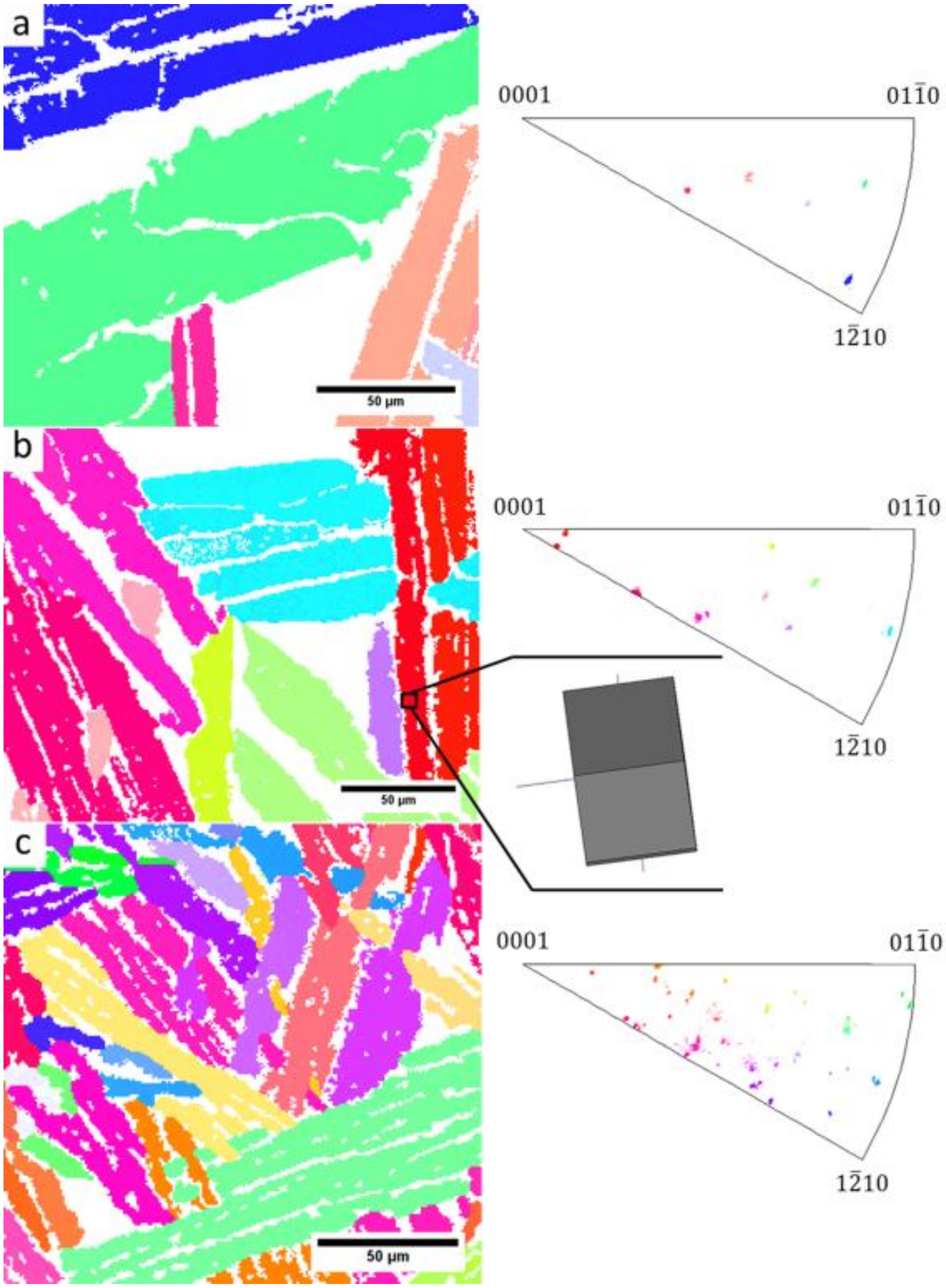

Figure 3: EBSD maps from near the surface (a), middle (b), and base (c) of the weldment 02 FZ and their corresponding inverse pole figures. A 3D hexagon represents the orientation of a specific grain.

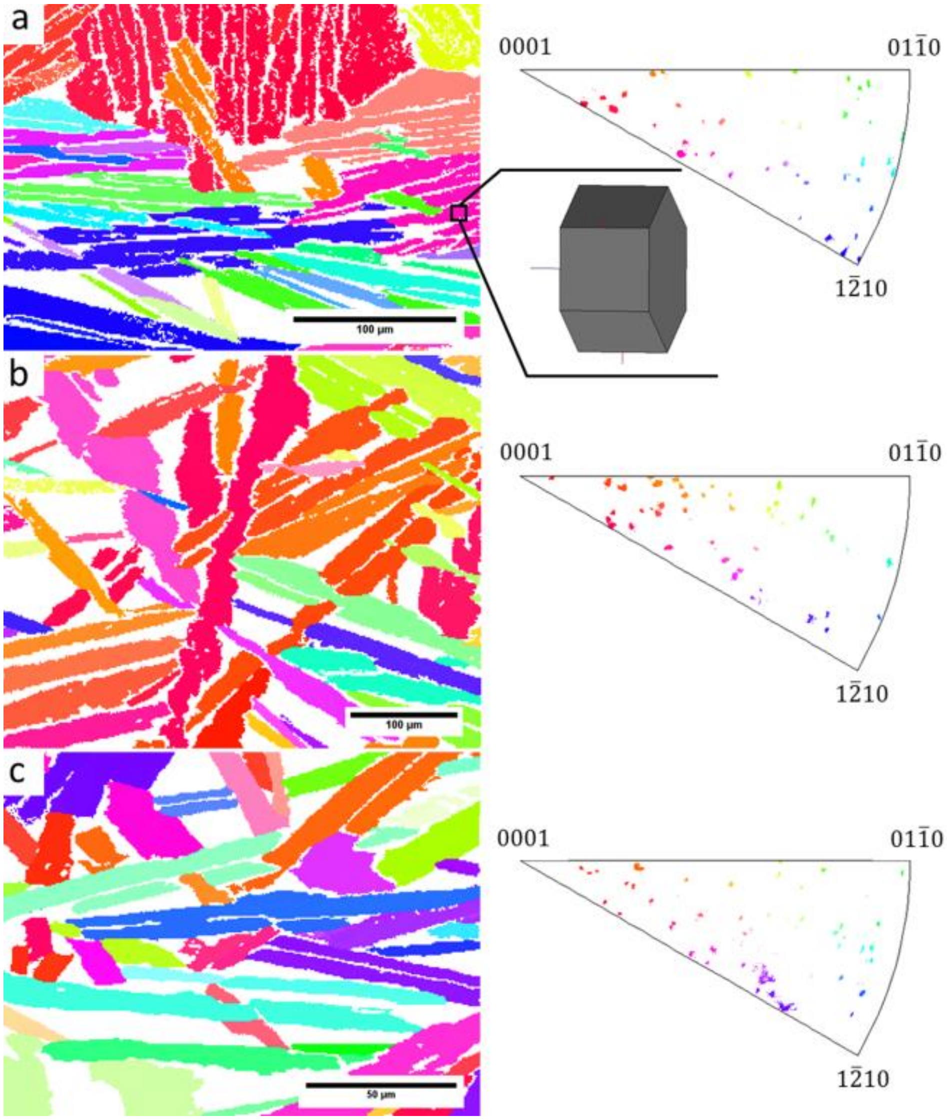

Figure 4: EBSD maps from near the surface (a), middle (b), and base (c) of the weldment 11 FZ and their corresponding inverse pole figures. A 3D hexagon represents the orientation of a specific grain.

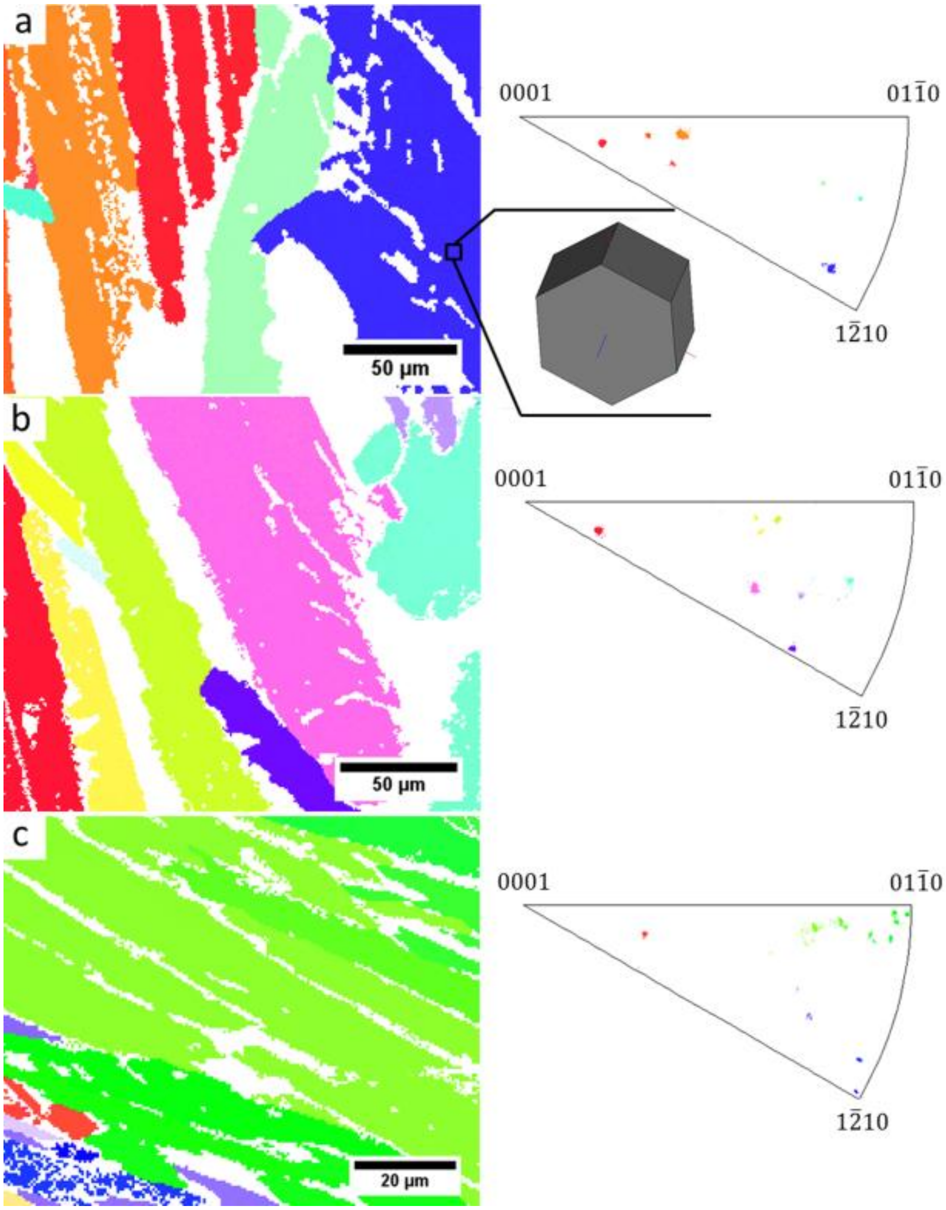

Figure 5: EBSD maps from near the surface (a), base (b), and side (c) of the weldment 20 FZ and their corresponding inverse pole figures. A 3D hexagon represents the orientation of a specific grain.

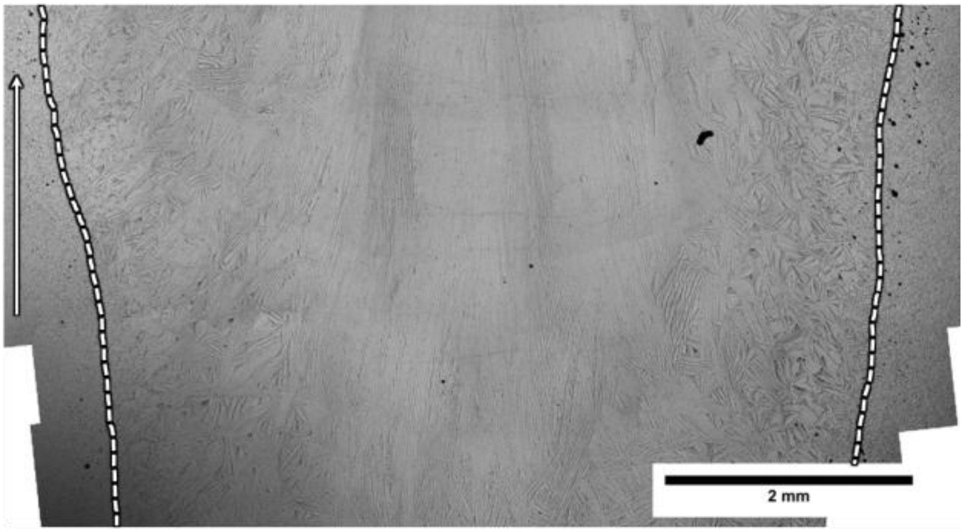

Figure 6: A top-down (surface of arc impingement) optical image of the weldment 20 FZ. The FZ is outlined, and an arrow points in the welding direction. Grains were observed to be as long as 2 mm in length, growing in the direction of the arcs thermal gradient.

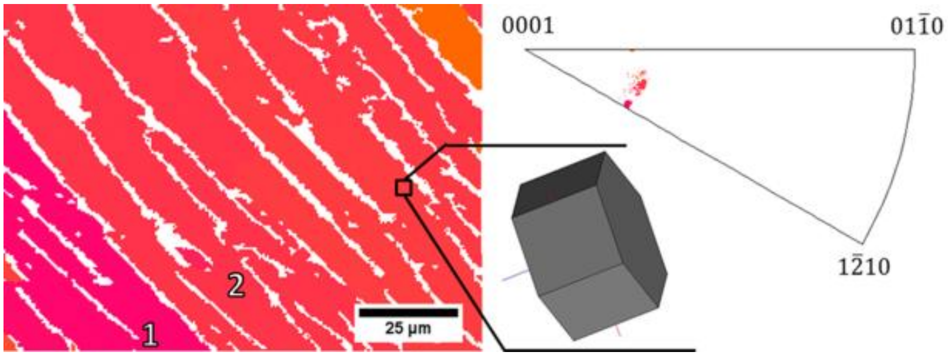

Figure 7: EBSD map from the top-down surface of the weldment 20 FZ and the corresponding inverse pole figures. A highly textured surface, grain growth occurs in the direction of the arcs thermal gradient. A 3D hexagon represents the orientation of a specific grain.

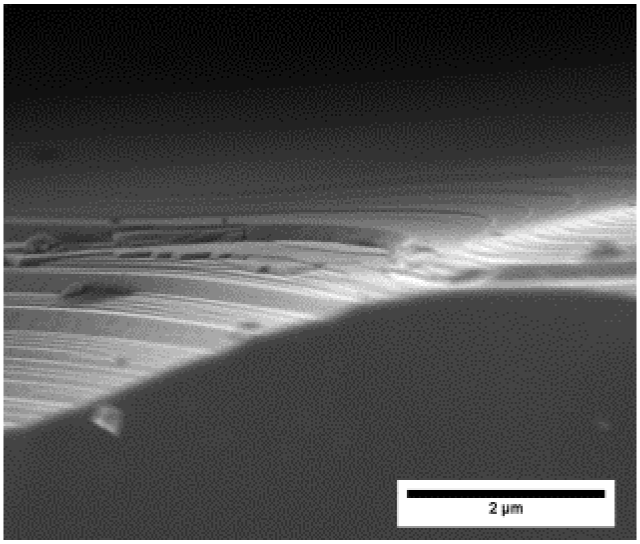

Figure 8: Secondary electron image of a weldment 11 fracture surface, exposing a free surface, where ledge growth of ZrB_2 was observed.

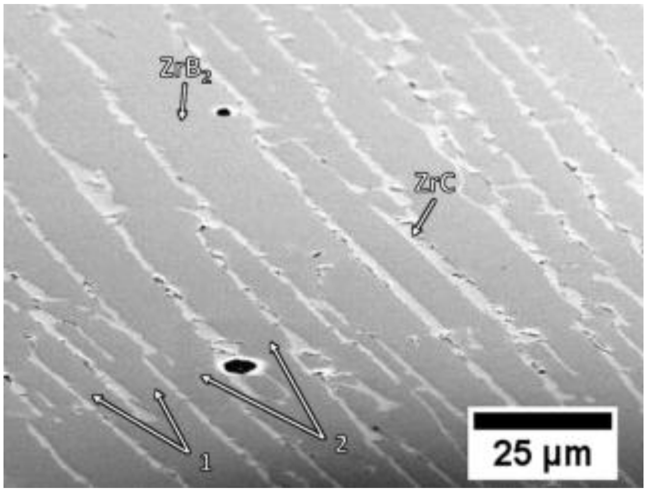

Figure 9: Secondary electron image of the weldment 20 FZ surface. Arrows indicate splitting of ZrB$_2$ within the same grain stack. Points 1 and 2 correspond to points 1 and 2 in Figure 7. Image tilted 72° relative to electron beam for EBSD indexing.

IV. PLASMA ARC WELDING OF TiB_2-20 VOL% TiC

Derek S. King, Greg E. Hilmas, William G. Fahrenholtz
Missouri University of Science and Technology
Materials Science and Engineering Dept.
Rolla, MO 65409
Corresponding Author Contact
Email: dsk2nf@mst.edu
Phone: 1-573-341-7205
Fax: 1-573-341-6934

ABSTRACT

Ceramics consisting of titanium diboride with titanium carbide additions were fusion welded to produce continuous joins. A welding current of 135 A, welding speed of 8 cm/min, and plasma flow rate of 0.75 l/min were combined with a pre-heat temperature of ~1450°C to fusion weld coupons of TiB_2 containing 20 vol.% TiC with a thickness of 4 mm. The resulting fusion zone was 3.9 mm deep at the center of the joint and 10.4 mm wide. During cooling of the melt pool, four distinct regions of crystal growth and nucleation were observed due to thermal gradients. Regions at the top and bottom of the fusion zone exhibited smaller TiB_2 crystals due to higher nucleation rates while regions in the middle of the fusion zone showed higher growth rates, with TiB_2 crystals up to 1.2 mm in length. Thermal gradients also affected cooling of the eutectic phase, causing a cellular structure to appear in the cooled eutectic. Plasma arc welding was a viable method for joining diboride-based ceramics.

1. INTRODUCTION

Processing methods, such as hot pressing and spark plasma sintering, that are typically used for the densification of ultra-high temperature ceramics (UHTCs) and other materials for extreme environments, are limited to the fabrication of relatively simple shapes.[1] Ceramic joining may allow for the production of more complex shaped parts. Methods such as solid-state diffusion bonding or brazing have been used to join UHTCs.[1-3] Brazing is a versatile technique that can join a variety of materials, but braze alloy melting temperatures limit subsequent use temperatures. Alloys with higher melting temperatures, such as Pd alloys, have been investigated, but their melting temperatures are still below the expected use temperatures for UHTCs, which are 2000°C or higher.[1,3] Pressureless sintering can be used to produce solid-state joints between UHTCs. However, densification of many UHTC materials requires pressure to accompany the elevated temperatures required for densification, which could limit complex shape formation.[1,4]

Fusion welding of UHTCs combines the versatility of brazing with the ability to use joined components near the same temperature as the parent materials. This would allow for the production of complex shapes having solid-state like joints. Fusion welding may also be useful in joining dissimilar materials, including joining ceramics to refractory metals. Fusion welding of ceramics has been shown to be feasible using electron beam, laser, and arc welding techniques.[5] While past investigations of arc welding of ceramics have been limited, it is possible, and likely the most cost effective of the three fusion welding techniques.[5]

The purpose of this communications is to evaluate fusion welding of UHTCs through plasma arc welding. Using plasma arc welding, TiB_2 containing 20 vol.% TiC was joined. Microstructure analysis was used to identify the fusion zone and microstructural changes that formed during cooling of the weld region.

2. EXPERIMENTAL PROCEDURE

Titanium diboride-titanium carbide (TiB_2-TiC) ceramics with a nominal carbide content of 20 vol.% were prepared for plasma arc welding. TiB_2 (Momentive; Grade HCT-F; Columbus, OH) and TiC (Materion Advanced Chemicals; -325 mesh; Milwaukee, WI) powders were mechanically mixed by ball milling. In addition, 1.25 wt.% phenolic resin (Georgia Pacific Chemicals; Atlanta, GA), which produced a final carbon content of 0.5 wt.%, was added as a sintering aid. Milling was carried out in acetone for 2 hours using TiB_2 media. After milling, the powder slurry was dried using rotary evaporation to minimize segregation of the constituents. Dried powders were then ground and sieved to -60 mesh before hot-pressing.

Billets, nominally 46.5 mm by 30.0 mm by 5.0 mm, of TiB_2-20 vol.% TiC (TiB_2-20TiC) were fabricated through hot-pressing using the procedure described by King *et al.* for SiC-TiB_2 ceramics.[6] The relative geometric densities of the pressed billets were calculated based on a volumetric rule of mixtures calculation for TiB_2-20TiC (4.60 g/cm^3). Billets with relative geometric densities over 95% were deemed appropriate for further machining and subsequent welding. Machining was performed using a surface grinder (Chevalier Machinery Inc.; Model FSG-618; Santa Fe Springs, CA) with diamond tooling (National Diamond Labs; Los Angeles, CA). Machined pieces to be welded had nominal dimensions of 15 mm by 15 mm by 4 mm.

Cut billets were butt welded in a custom welding chamber consisting of a glovebox (MBraun; UNIlab ; Garching, Germany) modified with feedthroughs for a graphite element furnace for pre-heating, cooling water for the furnace, a welding ground, power and gas for a plasma arc welding torch (Victor Technologies; Thermal Arc; PWM 300; St. Louis, MO), and electrical power. The glovebox was set to maintain argon between 100 and 450 Pa (1.0 and 4.5 mbar) over atmospheric pressure. A Thermal Arc® plasma arc welding system consisting of a coolant circulator (HE100A), power supply (ArcMaster 300S), welding console (WC-100B), weld sequencer (WC-1), and plasma arc welding torch was utilized for welding. The pre-heat furnace consisted of a graphite box with nominal inner dimensions of 12.7 cm by 12.7 cm by 5.1 cm, the graphite element, and removable top plate to serve as the welding ground. The furnace was surrounded by ~22.0 mm of graphite felt and ~6.4 cm of refractory. Temperature was monitored using a type B thermocouple. To control welding speed, the welding torch was attached to a torch track (ESAB; Model ; Gothenburg, Sweden) that allowed for variable welding speeds.

Butt weld gaps were ~0.35 mm wide and formed by separating the diced samples with 4 layers of double sided tape (3M; Scotch® Double Sided Tape; St. Paul, MN). Samples were aligned with the torch, then covered with a layer of graphite felt and pre-heated to ~1450°C. Samples were uncovered and the torch track was moved such that the torch tip was placed at one end of the sample gap. The arc was struck to the sample and welding current was increased at a rate of 17 A/s.. Once the welding current was reached, the torch track was engaged at a speed of ~8 cm/min At the end of the weld, the current was tapered 10% over a time span of 0.25 s followed by a decreasing at a rate of

11 A/s. Welded samples were covered with graphite felt and the furnace was allowed to equilibrate the temperature. The furnace and welded samples were then cooled at a rate of ~30°C/min from the equilibrated temperature to room temperature.

Joints were cut perpendicular to the welding direction using a manual surface grinder and diamond cutting wheel. Cross-sections were mounted in an epoxy resin and polished to a mirror finish using successively finer diamond abrasives with the finest abrasive being 0.25 μm. Microstructural analysis of polished cross-sections was performed using optical microscopy (Nikon; Epiphot 200; Tokyo, Japan), scanning electron microscopy (S-570, Hitachi, Tokyo, Japan), and X-ray diffraction (Phillips, X-Pert Diffractometer).

3. RESULTS AND DISCUSSION

A successful butt weld of TiB_2-20TiC, welded at 135 A with a plasma flow rate of 0.75 l/min, and exhibiting full penetration along the entire length of the joint is shown in Figure 1. Several welds were attempted with increased heat input, which was achieved by increasing current, or plasma flow rate. Higher heat input divided the weld pool and pushed it up the sides of the two coupons producing a cutting action, similar to plasma cutting. Likewise, specimens produced with decreased heat input through lower currents or plasma flow rates were not melted, meaning that a weld pool could not be established. A weld cross-section taken 3.2 mm from the start of the weld revealed that the weld pool contained large oval pores, ~1 mm at their largest diameter. The large pores were located at the edges and base of the weld pool and can be seen in Figure 1. The fusion zone (FZ) appears semi-circular, and was measured to be 10.4 mm wide at the top surface of the parent material (PM), and 3.9 mm deep at the center of the joint. A distinct heat affected zone (HAZ) was not apparent. During plasma arc welding, the plasma flow rate caused the weld pool to be partially blown up onto the top surface of the parent material. These ridges were not taken into account while measuring the fusion zone dimensions. Grazing incidence X-ray diffraction, Figure 2, identified TiB_2 and TiC as the only crystalline phases present in the weld pool. A backscatter electron image (BEI), Figure 3, also revealed two phases. Based on the atomic number contrast of the two phases identified through XRD, TiC appears light grey and TiB_2 appears dark grey in BEI images like Figure 3. In contrast, TiB_2 appears white and TiC appears light grey in optical images like Figure 1. While large pores were formed during the welding process, a full penetration weld was formed via plasma arc welding using a current of 135 A, and a plasma flow rate of 0.75 l/min. Further, the weld contained the same two phases as the parent material, TiB_2 and TiC.

Analysis of the microstructure in the FZ of the full penetration weld revealed four regions. The top surface of the fusion zone contained a large number of crystals that grew directionally to a length of ~200 μm, this region will be referred to as Region 1, and is shown at the top of Figure 4. Growth of the crystals in Region 1 likely occurred as the surface of the melt pool cooled through radiative heat losses. The cooler surface temperature allowed for a high nucleation rate as several crystals formed at the surface of the weld pool and grew directionally toward the center of the melt pool.[7] While 200 μm long crystals are large compared to the parent TiB_2, it can be seen that Region 1 did not have the largest grains.[8] Below the 200 μm layer of surface crystals, a second region can be seen with larger TiB_2 crystals, referred to as Region 2. In Region 2, it is possible that the melt retains high enough temperatures such that the nucleation rate was lower than the crystal growth rate, allowing larger crystals to grow from the melt.[7] Within Region 2, crystal lengths reached up to 1.2 mm. Region 3 is similar in TiB_2 crystal size and frequency to Region 2. However, in Region 3, the crystals likely grew from the bottom of the fusion zone to the hottest region in the weld pool where Regions 2 and 3 meet. This occurred due to the cooler Region 4, the bottom most region, acting as a cold face for Region 3 crystal growth. The large number of TiB_2 grains in Region 4 suggests a high nucleation rate, similar to Region 1.[7] Lack of directional growth, like Region 1, suggests Region 4 had the highest nucleation rate, which indicates the lowest temperature in the FZ during cooling. Each of the four regions can be seen in Figure 4, and are defined by the dashed lines. In the FZ, a hot weld pool center promoted crystal growth with crystals up to 1.2 mm in length in Regions 2 and 3, while at the cooler surfaces, a higher frequency of crystals suggests higher nucleation rates in Regions 1 and 4.

In Regions 2, 3, and 4, the areas among the TiB_2 crystals are filled with solidified eutectic that has a cellular structure. In contrast, the TiB_2 crystals in Region 1 are bordered by TiC, not solidified eutectic.[9,10] Throughout the weld, directional solidification of the eutectic is prominent due to the thermal gradients within the weld pool. The directionality of the eutectic growth was also affected by nearby large pores, growing crystals and the welding direction. Figure 5 shows eutectic that has solidified parallel to weld direction, presumably due to the thermal gradient produced by the welding process. Areal analysis of cellular eutectic was used to determine the relative eutectic composition, and gave a eutectic composition of 50.5±6.5 vol.% TiB_2 and 49.5±6.5 vol.% TiC, which agrees with previous studies.[11,12] The thermal gradients throughout the weld pool promote directional solidification of the eutectic that may cool based on the weld direction, porosity, or surrounding TiB_2 crystals.

4. SUMMARY

Plasma arc welding was used to fusion weld TiB_2-20vol.% TiC ceramic composites. A welding current of 135 A, welding speed of 8 cm/min, and plasma flow rate of 0.75 l/min were used to join TiB_2-20vol.% TiC ceramics. The FZ had a center depth of 3.9 mm and a width of 10.4 mm. Within the fusion zone, elliptical pores, up to 1 mm in diameter on their long axis, surrounded the fusion zone near the interface of the FZ and the PM. TiB_2 and TiC were confirmed to be the constituent phases using grazing incidence XRD and BEI.

Four distinct regions were observed within the FZ, each evolving from temperature gradients within the melt. Region 1 contained a high frequency of TiB_2 crystals that had grown into the melt to a length of ~200 μm. TiB_2 crystals in Regions 2 and 3 grew to lengths up to 1.2 mm due to temperatures that favored grain growth over crystal nucleation. Region 2 crystals grew downward into the melt at the Region 1-2 interface, while Region 3 crystals grew upward toward Region 2, where both regions meet. Like Region 1, Region 4 exhibited a high frequency of TiB_2 crystals, however, a lack of TiB_2 crystal growth in Region 4 suggests that nucleation rates were highest in Region 4 while the temperature throughout Region 4 was the lowest. Along with directional growth of the TiB_2 phase, directional solidification of the eutectic was seen throughout the FZ.

Plasma arc welding was demonstrated for TiB_2-20TiC ceramics, yet large crystals and pores present in the fusion zone present critical flaws that would decrease the strength of a welded joint. Nonetheless, fusion welding of UHTC ceramics was possible and further understanding of the plasma arc welding process and weld pool mechanics may lead to improvements in arc welding of ceramics.

ACKNOWLEDGEMENTS

Research was conducted in cooperation with MO-SCI Corporation and supported by AFOSR Grant # FA9550-12-C-0060.

REFERENCES

[1]W. R. Pinc, M. Di Prima, L. S. Walker, Z. N. Wing, and E. L. Corral, "Spark Plasma Joining of ZrB_2–SiC Composites Using Zirconium–Boron Reactive Filler Layers," *J. Am. Ceram. Soc.,* **94**[11] 3825-32 (2011).

[2]M. L. Shalz, B. J. Dalgleish, A. P. Tomsia, and A. M. Glaeser, "Ceramic joining," *J. Mater. Sci.,* **28**[6] 1673-84 (1993).

[3]M. Singh and R. Asthana, "Joining and integration of ZrB_2-based ultra-high temperature ceramic composites using advanced brazing technology," *J. Mater. Sci.,* **45**[16] 4308-20 (2010).

[4]W. G. Fahrenholtz, G. E. Hilmas, I. G. Talmy, and J. A. Zaykoski, "Refractory Diborides of Zirconium and Hafnium," *J. Am. Ceram. Soc.,* **90**[5] 1347-64 (2007).

[5]R. W. Rice, "Joining of Ceramics,*"* pp. 69-111 in Advances in joining technology: proceeding of the 4th Army Materials Technology Conference, Boston, MA, 1976.

[6]D. S. King, W. G. Fahrenholtz, and G. E. Hilmas, "Silicon carbide-titanium diboride ceramic composites " *J. Eur. Ceram. Soc.,* **33**[15-16] 2943-51 (2013).

[7]E. S. Machlin, pp. 263-88. in An Introduction to Aspects of Themodynamics and Kinetics Relevant to Materials Science**.** Elsevier, Oxford, UK, 2007.

[8]B. Basu, "Processing and Properties of Monolithic TiB_2 Based Materials," *Int. Mater. Rev.,* **51**[6] 352-74 (2006).

[9]C. C. Sorrell, H. R. Beratan, R. C. Bradt, and V. S. Stubican, "Directional Solidification of (Ti, Zr) Carbide-(Ti, Zr) Diboride Eutectics," *J. Am. Ceram. Soc.,* **67**[3] 190-94 (1984).

[10]W.-J. Li, R. Tu, and T. Goto, "Preparation of directionally solidified TiB_2–TiC eutectic composites by a floating zone method," *Mater. Lett.,* **60**[6] 839-43 (2006).

[11]E. Rudy and S. Windish, "Ternary Phase Equilibria in Transition Metal-Boron-Carbon-Silicon System: Part V. Compendium of Phase Diagram Data." in**.** Air Force Materials Laboratory, AFML-TR-65-2, Wright Patterson Air Force Base, OH, 1966.

[12]S. S. Ordan'yan, V. I. Unrod, and A. I. Avgustinik, "Reactions in the System TiC_x-TiB_2," *Sov. Powder Metall. Met. Ceram.,* **14**[9] 729-31 (1975).

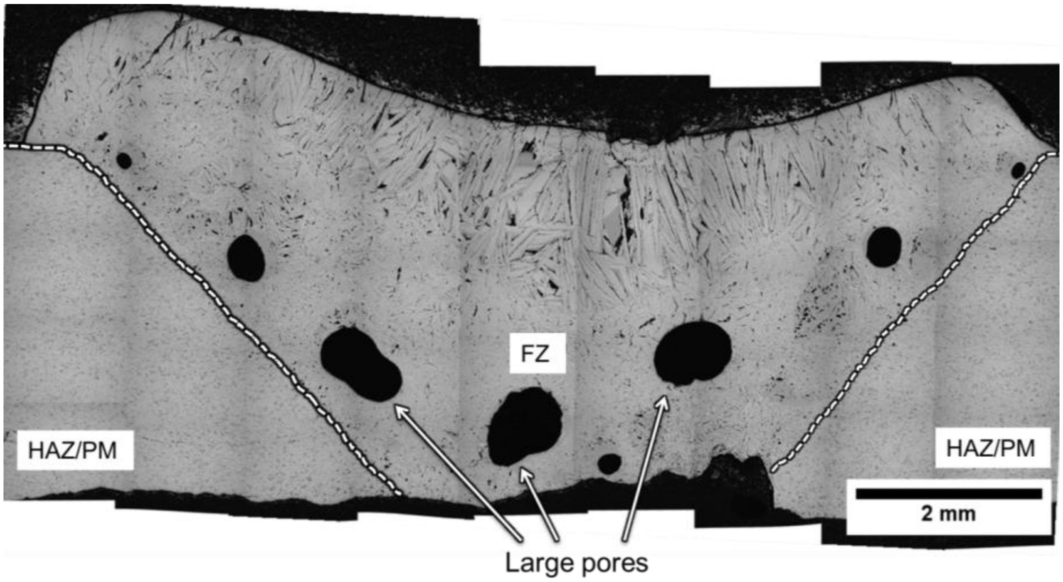

Figure 1: Cross section of a TiB_2-20TiC weldment showing directionally solidified TiB_2 grains (white) extending 1.9 mm into the FZ of a butt joint exhibiting full penetration. White arrows point to the large pores indicated at the bottom of the figure.

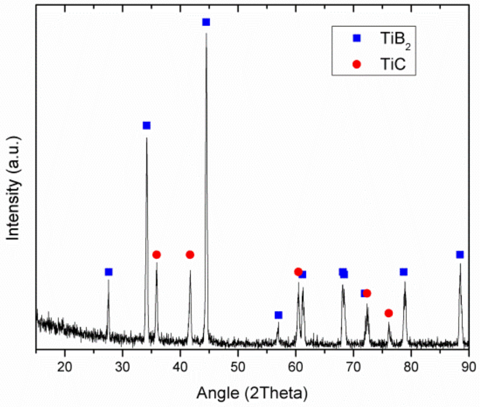

Figure 2: Grazing incidence XRD showing only TiB_2 and TiC present in the fusion zone.

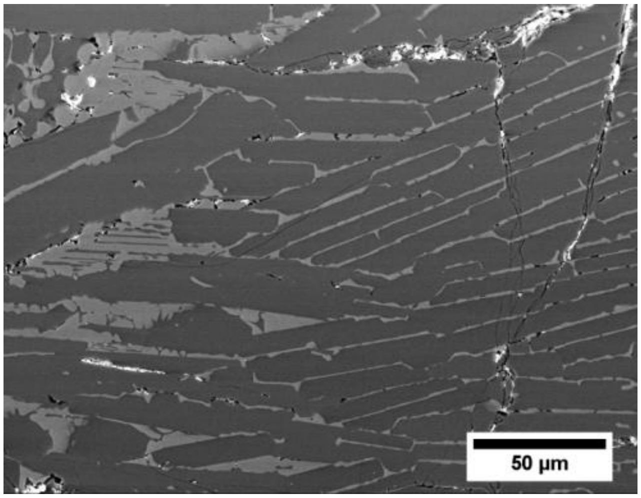

Figure 3: Backscatter electron image of a TiB_2–20TiC fusion zone. The light gray phase is TiC based on Z contrast.

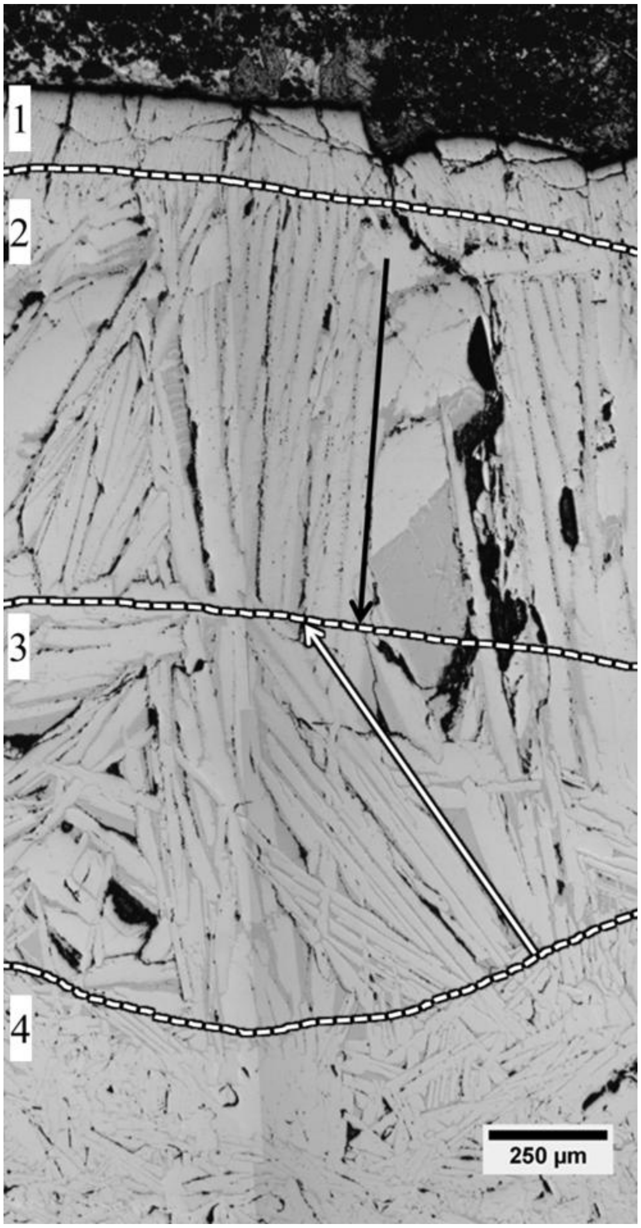

Figure 4: Directional growth of TiB_2 crystals (white) in Region 2 and Region 3 of the fusion zone. A black arrow highlights Region 2 TiB_2 crystal growth into the melt. A white arrow highlights the upward growth of Region 3 TiB_2 crystals. Dashed lines separate Regions 1 (top region) through 4 (bottom region).

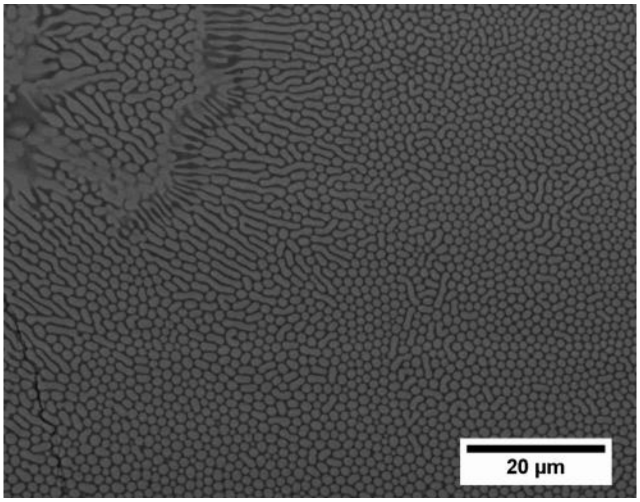

Figure 5: Backscatter electron image of cellular eutectic that has solidified, perpendicular to the cross-sectioning direction/parallel to the welding direction, in Region 2.

SECTION

3. SUMMARY AND CONCLUSIONS

The purpose of this dissertation was to investigate the fusion joining of UHTCs by plasma arc welding. A literature review on the joining of ceramics revealed that processes such as brazing and solid-state joining have received the most attention for the joining of ZrB_2 based ceramics. For example, glass and palladium brazes work well for the joining of ZrB_2-SiC ceramics, but braze melting temperatures limit the use temperature of joints. Solid-state joining techniques have been shown to exhibit properties consistent with the properties of the parent material, however the processing methods limit complex shape formation. Arc welding of ZrB_2 based ceramics was also previously demonstrated, but subsequent discussion on properties and microstructure was small, and the understanding of fusion welded UHTCs is still miniscule. In the work presented in this dissertation, ZrB_2 containing 20 vol% ZrC was produced for plasma arc welding studies. Plasma arc welding parameters were varied to study their effect on the solidified fusion zone. The mechanical properties of fusion zones were also analyzed to assess the usability of fusion welded UHTCs. Overall, this dissertation provides deeper insight into the fusion welding of UHTCs, and the first published reports on plasma arc welding of ZrB_2 based ceramics.

3.1 SUMMARY OF RESULTS

Questions were outlined in the Introduction of this dissertation. The summary will review the work presented in the manuscripts of this dissertation, and how it related to the questions set forth.

1. *Can plasma arc welding be used for the fusion welding of ZrB_2 based ceramics?*

Plasma and pulsed plasma arc welding processes (PAW and PPAW) were used to join dense ZrB_2-20ZrC ceramics. Three distinct fusion zone (FZ) shapes and microstructures were observed. PAW and PPAW FZs were observed to be binary FZs. ZrB_2 grains up to 1 mm in length in PAW FZs, with aspect ratios up to ~25:1. For PPAW binary FZs, ZrB_2 grains grew up to 0.8 mm in length, with aspect ratios up to ~40:1, revealing that the growth of ZrB_2, in length and width, was hindered by PPAW. In binary FZs, the composition of the ZrB_2-ZrC eutectic (43.2±6.1 vol% ZrC) agreed well with previously reported eutectic compositions (39 vol% ZrC). Starting a weld at the edge of the coupons allowed the melt pool to contact the underlying graphite disc, and C from the disc diffused into the melt pool. ZrB_2 grains in the PAW/C-rich were smaller than those in the binary welds, having an average maximum Feret diameter of 22.7±22.1 μm, and a maximum size of ~150 μm.

2. *What are the differences between plasma arc welded microstructures and the microstructure of the non-welded material?*

The grain size of ZrB_2 in the PM was 3.3±1.8 μm. EBSD was performed on the PM, and the crystallographic orientation of the PM was random. The differences between ZrB_2 grain sizes in each weldment were discussed in Question 1. FZ texture was analyzed by EBSD for three different weldments. Texture was observed throughout the FZ of a non-keyhole weld using the highest welding current (222A) with a plasma flow rate of 0.50 l/min, and a welding speed of 8 cm/min. These parameters were expected to have experienced the highest temperature. Texture was observed at a microstructural level for keyhole welds, with welding parameters of 176 A-1.00 l/min-8 cm/min, and 198 A-0.75 l/min-8 cm/min. ZrB_2 grains had a stacked appearance, where ZrC precipitated between ZrB_2 grains within a stack. Instead, it was determined, based on microstructural observations, that fast nucleation/growth of ZrB_2 desaturated B from the liquid weld pool, forcing ZrC to precipitate. As ZrC precipitated, ZrB_2 grains split and grew around the ZrC. Not all ZrC was trapped in ZrB_2 grains, and agreement with the reported eutectic composition revealed that ZrB_2 and ZrC within the eutectic solidified along an equilibrium path.

3. *How do ZrB_2 grains grow within the melt pool, and can grain growth be controlled?*

ZrB_2 grains at the surface of a FZ, made with welding parameters of 222 A-0.50 l/min-8 cm/min, were observed to grow up to 2 mm in length along the direction of the arc thermal gradient. EBSD revealed that the ZrB_2 grains grew along the basal plane, resulting in grains with a plate-like appearance. Examination of a free surface revealed ledge growth of ZrB_2. Varying PAW welding parameters affected ZrB_2 grain growth, where an increasing weld pool temperature led to increased growth of ZrB_2, i.e. larger ZrB_2 grains. PPAW hindered grain growth within the FZ. Similarly, the incorporation of a third phase, in PAW/C-rich FZs also hindered the growth of ZrB_2 during solidification.

4. *How do the strengths of welded ceramics compare to the base material?*

The four-point flexure strength of the PM was 656±79 MPa. The four-point flexure strength was subsequently measured for PAW, PAW/C-rich, and PPAW weldments. Flexure bars were machined from weldments, such that the surface of the FZ was the tensile surface of the flexure bar. The flexure strength of PAW welds was

143±34 MPa. Flexure strength increased for PPAW welds to 166±22 MPa. The highest flexure strength was observed for PAW/C-rich welds, 247±21 MPa. Griffith criteria was used to determine the critical flaws of the weldments. Critical flaw sizes were predicted to be ~400 μm for PAW welds, ~300 μm for PPAW welds, and ~140 μm for PAW/C-rich welds. The critical flaw size of PAW/C-rich weldments could not be determined, as the estimated sizes of scratch-like flaws, surface flaws, and volume flaws were all comparable to potential machining or observable microstructure flaws. For PAW welds, eutectic separation from ZrB_2 grains during cooling led to the formation of voids large enough to initiate failure. However, in PPAW welds, multiple fracture mirrors observed in a ZrB_2 grain indicated that link up of spontaneous or stress-induced microcracks likely initiated failure.

5. *Is arc welding a joining technique limited to ZrB_2 based ceramics?*

PAW of ZrC containing 20 vol% TiC (ZrC-20TiC), and TiB_2 containing 20 vol% TiC (TiB_2-20TiC) was accomplished. Porosity was observed at the edge of the FZ, where oblong pores were up to 0.9 mm in size along their longest axis. X-ray diffraction detected the presence of TiO (hongquiite) in the ZrC-20TiC PM, but not in the FZ, suggesting that pores in the FZ and HAZ of the ZrC-20TiC weldment possibly formed during active oxidation of the carbide. As with ZrB_2-20ZrC FZs, the TiB_2-20TiC FZ was a binary FZ. Exaggerated growth of TiB_2 grains was observed, where grains grew up to 1.2 mm in length. Analysis of the TiB_2-TiC eutectic composition (50 vol% TiC) agreed well with previously reported eutectic compositions.

3.2 CONCLUSIONS

The following conclusions were based on the manuscripts presented in this dissertation, and the preceding Summary section.

1. Plasma and pulsed plasma arc welding techniques can be used to fusion weld ZrB_2-20ZrC particulate ceramic composites. Several combinations of current, plasma flow rate, and welding speed can be used to alter the shape of the FZ width and the depth of penetration. For keyhole welds, increased arc power leads to an increase in the size of the weld pool. Increasing current led to larger arc spot sizes.
2. ZrB_2 in the PM had a random orientation and the microstructure of the PM was homogenous. In the FZ, increasing texture occurred with increasing weld pool temperature. In the PM, ZrC was homogenously distributed as a second phase. In the FZ, ZrC was contained in solidified eutectic, or trapped in large ZrB_2 grains, where ZrB_2 grains split and grew around nucleating ZrC.
3. ZrB_2 grew in the melt pool along the basal plane, forming platelet grains. Platelet orientation was determined by the largest thermal gradient acting on growing grains. Platelet thickness increased by ledge growth.
4. Separation of solidifying eutectic from ZrB_2 grains within the plasma arc welded fusion zone resulted in the formation of large voids within the FZ. These voids were determined to be failure origins for plasma arc welded ZrB_2-20ZrC. Void formation was not observed in pulsed plasma arc welded ceramics, but multiple fracture mirrors in a single ZrB_2 grain indicated stress-induced microcracking occurred in pulsed plasma arc welded FZs, leading to failure initiation. When voids were removed from the FZ, the effects of large ZrB_2 grain size controlled the mechanical behavior of the weldments.

5. Plasma arc welding was used to weld both ZrC-20TiC and TiB_2-20TiC ceramics. Porosity was observed in each FZ, indicating the need to refine PM processing and/or welding parameters. Welding of a carbide ceramic also revealed that ceramics with higher electrical resistivities than ZrB_2 can be arc welded, but at this point, the range of electrical resistivities that allow for arc welding is unknown.

Overall, the research presented in this dissertation expands the knowledge of ceramic fusion welding and provides a base for future work in the area. Analysis of the effect that welding parameters had on the formation and texture of the FZ, and discussion on the FZ microstructure and how it affects the mechanical properties surpasses that of the previous work on arc welding of ZrB_2 based ceramics. In future work, control of welding parameters and weld pool temperatures can be used to control the size, solidification behavior, and the resulting microstructure of FZs, leading to desired FZ properties.

Finally, it is recommended that research in PAW of ZrB_2-20ZrC ceramics expand upon the parameters of 176 A (current), 1 l/min (plasma flow rate), 12 cm/min (welding speed). This combination of parameters provides sufficient heat to form a FZ, but grain growth is hindered compared to higher welding currents, likely due to a combination of increased plasma flow rate and increased welding speed. To further refine microstructure, PPAW should be utilized, and an experimental matrix centering around the parameters presented in this research can assist in parameter refinement. Ultimately, a finer microstructure will improve the mechanical performance of ceramic weldments.

4. SUGGESTIONS FOR FUTURE WORK

Research presented in this dissertation has focused on the fusion welding of ultra-high temperature ceramics, but more work in the area of ceramic welding can be accomplished. This section presents several suggestions for future work that will advance the understanding of the behavior of ceramics during fusion welding.

1. The use of modeling will be useful in understanding the thermal gradients generated during the plasma arc welding process. Information on the temperature of a weld pool, and the thermal gradients surrounding the cooling liquid, can be combined with microstructural observations to describe the nucleation and growth behavior of the diboride in diboride-carbide weld pools. Modeling may then be used to optimize PAW parameters such that the FZ remains at a temperature conducive to high nucleation rates and low growth rates.
2. Pre-heating is necessary to successfully plasma arc weld diboride or carbide based ceramics. Without a pre-heat in excess of ~1300°C, thermal shock of the ceramic has been observed. Therefore, it is suggested that the thermal shock associated with arc welding be investigated.
3. PAW/C-rich FZs had smaller ZrB_2 grains than PAW or PPAW FZs. It was hypothesized that the introduction of C into the weld pool reduced the temperature of the weld pool as energy was expended during the dissolution of C from the graphite spacer. This occurs as the enthalpy of fusion (ΔH_f) and mixing (ΔH_{mix}) are expected to be positive for the system. In PAW/C-rich welds, the lower temperature of the weld pool promoted nucleation of ZrB_2, but hindered

growth. Addition of a filler material with known ΔH_f and ΔH_{mix} can be added to a weld pool during welding, could be used to confirm this hypothesis.

4. Large pores were observed in the FZ of ZrC-20TiC. Porosity was also observed in the HAZ of ZrC-20TiC and ZrB_2-20ZrC weldments. Currently, porosity formation is thought to occur during to active oxidation of the non-oxides. X-ray diffraction of the parent material revealed the presence of hongquiite, a cubic TiO, and the formation of these pores is thought to occur during oxidation of (Zr,Ti)C with TiO, producing CO/CO_2 gas. Oxygen impurities are present in the shield and plasma gas. The utilization of pure materials, powders and gasses, may restrict or eliminate pore formation in the FZ and HAZ.
5. The research presented in this dissertation revealed that PAW can be utilized for the fusion joining of ceramics, while previous work on the arc welding of ceramics utilized gas tungsten arc welding (GTAW) processes. Utilizing GTAW, the fusion welding of ceramics containing SiC and B_4C was demonstrated. Attempts at PAW of UHTCs containing SiC and B_4C have not been so successful, therefore, it is suggested that the research on fusion welding of ceramics by GTAW be expanded.

APPENDIX

A.1 UNPUBLISHED DATA

A.1.1 Inert Atmosphere Welding Chamber

A custom welding chamber consisting of a glovebox (MBraun; UNIlab ; Garching, Germany) modified with feedthroughs for a graphite element furnace (Figure A1) for pre-heating, cooling water for the furnace, a welding ground, power and gas for a plasma arc welding torch (Victor Technologies; Thermal Arc; PWM 300; St. Louis, MO), and electrical power. The glovebox was set to maintain argon between 100 and 450 Pa (1.0 and 4.5 mbar) over atmospheric pressure. A Thermal Arc® plasma arc welding system consisting of a coolant circulator (HE100A), power supply (ArcMaster 300S), welding console (WC-100B), weld sequencer (WC-1), and plasma arc welding torch was utilized for welding. The pre-heat furnace consisted of a graphite box with nominal inner dimensions of 12.7 cm by 12.7 cm by 5.1 cm, the graphite element, and removable top plate to serve as the welding ground. The furnace was surrounded by ~22.0 mm of graphite felt and ~6.4 cm of refractory. Temperature was monitored using a type B thermocouple. To control welding speed, the welding torch was attached to a torch track (ESAB; Model ; Gothenburg, Sweden) that allowed for variable welding speeds. The entire inert welding chamber is pictured in Figure A2.

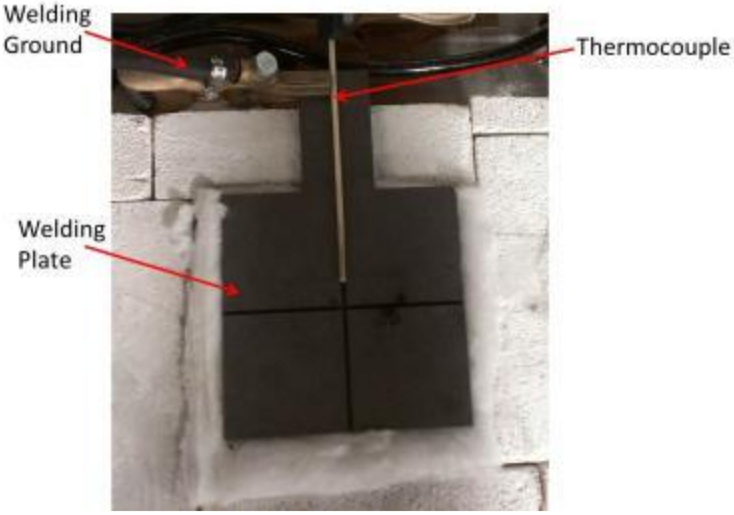

Figure A1: Covered welding furnace. The welding plate serves as contact with the specimen and ground. A graphite element under the welding plate heats the welding plate and specimens. A type-B thermocouple measures temperature.

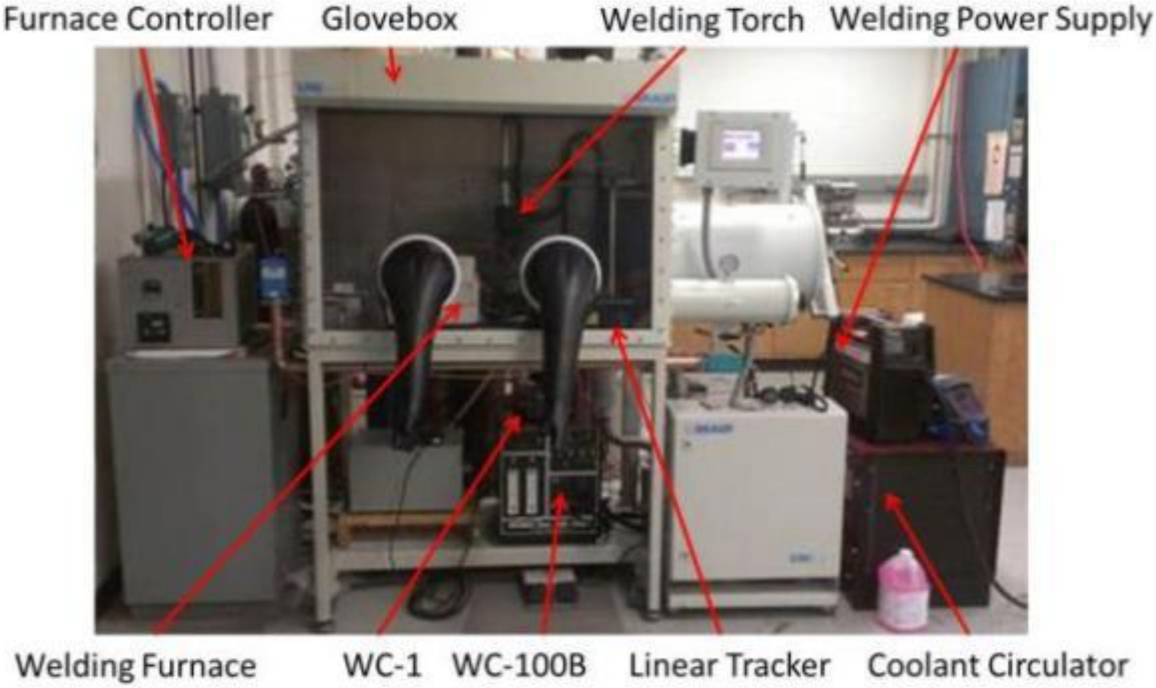

Figure A2: Welding chamber and equipment necessary for PAW of UHTCs.

A.1.2 Factorial Analysis of PAW Welding Parameters

PAW welding parameters were optimized for ZrB_2-20ZrC using a 3^3 factorial. The welding current, plasma flow rate, and welding speed were investigated. Table A1 includes the values of each parameter that were investigated. Weldments were given scores based on the density and penetration depth of the FZ. The scores were analyzed for interactions, using an ANOVA (analysis of variance) general linear model in Minitab, to determine which welding parameters produced the optimal weldments.

A total of 14 parameter combinations from the 3^3 factorial were observed to produce successful welds. With no replications of the experiment, an error term could not be calculated, therefore, it is assumed that no three-factor interactions occured. For analysis of two-factor interactions, the null hypothesis of the factorial was assumed that no significant interaction occurred between the factors. Testing for two-factor interactions with a significance level of 0.05, resulted in a failure to reject the null hypothesis, leading to the conclusion that there were no two-factor interactions. As no two-factor interactions were observed, the main effects of each parameter were calculated, where the null hypothesis was that each factor had no significant effect on the final weldment score. Using a significance level of 0.05, testing of main the effects revealed that the welding current and plasma flow rate had a significant effect on the formation of weldments. At a significance level of 0.1, welding speed had a significant effect on the formation of weldments. Therefore, it was concluded, with 90% confidence, each factor had an effect on the formation of welds in the ZrB_2-20ZrC system. Main effects plots are shown in Figure A3, where increasing current and plasma flow rate were observed to have a positive effect on the mean weldment score, while increasing speed was observed to have a negative effect on the mean weldment score.

The highest weldment score of 9.92 was selected as the set of optimal welding parameters for future work, where the current was 198 A, plasma flow rate was 0.75 l/min, and the welding speed was 8 cm/min.

Table A1: 3^3 Factorial Parameters and Final Weldment Scores

Welding Current (A)	**Plasma Flow Rate (l/min)**	**Welding Speed (cm/min)**	**Score**	**Porosity in FZ**
176	0.50	8	0.00	-
198	0.50	8	6.51	yes
222	0.50	8	3.89	yes
176	0.75	8	8.44	yes
198	0.75	8	9.92	no
222	0.75	8	9.41	no
176	1.00	8	4.29	yes
198	1.00	8	6.43	yes
222	1.00	8	8.41	yes
176	0.50	12	0.00	-
198	0.50	12	0.00	-
222	0.50	12	0.00	-
176	0.75	12	0.00	-
198	0.75	12	9.42	no
222	0.75	12	9.49	no
176	1.00	12	0.00	-
198	1.00	12	9.02	yes
222	1.00	12	9.94	no
176	0.50	16	0.00	-
198	0.50	16	0.00	-
222	0.50	16	0.00	-
176	0.75	16	0.00	-
198	0.75	16	9.08	yes
222	0.75	16	0.00	-
176	1.00	16	0.00	-
198	1.00	16	0.00	-
222	1.00	16	9.45	no
Perfect Score			13.96	

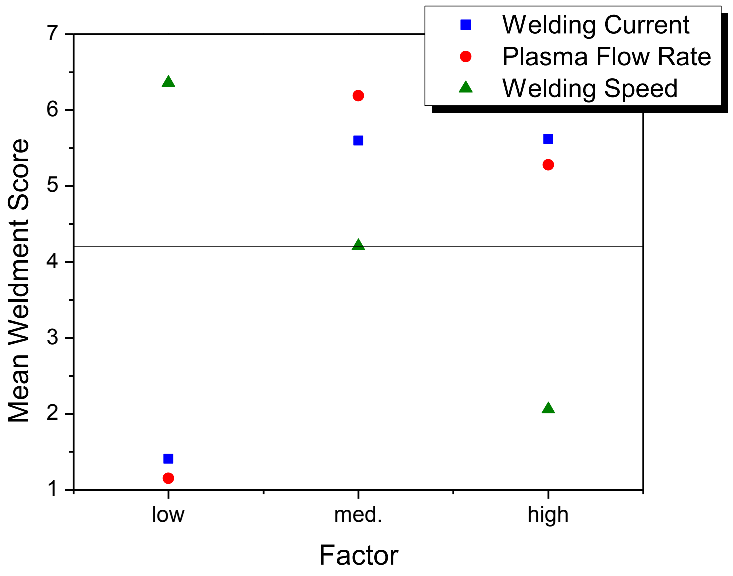

Figure A3: Plotted 3^3 factorial weldment scores, where the effects of welding current, plasma flow rate, and welding speed were analyzed for their effect on PAW of ZrB_2-20ZrC.

A second optimization experiment, a 3^2 factorial, was used to analyze the effect of pre-heat temperature and arc ramp-up rates on welding of ZrB_2-20ZrC. The three levels of pre-heat temperature tested were 1250, 1450, and 1650°C. Arc ramp-up rates were tested at levels of 15, 20, and 25 A/s. Welding current, plasma flow rate, and welding speed were kept constant at 198 A, 0.75 l/min, and 8 cm/min for each of the nine 3^2 experiments. The scores for all 9 weldments were analyzed for two and single factor interactions, using an ANOVA (analysis of variance) general linear model in Minitab, to determine which pre-heat temperature and arc ramp-up rates produced optimal weldments. It was observed that the pre-heat temperature and arc ramp up rates did not interact, or have a significant effect on the weldment score (Figure A4), therefore, pre-heat temperature and arc ramp up rate were determined to not significantly affect the ability to successfully weld ZrB_2-20ZrC when using the values that were examined.

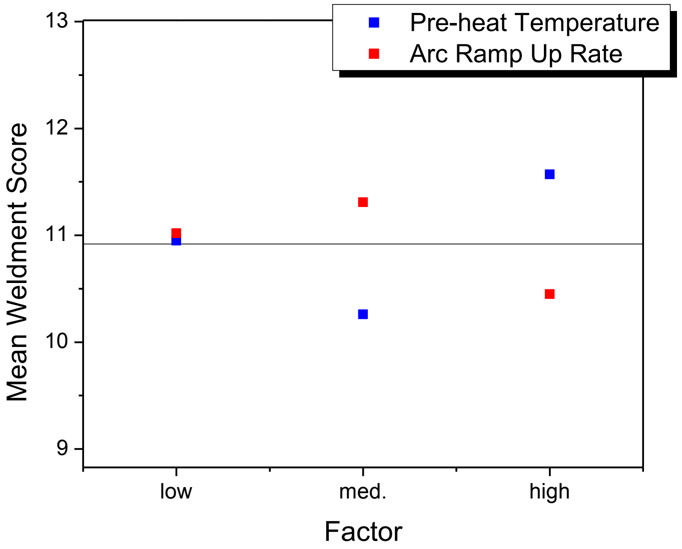

Figure A4: Plotted 2^3 factorial weldment scores, where the effects of pre-heat temperature and arc ramp rate were analyzed for their effect on PAW of ZrB_2-20ZrC.

A.1.3 Pulsed Plasma Arc Welding of ZrB_2-ZrC-WC

PAW of ZrB_2-20ZrC and TiB_2-20TiC were demonstrated, but it was observed that the diboride exhibited exaggerated growth (grains up to 1 mm in length in one direction). Analysis of ZrB_2-ZrC PAW welding procedures also revealed that the growth of ZrB_2 could be controlled. Two methods were observed. The first method was the incorporation of a third phase that may alter solidification. The second method was the use of PPAW, where controlled pulses provided the necessary heat to melt the PM at peak currents. To expand on both methods on the control of ZrB_2 during weld pool solidification, PPAW was used to weld a ZrB_2 containing 25 vol% ZrC and 10 vol% WC (ZrB_2-25ZrC-10WC). Three FZs were analyzed. The first weldment was welded using a peak current of 260 A and a background of 57%. Pulse times were 0.1s at peak and 0.3s at background. The plasma flow rate was 1 l/min, and the welding speed was 12 cm/min. The second ZrB_2-ZrC-WC weldment was welded using a peak current of 230 A and a background of 57%. Pulse times, plasma flow rate, and welding speed were the same as the first weld. The third ZrB_2-ZrC-WC weldment was welded using a peak current of 230 A and a background of 50%. Pulse times were 0.1s at peak current and 0.4s at background current. Plasma flow rate and welding speed were the same as the first two welds. Representative microstructures for each weld are presented in Figure A.3.

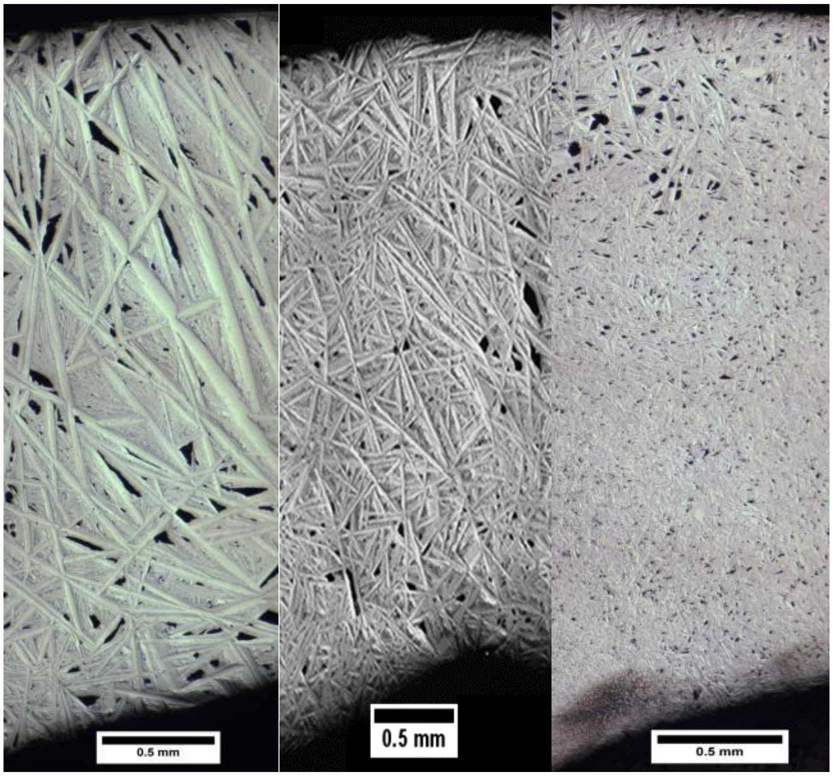

Figure A5: ZrB_2-ZrC-WC PPAW fusion zones, where power input into the weld decreases from left to right. Far left, power input of 2637 J/mm. Middle, power input of 2333 J/mm. Far right, power input of 2066 J/mm.

The heat input for each of the three welds was calculated and heat input was observed to decrease from weld 1 to weld 3. Dividing the heat input by the welding speed gives the linear energy input in J/mm. The total linear energy input for weld 1 was 2637 J/mm, for weld 2 2333 J/mm, and for weld 3 2066 J/mm. The length of ZrB_2 grains was also observed to decrease with decreasing linear energy input, where ZrB_2 grains in weld 1 grew to lengths of 2.3 mm and ZrB_2 grains in weld 3 grew to lengths of 0.66 mm, a reduction of ~71% for the observed maximum in ZrB_2 grain length. Therefore, decreasing the linear energy input hindered the growth of ZrB_2 grains in ZrB_2-25ZrC-10WC FZs.

A.1.4 Tungsten filler additions

Tungsten filler (W wire) was added to the PAW FZ of ZrB_2-20ZrC. Filler was added to the FZ by feeding wire into the molten ZrB_2-ZrC weld pool just behind the plasma arc. W filler was added using a welding current of 200 A, 1 l/min plasma flow rate, and a welding speed of 8 cm/min. In the FZ (Figure A6), ZrB_2 grains were observed to grow up to lengths >1 mm with aspect ratios ranging from ~10:1 to ~45:1. The observed grain sizes were similar to that of ZrB_2 in PAW welds, with aspect ratios similar to both PAW and PPAW techniques. At a higher welding current and plasma flow rate, the incorporation of W as a filler may have affected ZrB_2 grain growth, but an in-depth analysis of filler materials and their effect on FZ solidification is required.

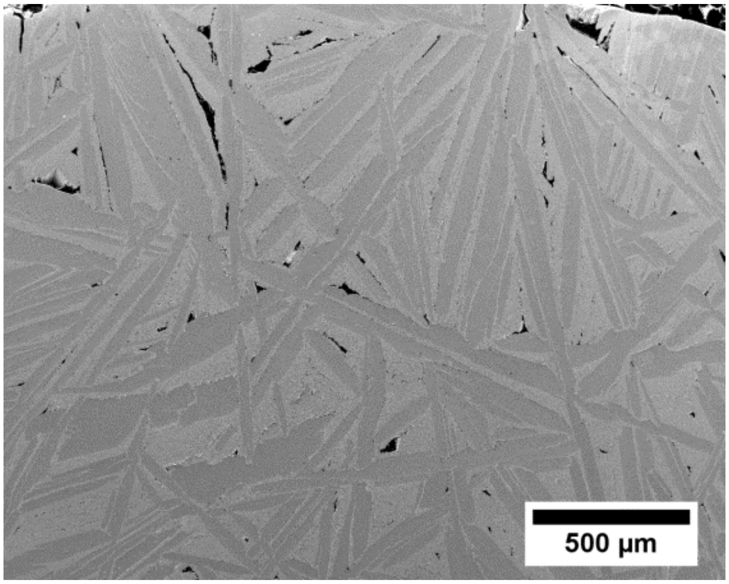

Figure A6: FZ of a ZrB_2-20ZrC FZ, where W was utilized as a filler material.

A.1.5 Gas Tungsten Arc Welding of TiB_2-TiC-B_4C

The PAW of a three phase PM was attempted through the PAW of ZrB_2-ZrC-B_4C and TiB_2-TiC-B_4C ceramics. However, during welding loss of B_4C occurred, and the final FZ microstructure consisted of only ZrB_2-ZrC or TiB_2-TiC. Due to the penetration of the plasma jet into the weld pool, it is possible that oxidation of B_4C occurs during PAW of the three phase material. It should be noted that the argon gas utilized for a plasma gas did contain some percentage of oxygen impurities, therefore, oxidation of B_4C could occur even in the inert (typically <100 ppm O_2) environment of the glovebox. To determine if a diboride-carbide containing B_4C could be fusion welded, TiB_2-TiC-B_4C was welded with GTAW (gas tungsten arc welding) in an argon bucket. When compared to PAW, GTAW does not produce a plasma jet that penetrates the weld pool, therefore, the melt pool is not exposed to oxygen unless the welding environment contains oxygen. Welding was not performed in the glovebox, therefore, to reduce oxygen within the bucket, the bucket was flooded with argon for a period of 15 minutes. The argon flow into the bucket was continued during welding. Welding was performed by arcing to a graphite pillar which the specimens sat on. Radiative heating of the specimen from the arc was enough to pre-heat the specimens to a sufficient temperature to prevent thermal shock. Welding with a current of ~225 A, two specimens were butt welded using GTAW. After welding, the specimen was allowed to cool naturally to room temperature. The specimen was slightly glassy on the surface after welding, indicating that some oxidation of the specimen occurred.

SEM image analysis of the FZ revealed a finer microstructure, similar to that of PAW C-rich. Figure A7 presents a low magnification view of the FZ, where exaggerated growth similar to PAW of ZrB_2-20ZrC and TiB_2-20TiC, or PPAW of ZrB_2-20ZrC was not observed. Pores were observed at the HAZ/FZ interface, which may have formed due to oxidation of the weld pool. Figure A8, a higher magnification image of the FZ, reveals the presence of two phases, a light grey phase, and a black phase. At the present time, it is unclear what the two phases are, or if a third phase is present, but not visible due to contract differences. However, it can be said that TiC has been observed to appear as a brighter phase than TiB_2 in SEM, due to Z contrast. Similarly, a low molecular weight compound, such as B_4C would appear very dark compared to TiC or TiB_2. Regardless of the phases present, the GTAW FZ re-enforces the idea that GTAW can be utilized for the fusion joining of UHTCs.

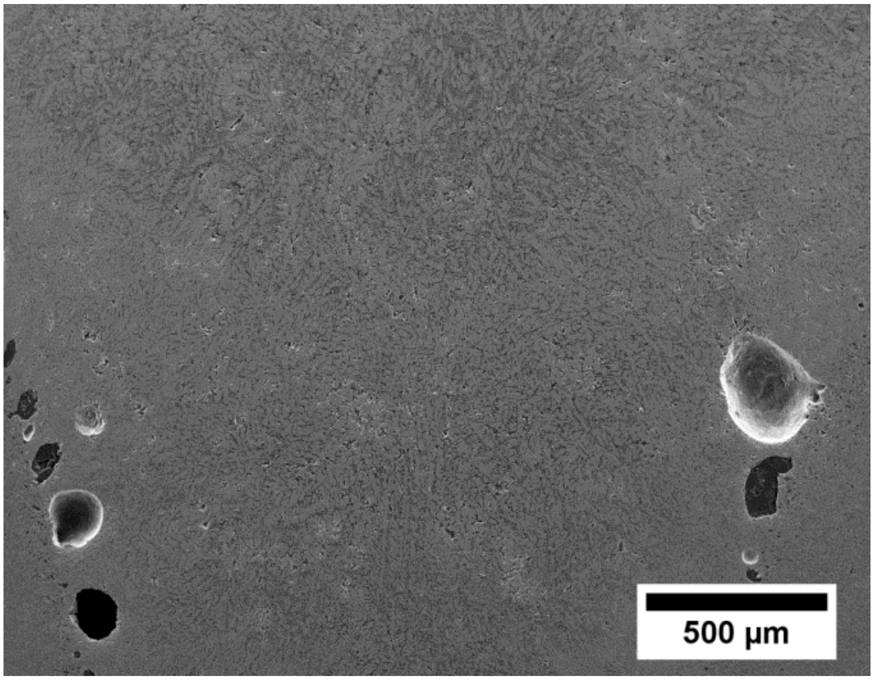

Figure A7: FZ of a TiB2-TiC-B4C weldment revealing a finer microstructure than PAW fusion joining methods. Porosity was observed at the HAZ/FZ interface.

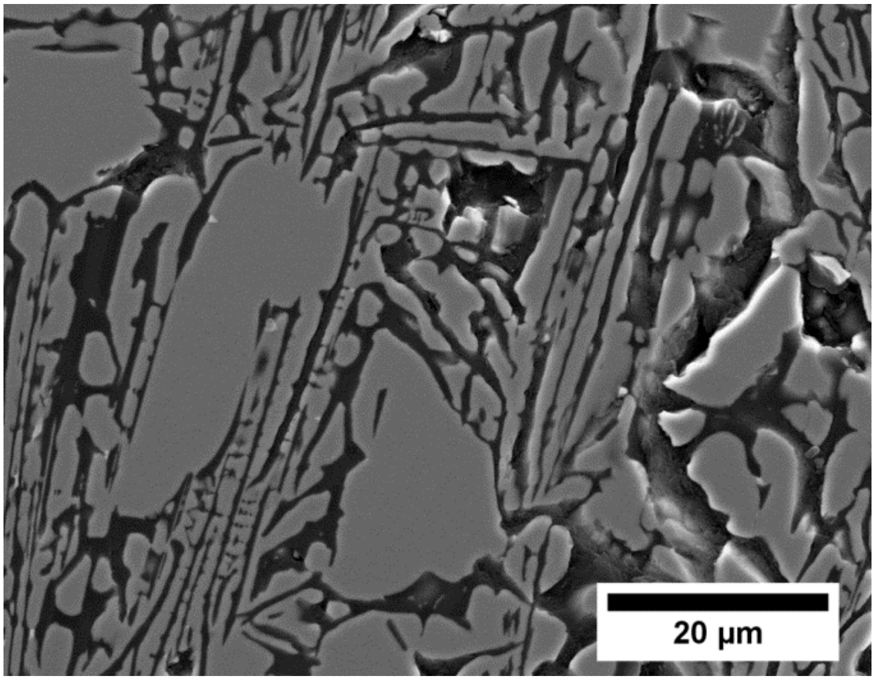

Figure A8: Higher magnification image where a phase with a high Z contrast and a phase with a low Z contrast were observed.

REFERENCES

[1]W. G. Fahrenholtz, G. E. Hilmas, I. G. Talmy, and J. A. Zaykoski, "Refractory Diborides of Zirconium and Hafnium," *J. Am. Ceram. Soc.,* **90**[5] 1347-64 (2007).

[2]E. Rudy and S. Windish, "Ternary Phase Equilibria in Transition Metal-Boron-Carbon-Silicon System: Part V. Compendium of Phase Diagram Data." in**.** Air Force Materials Laboratory, AFML-TR-65-2, Wright Patterson Air Force Base, OH, 1966.

[3]L. Zhang, D. A. Pejaković, J. Marschall, and M. Gasch, "Thermal and Electrical Transport Properties of Spark Plasma-Sintered HfB_2 and ZrB_2 Ceramics," *J. Am. Ceram. Soc.,* **94**[8] 2562-70 (2011).

[4]G.-J. Zhang, Z.-Y. Deng, N. Kondo, J.-F. Yang, and T. Ohji, "Reactive Hot Pressing of ZrB_2–SiC Composites," *J. Am. Ceram. Soc.,* **83**[9] 2330-32 (2000).

[5]D. Sciti, L. Silvestroni, G. Celotti, C. Melandri, and S. Guicciardi, "Sintering and Mechanical Properties of ZrB_2–$TaSi_2$ and HfB_2–$TaSi_2$ Ceramic Composites," *J. Am. Ceram. Soc.,* **91**[10] 3285-91 (2008).

[6]A. L. Chamberlain, W. G. Fahrenholtz, G. E. Hilmas, and D. T. Ellerby, "High-Strength Zirconium Diboride-Based Ceramics," *J. Am. Ceram. Soc.,* **87**[6] 1170-72 (2004).

[7]M. Singh and R. Asthana, "Joining and integration of ZrB_2-based ultra-high temperature ceramic composites using advanced brazing technology," *J. Mater. Sci.,* **45**[16] 4308-20 (2010).

[8]W. R. Pinc, M. Di Prima, L. S. Walker, Z. N. Wing, and E. L. Corral, "Spark Plasma Joining of ZrB_2–SiC Composites Using Zirconium–Boron Reactive Filler Layers," *J. Am. Ceram. Soc.,* **94**[11] 3825-32 (2011).

[9]R. Asthana, M. Singh, and N. Sobczak, "Wetting behavior and interfacial microstructure of palladium- and silver-based braze alloys with C–C and SiC–SiC composites," *J. Mater. Sci.,* **45**[16] 4276-90 (2010).

[10]R. W. Rice, "Joining of Ceramics," pp. 69-111 in Advances in joining technology: proceeding of the 4th Army Materials Technology Conference, Boston, MA, 1976.

[11]G. E. Hilmas, W. G. Fahrenholtz, J. L. Watts, and H. J. Brown-Shaklee, "Ceramic welds, and a method for producing the same," U.S. Patent 8,715,803, (2014).

[12]R. Lofting, "Welding." Crowood Press: Marlborough, Wiltshire, UK, (2013).

[13]N. Kahraman, "The influence of welding parameters on the joint strength of resistance spot-welded titanium sheets," *Materials & Design,* **28**[2] 420-27 (2007).

[14]S. D. Meshram, T. Mohandas, and G. M. Reddy, "Friction welding of dissimilar pure metals," *Journal of Materials Processing Technology,* **184**[1–3] 330-37 (2007).

[15]G. Liu, L. E. Murr, C. S. Niou, J. C. McClure, and F. R. Vega, "Microstructural aspects of the friction-stir welding of 6061-T6 aluminum," *Scr. Mater.,* **37**[3] 355-61 (1997).

[16]F. Meschke, U. Kayser, and A. Rendtel, "Process for the Low-Deformation Diffusion Welding of Ceramic Components." in, **Vol. US 8,087,567 B2.** Edited by U. S. P. Office. ESK Ceramics GmbH & Co., KG, United States, 2012.

[17]L. M. Nguyen, D. Leguillon, O. Gillia, and E. Riviere, "Bond failure of a SiC/SiC brazed assembly," *Mechanics of Materials,* **50**[0] 1-8 (2012).

[18]M. Singh, T. Matsunaga, H.-T. Lin, R. Asthana, and T. Ishikawa, "Microstructure and mechanical properties of joints in sintered SiC fiber-bonded ceramics brazed with Ag–Cu–Ti alloy," *Materials Science and Engineering: A,* **557**[0] 69-76 (2012).

[19]M. Singh, "Joining of sintered silicon carbide ceramics for high-temperature applications," *J. Mater. Sci. Lett.,* **17**[6] 459-61 (1998).

[20]J. Janczak-Rusch, D. Piazza, and A. R. Boccaccini, "Joining of SiC fibre reinforced borosilicate glass matrix composites to molybdenum by metal and silicate brazing," *J. Mater. Sci.,* **40**[14] 3693-701 (2005).

[21]F. Smeacetto, M. Salvo, M. Ferraris, J. Cho, and A. R. Boccaccini, "Glass–ceramic seal to join Crofer 22 APU alloy to YSZ ceramic in planar SOFCs," *J. Eur. Ceram. Soc.,* **28**[1] 61-68 (2008).

[22]M. G. Nicholas and D. A. Mortimer, "Ceramic/metal joining for structural applications," *Mater. Sci. Technol.,* **1**[9] 657-65 (1985).

[23]T. Yano, H. Suematsu, and T. Iseki, "High-resolution electron microscopy of a SiC/SiC joint brazed by a Ag-Cu-Ti alloy," *J. Mater. Sci.,* **23**[9] 3362-66 (1988).

[24]T. J. Moore, "Feasibility Study of the Welding of SiC," *J. Am. Ceram. Soc.,* **68**[6] C-151-C-51 (1985).

[25]E. F. C. Cain and W. T. McFarlen, "Compliant interface for ceramic turbine blades," U.S. Patent 4,417,854, (1983).

[26]M. C. Hemsworth, R. J. Corsmeier, and A. A. Hauser, "Ceramic turbine shroud assembly," U.S. Patent 4,087,199, (1978).

[27]S. M. Widrig, J. Morrison, H. A. Albrecht, Y. Shteyman, and S. C. Butner, "Ceramic matrix composite turbine vane," U.S. Patent 6,648,597, (2003).

[28]A. Rossmann and W. Hoffmuller, "Method and means for retaining ceramic turbine blades," U.S. Patent 3,784,320, (1974).

[29]H. Brobeck, "Improved connection structure for joining ceramic and metallic parts of a turbine shaft," U.S. Patent 4,424,003, (1984).

[30]M. Singh and R. Asthana, "Joining of ZrB_2-Based Ultra-High-Temperature Ceramic Composites to Cu–Clad–Molybdenum for Advanced Aerospace Applications," *Int. J. Appl. Ceram. Technol.*, **6**[2] 113-33 (2009).

[31]R. Asthana and M. Singh, "Joining of ZrB_2-based ultra-high-temperature ceramic composites using Pd-based braze alloys," *Scr. Mater.*, **61**[3] 257-60 (2009).

[32]N. L. Okamoto, M. Kusakari, K. Tanaka, H. Inui, and S. Otani, "Anisotropic elastic constants and thermal expansivities in monocrystal CrB_2, TiB_2, and ZrB_2," *Acta Mater.*, **58**[1] 76-84 (2010).

[33]Z. Li and R. C. Bradt, "Thermal Expansion and Thermal Expansion Anisotropy of SiC Polytypes," *J. Am. Ceram. Soc.*, **70**[7] 445-48 (1987).

[34]D. J. Green, P. Z. Cai, and G. L. Messing, "Residual stresses in alumina–zirconia laminates," *J. Eur. Ceram. Soc.*, **19**[13–14] 2511-17 (1999).

[35]H. M. Chan, "LAYERED CERAMICS: Processing and Mechnical Behavior," *Annu. Rev. Mat. Sci.*, **27** 249-82 (1997).

[36]O. Sbaizero and E. Lucchini, "Influence of residual stresses on the mechanical properties of a layered ceramic composite," *J. Eur. Ceram. Soc.*, **16**[8] 813-18 (1996).

[37]R. Bermejo and R. Danzer, "High failure resistance layered ceramics using crack bifurcation and interface delamination as reinforcement mechanisms," *Engineering Fracture Mechanics*, **77**[11] 2126-35 (2010).

[38]L. Esposito and A. Bellosi, "Joining ZrB_2-SiC composites using glass interlayers," *J. Mater. Sci.*, **40**[17] 4445-53 (2005).

[39]T. Okuni, Y. Miyamoto, H. Abe, and M. Naito, "Joining of silicon carbide and graphite by spark plasma sintering," *Ceram. Int.*, **40**[1, Part B] 1359-63 (2014).

[40]S. Grasso, P. Tatarko, S. Rizzo, H. Porwal, C. Hu, Y. Katoh, M. Salvo, M. J. Reece, and M. Ferraris, "Joining of β-SiC by spark plasma sintering," *J. Eur. Ceram. Soc.*, **34**[7] 1681-86 (2014).

[41]S. Rizzo, S. Grasso, M. Salvo, V. Casalegno, M. J. Reece, and M. Ferraris, "Joining of C/SiC composites by spark plasma sintering technique," *J. Eur. Ceram. Soc.,* **34**[4] 903-13 (2014).

[42]T. Okuni, Y. Miyamoto, H. Abe, and M. Naito, "Joining of AlN and graphite disks using interlayer tapes by spark plasma sintering," *Materials & Design,* **54**[0] 755-59 (2014).

[43]R. A. Alliegro, L. B. Coffin, and J. R. Tinklepaugh, "Pressure-Sintered Silicon Carbide," *J. Am. Ceram. Soc.,* **39**[11] (1956).

[44]S. C. Zhang, G. E. Hilmas, and W. G. Fahrenholtz, "Mechanical properties of sintered ZrB_2–SiC ceramics," *J. Eur. Ceram. Soc.,* **31**[5] 893-901 (2011).

[45]D. Sciti, F. Monteverde, S. Guicciardi, G. Pezzotti, and A. Bellosi, "Microstructure and mechanical properties of ZrB_2–$MoSi_2$ ceramic composites produced by different sintering techniques," *Materials Science and Engineering: A,* **434**[1–2] 303-09 (2006).

[46]F. Monteverde, C. Melandri, and S. Guicciardi, "Microstructure and mechanical properties of an HfB_2 vol.% SiC composite consolidated by spark plasma sintering," *Mater. Chem. Phys.,* **100**[2–3] 513-19 (2006).

[47]G. N. Mikhailova, B. P. Mikhailov, and A. V. Troitskii, "Laser welding of HTSC ceramics," *Laser Physics Letters,* **1**[10] 525-27 (2004).

[48]M. Ikeda, "Ceramics Welding with Laser," *Taikabutsu Overseas,* **5**[3] 27-33 (1985).

[49]J. F. Li, L. Li, and F. H. Stott, "Thermal stresses and their implication on cracking during laser melting of ceramic materials," *Acta Mater.,* **52**[14] 4385-98 (2004).

[50]L. Bradley, L. Li, and F. H. Stott, "Flame-assisted laser surface treatment of refractory materials for crack-free densification," *Materials Science and Engineering: A,* **278**[1–2] 204-12 (2000).

[51]V. A. Burdovitsin, A. S. Klimov, and E. M. Oks, "On the possibility of electron-beam processing of dielectrics using a forevacuum plasma electron source," *Technical Physics Letters,* **35**[6] 511-13 (2009).

[52]V. A. Burdovitsin, A. S. Klimov, A. V. Medovnik, and E. M. Oks, "Electron beam treatment of non-conducting materials by a fore-pump-pressure plasma-cathode electron beam source," *Plasma Sources Science and Technology,* **19**[5] 055003 (2010).

[53]J. C. Metcalfe and M. B. C. Quigley, "Heat transfer in plasma-arc welding," *Welding Journal,* **54**[3] 99-103 (1975).

[54]V. A. Mukhanov, P. S. Sokolov, and V. L. Solozhenko, "On melting of B_4C boron carbide under pressure," *J. Superhard Mater.,* **34**[3] 211-13 (2012).

[55]S. S. Ordan'yan, A. I. Dmitriev, E. K. Stepanenko, N. Y. Aulova, and N. E. Semenov, "SiC-TiB_2 system - A base of high-hardness wear-resistant materials," *Powder Metallurgy and Metal Ceramics,* **26**[5] 375-77 (1987).

[56]J.-D. Hong, K. E. Spear, and V. S. Stubican, "Directional solidification of SiC-B_4C eutectic: Growth and some properties," *Mater. Res. Bull.,* **14**[6] 775-83 (1979).

[57]R. Tu, H. Hirayama, and T. Goto, "Preparation of ZrB_2-SiC Composites by Arc Melting and Their Properties," *J. Ceram. Soc. Jpn.,* **116**[3] 431-35 (2008).

[58]Z. Liu, C. S. Wu, and J. Gao, "Vision-based observation of keyhole geometry in plasma arc welding," *International Journal of Thermal Sciences,* **63**[0] 38-45 (2013).

[59]C. S. Wu, C. B. Jia, and M. A. Chen, "A Control System for Keyhole Plasma Arc Welding of Stainless Steel Plates with Medium Thickness," *Supplement to the Welding Journal,* **89** 225-31 (2010).

[60]Y. Arata and H. Maruo, "Magnetic Control of Plasma Arc Welding," *Transactions of JWRI,* **1**[1] 1-9 (1972).

[61]D. M. Evans, D. Huang, J. C. McClure, and A. C. Nunes, "Arc Efficiency of Plasma Arc Welding," *Welding Journal,* **77**[2] 53-8 (1998).

[62]W. G. Essers and R. Walter, "Heat Transfer and Penetration Mechanisms with GMA and Plasma-GMA Welding," *Welding Journal,* **60**[2] 37-42 (1981).

[63]M. B. C. Quigley, P. H. Richards, D. T. Swift-Hook, and A. E. F. Gick, "Heat flow to the workpiece from a TIG welding arc," *J. Phys. D: Appl. Phys.*, **6**[18] 2250 (1973).

[64]N. Christensen, V. d. L. Davies, and K. Gjermundsen, "Distribution of temperatures in arc welding," *British Welding Journal,* **12**[2] 54-75 (1965).

[65]W. D. Kingery, H. K. Bowen, and D. R. Uhlmann, "Introduction to Ceramics," Second ed. John Wiley & Sons: New York, NY, (1975).

[66]J. W. Evans and L. C. De Jonghe, "The Production and Processing of Inorganic Materials." The Minerals, Metals & Materials Society: Warrendale, PA, (2002).

[67]J. E. Shelby, "Introduction to Glass Science and Technology," Second ed. The Royal Society of Chemistry: Cambridge, UK, (2005).

[68]D. A. Porter and K. E. Easterling, "Phase Transformations in Metals and Alloys," Second ed. Chapman & Hill: London, UK, (1992).

[69] G. J. Shiflet, M. A. Mangan, and W. G. Meng, "Growth by Ledges," *Interface Science,* **6**[1-2] 133-54 (1998).

[70] S. A. David, J. M. Vitek, M. Rappaz, and L. A. Boatner, "Microstructure of stainless steel single-crystal electron beam welds," *MTA*, **21**[6] 1753-66 (1990).

[71] J. I. Goldstein, D. E. Newbury, P. Echlin, D. C. Joy, C. E. Lyman, E. Lifshin, L. Sawyer, and J. R. Michael, "Scanning Electron Microscopy and X-Ray Microanalysis," Third ed. Springer: New York, NY, (2003).

[72] A. J. Schwartz, M. Kumar, and B. L. Adams, "Electron Backscatter Diffraction in Materials Science." Kluwer Academic: New York, NY, (2000).

[73] S. H. Wu, J. C. Huang, and Y. N. Wang, "Evolution of microstructure and texture in Mg-Al-Zn alloys during electron-beam and gas tungsten arc welding," *Metall and Mat Trans A*, **35**[8] 2455-69 (2004).

[74] J. Kell, J. R. Tyrer, R. L. Higginson, and R. C. Thomson, "Microstructural characterization of autogenous laser welds on 316L stainless steel using EBSD and EDS," *Journal of Microscopy,* **217**[2] 167-73 (2005).

[75] R. W. Fonda, J. F. Bingert, and K. J. Colligan, "Development of grain structure during friction stir welding," *Scr. Mater.*, **51**[3] 243-48 (2004).

[76] J. Unfried S, C. M. Garzón, and J. E. Giraldo, "Numerical and experimental analysis of microstructure evolution during arc welding in armor plate steels," *Journal of Materials Processing Technology*, **209**[4] 1688-700 (2009).

[77] S. F. Su, H. K. Lin, J. C. Huang, and N. J. Ho, "Electron-beam welding behavior in Mg-Al-based alloys," *Metall and Mat Trans A,* **33**[5] 1461-73 (2002).

[78] S. A. David, S. S. Babu, and J. M. Vitek, "Welding: Solidification and microstructure," *JOM,* **55**[6] 14-20 (2003).

[79] P. Vajeeston, P. Ravindran, C. Ravi, and R. Asokamani, "Electronic structure, bonding, and ground-state properties of AlB_2-type transition-metal diborides," *Physical Review B,* **63**[4] 045115 (2001).

[80] I. R. Shein and A. L. Ivanovskii, "Band structure of ZrB_2, VB_2, NbB_2, and TaB_2 hexagonal diborides: Comparison with superconducting MgB_2," *Physics of the Solid State,* **44**[10] 1833-39 (2002).

[81] "Card number 01-075-1050, International Centre for Diffraction Data."

[82] X. Zhang, X. Luo, J. Han, J. Li, and W. Han, "Electronic structure, elasticity and hardness of diborides of zirconium and hafnium: First principles calculations," *Computational Materials Science,* **44**[2] 411-21 (2008).

[83]J. W. Lawson, C. W. Bauschlicher, and M. S. Daw, "Ab Initio Computations of Electronic, Mechanical, and Thermal Properties of ZrB_2 and HfB_2," *J. Am. Ceram. Soc.*, **94**[10] 3494-99 (2011).

[84]V. A. Gasparov, N. S. Sidorov, I. I. Zver'kova, and M. P. Kulakov, "Electron transport in diborides: Observation of superconductivity in ZrB_2," *Journal of Experimental and Theoretical Physics Letters,* **73**[10] 532-35 (2001).

[85]J. W. Zimmermann, G. E. Hilmas, W. G. Fahrenholtz, R. B. Dinwiddie, W. D. Porter, and H. Wang, "Thermophysical Properties of ZrB_2 and ZrB_2–SiC Ceramics," *J. Am. Ceram. Soc.,* **91**[5] 1405-11 (2008).

[86]A. S. M. International, "ASM Ready Reference: Electrical and Magnetic Properties of Metals." ASM International: Materials Park, OH, (2000).

[87]W. D. Kingery, "Factors Affecting Thermal Stress Resistance of Ceramic Materials," *J. Am. Ceram. Soc.,* **38**[1] 3-15 (1955).

[88]J. W. Zimmermann, G. E. Hilmas, and W. G. Fahrenholtz, "Thermal shock resistance of ZrB_2 and ZrB_2–30% SiC," *Mater. Chem. Phys.,* **112**[1] 140-45 (2008).

[89]W. H. Gu and K. T. Faber, "Tensile Behavior of Microcracking SiC-TiB_2 Composites," *J. Am. Ceram. Soc.,* **78**[6] 1507-12 (1995).

[90]W. H. Gu, K. T. Faber, and R. W. Steinbrech, "Microcracking and R-curve behavior in SiC-TiB_2 composites," *Acta Metall. Mater.,* **40**[11] 3121-28 (1992).

[91]D. J. Green, "Critical Microstructures for Microcracking in Al_2O_3-ZrO_2 Composites," *J. Am. Ceram. Soc.,* **65**[12] 610-14 (1982).

[92]D. J. Green, "Stress-Induced Microcracking at Second-Phase Inclusions," *J. Am. Ceram. Soc.,* **64**[3] 138-41 (1981).

[93]R. W. Steinbrech, "Toughening mechanisms for ceramic materials," *J. Eur. Ceram. Soc.,* **10**[3] 131-42 (1992).

[94]P. G. Karandikar, G. Evans, S. Wong, M. K. Aghajanian, and M. Sennett, "A Review of Ceramics for Armor Applications," pp. 163-75. in Advances in Ceramic Armor IV: Ceramic Engineering and Science Proceedings, Volume 29, Issue 6**.** John Wiley & Sons, Inc., 2009.

[95]M. Flinders, D. Ray, A. Anderson, and R. A. Cutler, "High-Toughness Silicon Carbide as Armor," *J. Am. Ceram. Soc.,* **88**[8] 2217-26 (2005).

[96]D. Ray, M. Flinders, A. Anderson, and R. A. Cutler, "Hardness/Toughness Relationship for SiC Armor," pp. 401-10. in 27th Annual Cocoa Beach Conference on Advanced Ceramics and Composites: A: Ceramic Engineering and Science Proceedings**.** John Wiley & Sons, Inc., 2008.

[97]D. S. King, W. G. Fahrenholtz, and G. E. Hilmas, "Silicon carbide-titanium diboride ceramic composites " *J. Eur. Ceram. Soc.*, **33**[15-16] 2943-51 (2013).

[98]G. E. Hilmas and T.-Y. Tien, "Effect of AlN and Al_2O_3 additions on the phase relationships and morphology of SiC Part I Compositions and properties," *J. Mater. Sci.*, **34**[22] 5605-12 (1999).

[99]J. B. Wachtman, W. R. Cannon, and M. J. Matthewson, "Mechanical Properties of Ceramics," 2nd ed. John Wiley & Sons, Inc.: Hoboken, NJ, (2009).

[100]T. L. Anderson, "Fracture Mechanics," 3rd ed. Taylor & Francis Group, LLC: Boca Raton, Fl, (2005).

[101]D. J. Green, "Microcracking Mechanisms in Ceramics," pp. 457-78. in Fracture Mechanics of Ceramics, **Vol. 5.** Edited by R. C. Bradt, A. G. Evans, D. P. H. Hasselman, and F. F. Lange, Plenum Press, 1983.

[102]M. K. Ferber, P. F. Becher, and C. B. Finch, "Effect of Microstructure on the Properties of TiB_2 Ceramics," *J. Am. Ceram. Soc.*, **66**[1] C-2-C-3 (1983).

[103]H. Cai, W. H. Gu, and K. T. Faber, "Microcrack Toughening in a SiC-TiB_2 Composite," in Proceedings of the American Society for Composites Fifth Technical Conference; composite materials in transition.

[104]E. W. Neuman, G. E. Hilmas, and W. G. Fahrenholtz, "Strength of Zirconium Diboride to 2300°C," *J. Am. Ceram. Soc.*, **96**[1] 47-50 (2013).

[105]E. W. Neuman, G. E. Hilmas, and W. G. Fahrenholtz, "Mechanical behavior of zirconium diboride–silicon carbide ceramics at elevated temperature in air," *J. Eur. Ceram. Soc.*, **33**[15–16] 2889-99 (2013).

[106]A. Bellosi and F. Monteverde, "Ultra-Refractory Ceramics: the Use of Sintering Aids to Obtain Microstructure Control nad Properties Improvement," *Key Eng. Mater.*, **264-268** 787-92 (2004).

[107]J. J. Meléndez-Martínez, A. Domínguez-Rodríguez, F. Monteverde, C. Melandri, and G. de Portu, "Characterisation and high temperature mechanical properties of zirconium boride-based materials," *J. Eur. Ceram. Soc.*, **22**[14–15] 2543-49 (2002).

[108]D. Sciti, S. Guicciardi, A. Bellosi, and G. Pezzotti, "Properties of a Pressureless-Sintered ZrB_2–$MoSi_2$ Ceramic Composite," *J. Am. Ceram. Soc.*, **89**[7] 2320-22 (2006).

[109]W. Li, X. Zhang, C. Hong, W. Han, and J. Han, "Microstructure and mechanical properties of zirconia-toughened ZrB_2–$MoSi_2$ composites prepared by hot-pressing," *Scr. Mater.*, **60**[2] 100-03 (2009).

[110]F. Monteverde, "Beneficial effects of an ultra-fine α-SiC incorporation on the sinterability and mechanical properties of ZrB_2," *Applied Physics A*, **82**[2] 329-37 (2006).

[111]A. Rezaie, W. G. Fahrenholtz, and G. E. Hilmas, "Effect of hot pressing time and temperature on the microstructure and mechanical properties of ZrB_2–SiC," *J. Mater. Sci.*, **42**[8] 2735-44 (2007).

[112]J. Watts, G. Hilmas, and W. G. Fahrenholtz, "Mechanical Characterization of ZrB_2–SiC Composites with Varying SiC Particle Sizes," *J. Am. Ceram. Soc.*, **94**[12] 4410-18 (2011).

[113]S.-Q. Guo, T. Nishimura, T. Mizuguchi, and Y. Kagawa, "Mechanical properties of hot-pressed ZrB_2–$MoSi_2$–SiC composites," *J. Eur. Ceram. Soc.*, **28**[9] 1891-98 (2008).

[114]W.-W. Wu, G.-J. Zhang, Y.-M. Kan, and P.-L. Wang, "Reactive Hot Pressing of ZrB_2–SiC–ZrC Composites at 1600°C," *J. Am. Ceram. Soc.*, **91**[8] 2501-08 (2008).

[115]F. Monteverde, A. Bellosi, and S. Guicciardi, "Processing and properties of zirconium diboride-based composites," *J. Eur. Ceram. Soc.*, **22**[3] 279-88 (2002).

[116]F. Monteverde and A. Bellosi, "Efficacy of HfN as sintering aid in the manufacture of ultrahigh-temperature metal diborides-matrix ceramics," *J. Mater. Res.*, **19**[12] 3576-85 (2004).

[117]M. Taya, S. Hayashi, A. S. Kobayashi, and H. S. Yoon, "Toughening of a Particulate-Reinforced Ceramic-Matrix Composite by Thermal Residual Stress," *J. Am. Ceram. Soc.*, **73**[5] 1382-91 (1990).

[118]A. H. Heuer and V. L. K. Lou, "Volatility Diagrams for Silica, Silicon Nitride, and Silicon Carbide and Their Application to High-Temperature Decomposition and Oxidation," *J. Am. Ceram. Soc.*, **73**[10] 2789-803 (1990).

[119]S. S. Ordan'yan, A. I. Dmitriev, and E. S. Moroshkina, *Inorg. Mater.*, **25**[10] 1487-89 (1989).

[120]E. Rudy, D. P. Harmon, and C. E. Brukl, "Part I. Related Binary Systems. Volume II. Ti-C and Zr-C System." in**.** Air Force Materials Labratory, AFML-TR-65-2, Wright Patterson Air Force Base, OH, 1965.

[121]C. C. Sorrell, V. S. Stubican, and R. C. Bradt, "Mechanical Properties of ZrC-ZrB_2 and ZrC-TiB_2 Directionally Solidified Eutectics," *J. Am. Ceram. Soc.*, **69**[4] 317-21 (1986).

[122]T. Tsuchida and S. Yamamoto, "Spark plasma sintering of ZrB_2–ZrC powder mixtures synthesized by MA-SHS in air," *J. Mater. Sci.*, **42**[3] 772-78 (2007).

[123] S. H. Shim, K. Niihara, K. H. Auh, and K. B. Shim, "Crystallographic orientation of ZrB_2-ZrC composites manufactured by the spark plasma sintering method," *Journal of Microscopy,* **205**[3] 238-44 (2002).

[124] C. C. Sorrell, H. R. Beratan, R. C. Bradt, and V. S. Stubican, "Directional Solidification of (Ti, Zr) Carbide-(Ti, Zr) Diboride Eutectics," *J. Am. Ceram. Soc.,* **67**[3] 190-94 (1984).

[125] R. Chang and L. J. Graham, "Low Temperature Elastic Properties of ZrC and TiC," *J. Appl. Phys.,* **37**[10] 3778-83 (1966).

VITA

Derek Scott King was born on May 5th, 1988 in Kansas City, MO. In August of 2006 Derek started his undergraduate degree as an aerospace engineer at the University of Missouri-Rolla (now Missouri University of Science and Technology), but later decided to join the Ceramic Engineering Department (a great decision). During his undergraduate career, Derek was a member of many of the student groups. Derek also took the opportunity to work as an REU student, co-op, and undergraduate research assistant. Knowing he wanted to continue research, Derek spent his last semester taking undergraduate and graduate courses at Missouri S&T. In December of 2010, Derek received his Bachelors of Science degree in Ceramic Engineering from Missouri S&T.

Derek began his graduate work in January of 2011 working on advanced ceramics for armor applications. During his first semester as a graduate student, Derek was awarded a Chancellors Fellowship from the recommendation of his advisors Bill Fahrenholtz and Greg Hilmas. Derek received his Masters of Science in Ceramic Engineering from Missouri S&T in December of 2012, during his time as a Masters student, he presented his work at two conferences and published two manuscripts.

Derek continued his graduate work at Missouri S&T when he was given the exciting opportunity to study the plasma arc welding of ceramics for his PhD. Derek has presented his PhD work at six conferences and demonstrated arc welding of ceramics, leaving many jaws agape. His work has led to the publication of two manuscripts, and two pending manuscripts. Derek received his PhD in Ceramic Engineering from Missouri S&T in May of 2015. After his many years in Rolla, MO, Derek looks forward to starting an exciting career at UES Inc. in Dayton, OH.